Observation of Turbulence Echo Characteristics and Humidity Profiles with the MU Radar–RASS

by

Jun-ichi Furumoto

Observation of Turbulence Echo Characteristics and Humidity Profiles with the MU Radar–RASS

by

Jun-ichi Furumoto

Acknowledgments

I would like to express my sincere gratitude to Professor Toshitaka Tsuda for his enlightening scientific guidance, careful reading of the manuscript, and constructive discussions concerning this research. A great debt of appreciation is owed to Professor Shoichiro Fukao for his kind guidance and hearty encouragement. Special thanks are also due to Professor Toru Sato for his helpful advice and invaluable scientific suggestions.

In addition, I am extremely grateful to Drs. Gregory Nastrom and Thomas VanZandt for their kind discussions concerning this work and cooperative study in developing the dual-beamwidth method for observing atmospheric turbulence intensity. Likewise, I am grateful to Dr. Gregory Nastrom for his kind support during my stay at St. Cloud State University, Minnesota.

Drs. Hiroaki Iwasaki and Takehiko Satomura also deserve thanks for the valuable scientific advice and helpful suggestions they gave me which greatly contributed to my understanding of meteorological phenomena. Drs. Denis Riggin, David Fritts, and David Low also provided guidance and comments that enabled me to perform this work. Others whom I thank include Drs. Takuji Nakamura and Takeshi Horinouchi for their valuable scientific suggestions and careful reading of the original manuscript, Drs. Tatsuhiro Adachi and Yoshihisa Masuda for their work in developing the MU radar–RASS system, Dr. Hiroyuki Hashiguchi for his suggestions and advice on radar techniques, Drs. Mamoru Yamamoto and Masatomo Fujuwara for their instructive suggestions, Kenji Kurimoto, Masaki Miyamoto and Yoshihito Arikawa for their valuable discussions and cooperation in performing this study, Drs. Takayuki Yoshihara and Yuichi Aoyama for providing the precipitable water vapour data obtained by GPS and their helpful advice concerning the analysis of this data, Dr. Atsushi Shimizu and Tri Wahyu Hadi for their valuable comments and technical support regarding the computer software.

I am also grateful to Professors Hiroshi Matsumoto, Kozo Hashimoto, Yoshiharu Omura and all other staff members of Kyoto University's Radio Science Center for Space and Atmosphere (RASC).

Mr. Yoshihiro Watanabe of the Japan Weather Association (JWA) provided radiosonde data during the MU radar experiment in July 1999. The meteorological radar located at Osaka is operated by Japan Meteorological Agency (JMA). The radiometer data from the July, 1999 campaign were obtained by using a Radiometrics WPR-1300 borrowed from Dr. Kazumasa Aonashi of the Meteorological Research Institute. The MU radar is operated by RASC, Kyoto University. The operators, from Mitsubishi Electric Corporation, deserve high praise for their unflagging efforts to maintain and operate the MU radar. My month-long visit to Dr. Nastrom in Minnesota was supported by a grant of the Kyoto University Foundation. Also, this work was supported by a grant of the Japan Society for the Promotion of Science (JSPS) under the Fellowships for Japanese Young Scientists.

Abstract

This thesis discusses the characteristics of atmospheric turbulence investigated with the MU (middle and upper atmosphere) radar, and describes a new radar technique for measuring successive humidity profiles using turbulence echoes. Meteorological disturbances are characterized by various parameters, such as wind velocity, temperature, and humidity which contribute, respectively, to kinetic energy, sensible heat, and latent heat. Three-dimensional wind velocity can be observed by the wind profiler radar, while RASS (radio acoustic sounding system) can provide virtual temperature (T_v) profiles based on the relationship between T_v and acoustic speed. RASS is a remote-sensing technique that uses clear air Doppler radar and high-power acoustic transmitters. The former detects the Doppler shift of the radar echo scattered by refractive index fluctuations generated by the propagating acoustic wave. Combining RASS with the MU radar (MU radar–RASS) allows continuous monitoring of temperature and three-dimensional wind velocity profiles with time and height resolution of, respectively, a few minutes and a few hundred meters. In this thesis, we discuss the characteristics of the atmospheric turbulence echo revealed through high-resolution temperature profiles obtained by MU radar–RASS measurement and explain a new radar technique for measuring water-vapor profiles.

First, the estimation of the turbulence energy dissipation rate (ε) is considered. Two methods can be applied to estimate ε: use of the Doppler spectrum width and the echo power method. The spectral width method requires fewer assumptions than the echo power method. However, the spectral width is affected by other factors that cause additional broadening of the spectrum. The correction of these artificial broadening effects may be comparable in magnitude to the observed width, especially under strong wind conditions, so a small error in the correction may lead to a large error in ε.

To reduce the error, we developed a method to remove broadening effects by using multiple radar observation with different radar beam widths. This method was evaluated with the MU radar under various background wind conditions and was found to be an effective means of accurately estimating ε. Moreover, ε derived by the conventional method after removing the broadening effects from the wind velocity observation was sufficiently accurate under weak wind conditions.

Next, we made a detailed comparison of the ε obtained using the echo power and spectral width methods. The two methods have not previously been compared because such a comparison requires simultaneous temperature observations with a high time resolution that have not been available. High-resolution temperature profiles obtained with the MU radar–RASS was used to estimate ε in both methods. We found that the variation of the turbulent echo power is mainly

determined by variation in the vertical gradient of the water-vapor mixing ratio.

This strong dependence of the echo power on the vertical gradient of humidity was used to develop a radar remote-sensing technique that can be applied to measure humidity profiles. The differential equation relating humidity, echo-power intensity, and temperature was deduced. The estimation procedure using the high-resolution temperature profile obtained with the MU radar–RASS was then developed. Humidity profiles derived from the MU radar–RASS agreed with simultaneous radiosonde results at altitudes from 1.5 to 7.0 km.

The remote-sensing technique was then improved to enable continuous monitoring of humidity profiles. This improved method refers to complementary measurements such as precipitable water vapor obtained through simultaneous GPS-based measurement. Applying the method, we achieved the estimation of the continuous time-height distribution of humidity. The MU radar–RASS observation campaign was carried out for 7 days in July, 1999, and humidity profiles were estimated using the method. The time-height structure of radar-derived humidity agreed well with simultaneous radiosonde results taken every three hours. The radar-derived humidity profiles also revealed short-term fluctuations of 1-1.5 hours which cannot be monitored through radiosonde measurements. The radar-derived humidity correlated well with the cloud-top height observed by meteorological satellite. Moreover, the time evolution of the radar-derived humidity was consistent with the movement and the developing/decaying process of rain clouds monitored with meteorological radar.

We hope that the findings of this study will help to clarify the thermodynamics of mesoscale atmospheric phenomena.

Contents

List of Figures

List of Tables

Chapter 1

General Introduction

1.1 Tropospheric Atmospheric Phenomena

A major part of the solar radiation reaches the Earth's surface without absorption by the atmosphere. The tropospheric atmosphere is heated by infrared radiation from the Earth's surface, and convection transfers thermal and kinetic energy upward. Especially in the atmospheric boundary layer where the atmosphere undergoes direct infrared heating, active convections often appear and sometimes reach up to the tropopause under low-stability conditions. These deep convections are thought to transport minor constituents such as carbon dioxide between the troposphere and the stratosphere.

The troposphere is home to most of the meteorological phenomena, such as fronts and storms, that greatly affect human activities. Tropospheric meteorological phenomena can be categorized according to their time and spatial scales. Synoptic phenomena with a horizontal scale ranging from several hundred to thousands of kilometers play an important role in mid-latitude weather systems. These phenomena often involve smaller-scale phenomena. Meso-scale phenomena with a horizontal scale ranging from several tens to several hundred kilometers are especially important because they can bring about severe disasters.

The behavior of meteorological disturbances is characterized by various parameters, such as wind velocity, temperature, and humidity, which contribute to, respectively, kinetic energy, sensible heat, and latent heat. Therefore, precise measurements of these parameters with good time and height resolutions are important for studies of meso-scale meteorological phenomena. For example, upward fluxes of momentum, sensible heat, and latent heat are important for the study of vertical energy transport, which is closely related with the evolution process of a cloud system. However, the detailed structure of meso-scale phenomena

has not been fully analyzed because of a lack of high-resolution observations.

Wind profiler radars can be used to observe a three-dimensional wind field, while RASS (radio acoustic sounding system) can provide virtual temperature profiles with time and height resolutions of several minutes and a few hundred meters, respectively. Yet, a remote-sensing technique that allows us to observe humidity profiles with good time and height resolution under any meteorological conditions has not been developed. One purpose of this study has been to develop a radar remote-sensing technique to estimate humidity profiles with a good time and height resolutions.

In addition, turbulence is an important aspect of atmospheric motion. The process of vertical diffusion caused by atmospheric turbulence is especially important to the stratosphere-troposphere exchange. Turbulence is generated by Kelvin-Helmholtz instability which is caused by various atmospheric phenomena such as atmospheric gravity waves and wind shear.

The turbulence energy dissipation rate (ε) is a fundamental atmospheric parameter that describes turbulence characteristics. ε represents the rate of energy cascading into smaller eddies until the energy is transformed to heat without any input or output of kinetic energy. This study is also concerned with the development of ground-base radar remote-sensing techniques to measure ε.

Wind profiler radars have been used to estimate ε in past studies, but it is still difficult to obtain a precise estimate of ε, especially under strong wind or shear conditions. Thus, a goal of my research group has been to develop a method to precisely measure ε under any meteorological conditions. In the following section, the current status of ε and humidity measurement techniques is described.

1.2 Current Status of Turbulence Energy Dissipation Rate Measurements

There are several methods which can be used to estimate the intensity of ε. One technique used to measure ε employs the analysis of a power spectrum of velocity fluctuation which theoretically satisfies the -5/3 power law for the spectra [e.g., *Crooks et al.*, 1967]. Since this technique requires very good time and spatial resolution, it is applied with *in-situ* wind-velocity measurements made with high-resolution instruments such as anemometers aboard balloons and aircraft [*Chen*, 1974; *Gage et al.*, 1980]. Typical values of ε obtained through *in-situ* measurements in the troposphere are summarized in Fig. 1 of *Hocking and Mu* [1997]. They reported the value of ε under various meteorological conditions, and these values are shown here in Figure 1.1. In the earlier studies, *Kung* [1966] obtained

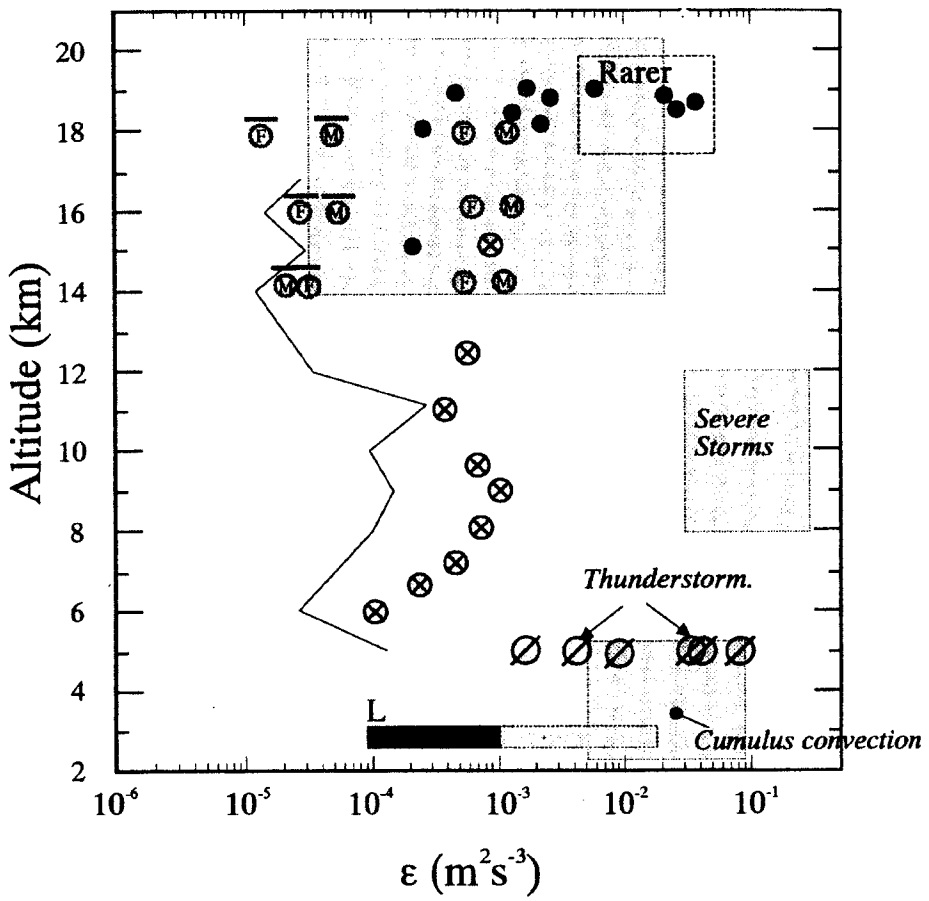

Figure 1.1: Various *in-situ* measurements of kinetic energy dissipation rates in the troposphere [*Hocking and Mu*, 1997]. ⊗, •, and ⊘ show the results of *Kung* [1966], *Vinnichienko and Dutton* [1969] and *Bohne* [1981], respectively. The line shows the results of *Crane* [1980]. The shaded areas represent the results of *Chen* [1974]. Ⓕ and Ⓜ are the values of ε reported by *Lilly et al.* [1974] over flatland/water and mountainous areas, respectively. The data of *Lilly et al.* [1974] with and without the overline indicate, respectively, the average over the whole atmosphere and in only the turbulent layer. The rectangle indicated by 'L' shows the results of *Lee et al.* [1988]. About 90% of their data lay in the black rectangular region.

ε between 6–15 km, and *Vinnichenko and Dutton* [1969] also reported the results of their HICAT campaign. *Lilly et al.* [1974] showed the values of ε between the height of 14–18 km, and *Chen* [1974] reported the value of ε in the three height ranges. Recent studies have also been performed such as *Crane* [1980] and *Lee et al.* [1988]. *Hocking and Mu* [1997] also reviewed the severity of ε as classified by *Vinnichenko and Dutton* [1969]. Through their analysis of many turbulence reports from aircraft, they classified the severity into four categories: 'no turbulence', 'light turbulence', 'moderate turbulence', and 'severe turbulence' with respective ε values of $< 3.0 \times 10^{-3}$, $\geq 3.0 \times 10^{-3}$ and $< 1.2 \times 10^{-2}$, $\geq 1.2 \times 10^{-2}$ and $< 1.0 \times 10^{-1}$ and $\geq 1.0 \times 10^{-1}$ $\mathrm{m^2 s^{-3}}$.

It has been realized for decades that ε can be measured by atmospheric radar, which provides the advantage of allowing us to measure turbulence continuously in space and time without perturbing the medium [e.g., *Atlas*, 1964]. The wind profiler radar has often been used to estimate ε from the Doppler spectra of turbulence echoes [e.g., *Gage and Green*, 1980; *Gossard*, 1990; *Hocking*, 1983, 1985, 1996]. Two types of method are generally used to estimate ε: one based on the echo ower and one base on the Doppler spectral width. In the returned-power method the radar data are analyzed by means of a theory that involves several more-or-less uncertain assumptions and parameters such as the the radar system parameters and the volume filling factor of the turbulence [*VanZandt et al.*, 1978; *Hocking and Mu*, 1997].

Spectral width methods take advantage of the fact that small air parcels within a radar range volume show random motion due to turbulence. Therefore, the Doppler spectrum is broadened around the mean wind velocity, and the Doppler spectral width can be related to the structure constant of the turbulence velocity. However, the spectral width is affected by other factors that cause additional broadening of the spectrum. Since the correction of these broadening effects may be comparable to the spectral width caused by turbulence, these effects must be carefully removed from the observed spectral width.

The values of ε obtained by *in-situ* and the radar methods were compared by several studies [e.g., *Hocking and Mu*, 1997; *Bertin et al.*, 1997]. *Hocking and Mu* [1997] derived ε from *in-situ* and turbulence echo power, and reported broad agreement in terms of the magnitude and shape between the two sets of ε values.

1.3 Current Status of Humidity Measurements

Water vapor, mostly in the troposphere, plays an important role in the atmospheric thermodynamics that transport latent heat through evaporation and condensation. Although the weight of atmospheric humidity is as small as 0.1–

1% of the total atmospheric weight, the humidity fluctuates considerably and this fluctuation is an important driving source of the meso-scale meteorological phenomena.

The most common technique for measuring a humidity profile is with a balloon-borne radiosonde, as is routinely done at meteorological stations around the world. A radiosonde system consists of a balloon, electronic sensors, and a radio transmitter. The radiosonde ascends at a speed of about 5 ms^{-1}, measures pressure, temperature, and humidity, then sends the data to a radio-receiver on the ground. Note that the radiosonde height is determined by integrating the measured pressure and assuming hydrostatic equilibrium. The radiosonde's time resolution is at most a few hours, though it can measure pressure, temperature, and relative humidity with a height resolution of 30 m with an accuracy of 0.5 hPa, 0.2°C, and 3%, respectively [e.g., *Miloshevich et al.*, 2001].

Several remote-sensing techniques for observing the humidity profile have been developed. A multi-frequency microwave radiometer can observe the height distribution of water vapor and liquid water every 1 minute, although the height resolution is at most a few km [e.g., *Ware et al.*, 2001]. Although the radiometer has excellent time resolution, it is not suitable for the study of severe meteorological phenomena because the radiometer data may become inaccurate under rainy conditions. In addition, calibration using simultaneous radiosondes is necessary to obtain accurate estimates. Humidity profiles can be also retrieved from radiometer data combined with K_a-band Doppler radar measurements of the cloud-layer height [*Stankov et al.*, 1995] and 449-MHz wind profiler measurements of significant moisture gradients [*Stankov et al.*, 1996].

Differential absorption lidar (DIAL) and Raman lidar can also be used to observe a humidity profile, although the observation is restricted to the night-time and under a clear sky, or at least a sky without thick clouds. [e.g., *Goldsmith et al.*, 1994; *Wulfmeyer et al.*, 1998]. Lidar observation has better time resolution and wider height coverage than a radiosonde.

Global Positioning System (GPS) receivers can be used to observe the precipitable water vapor (PWV) with time resolution of a few minutes under any meteorological conditions. The GPS provides a compact and calibration-free system, and about a thousand GPS receivers have been installed throughout Japan and are routinely operated by Geographical Survey Institute (GSI) [*Miyazaki and Hatanaka*, 1998]. In addition, a method of three-dimensional humidity estimation using a number of GPS receivers combined with the tomography technique has recently been developed [*Hirahara*, 2000; *Seko et al.*, 2000; *Yoshihara et al.*, 2001].

For monitoring a humidity profile with good time and height resolution under

any meteorological conditions, a new radar remote-sensing technique has been developed that uses the characteristics of clear air echoes. The volume reflectivity of turbulence echoes (η_{turb}) detected with a wind profiler radar is closely related to the refractive index gradient (M). Moreover, M in the lower atmosphere largely depends on the height gradient of specific humidity ($\mathrm{d}q/\mathrm{d}z$). Then, η_{turb} can be related to $\mathrm{d}q/\mathrm{d}z$ [*Hocking and Mu*, 1997; *Tsuda et al.*, 2001]. Using this correlation, *Gossard et al.* [1998] estimated a height structure of $\mathrm{d}q/\mathrm{d}z$ from radar echoes combined with wind profiler observations. Moreover, *Gossard et al.* [1999] retrieved a q profile at altitudes of 0.5–2.0 km by incorporating information on PWV with GPS measurements.

The q profile at 1.5–10 km was also estimated from MU radar–RASS observation using the correlation between M and the Brunt Väisälä frequency squared (N^2) [*Tsuda et al.*, 2001]. Moreover, *Furumoto et al.* [2002] improved the estimation of q by MU radar–RASS by using simultaneous GPS measurements of PWV to achieve the more robust estimation under various meteorological conditions. The detailed description of the estimation with the MU radar will be presented in Chapter 5 and 6.

1.4 Scope of This Thesis

This thesis is concerned with the development of a method to estimate turbulence characteristics and humidity profiles using the MU radar–RASS with the goal of being able to continuously and simultaneously monitor the wind velocity, temperature, humidity, and turbulence intensity.

The structure of this thesis is as follows. In Chapter 2, we describe the basic technology of atmospheric radar – which is the basis of this research – and the basic principle underlying the turbulence scattering echo. The principle of the RASS is explained and an outline of the MU radar–RASS system is given. Typical observation results from the MU radar–RASS are also described.

Chapter 3 is concerned with a new dual-beamwidth radar method for inferring the velocity variance due to the turbulence kinetic energy density. As explained above, the spectral width method for estimating ε may contain large errors under strong wind or shear conditions. To obviate these difficulties, our group has developed a dual-beamwidth method which is less affected than the conventional single-beamwidth method by the error of the wind-velocity estimation. We have tested and compared the dual- and single-beamwidth methods using the MU radar. Consequently, we found that ε can be precisely estimated by using our method. We also show that the ε derived through the conventional observation method under light wind conditions is sufficiently reliable.

In Chapter 4, we compare ε obtained by the spectral width and echo power methods. In both methods, N^2 must be measured to estimate ε. We have estimated and compared ε as determined by the two methods using N^2 derived from a temperature profile with high time and height resolution. We found the variation of turbulence echo power is strongly dependent on that of the vertical humidity gradient. In Chapter 5, we describe the development of a radar technique for determining the height profile of humidity by using the dependence of the clear air echo power on the humidity gradient in the troposphere. We evaluated the accuracy of the estimated humidity by comparing it to simultaneous radiosonde results.

In Chapter 6, we explain how the radar remote-sensing technique can be improved to enable continuous monitoring of humidity profiles. To achieve continuous estimation, even under disturbed meteorological conditions, our improved method refers to complementary measurements, such as the PWV obtained from the propagation delay of GPS radio signals. We also investigated the correlation between the radar-derived humidity and the cloud-top height estimated from irradiance measurement by satellite. We also discuss a detailed time-height structure of the retrieved humidity, referring to the horizontal distribution of the rain echo obtained from a nearby meteorological radar, and focusing on the correspondence to the passage of rain clouds over the MU radar.

In Chapter 7, we summarize this work and present conclusions.

Chapter 2

MU Radar–RASS Observation

In this chapter, the basic principle underlying turbulence echo and temperature observations with the MU radar–RASS is explained. First, the radar equation of the turbulence echo and basic characteristics of the turbulence echo are described. The radar methods used to estimate ε are then explained, and the basic principle of the RASS technique, especially the radar equation of the RASS echo and the ray-tracing of acoustic wavefronts, are described. The RASS developed for use with the MU radar is described, and examples of the temperature observation results obtained by the MU radar–RASS are shown.

2.1 Fundamental Characteristics of Turbulence Echoes

2.1.1 Radar Equation for Turbulence Echoes

In this section, we review the radar equation for clear air echoes under the assumption that a radiowave whose power is P_t is radiated in all directions with a uniform strength. The power density (P_i) per unit area perpendicular to the direction of propagation at a sufficiently distant point from the radar antenna is

$$P_\mathrm{i} = G_t \frac{P_\mathrm{t}}{4\pi r^2}, \tag{2.1}$$

where r is the distance between the point and the transmitting antenna and G_t is the gain of the transmitting antenna. If we consider a target that scatters the radiowaves in all directions, the density of scattered power (P_s) at a distance of r' is

$$P_\mathrm{s} = \frac{P_\mathrm{i}}{4\pi r'^2}\sigma. \tag{2.2}$$

We can consider the scattered echo to be received by an antenna whose effective area and loss factor is, respectively, A_e and L. The received echo power (P_r) is then shown as

$$P_r = P_s A_e L = \frac{P_t G_t A_e L}{16\pi^2 r^2 r'^2}. \tag{2.3}$$

In the case of mono-static radars r is equal to r'. The universal relationship between G_t and A_e is [*Silver*, 1951]

$$G_t = \frac{4\pi A_e}{\lambda^2}, \tag{2.4}$$

where λ is the radar wavelength. Then, the received echo power (P_r) can be rewritten as

$$P_r = \frac{P_t A_e^2 L}{4\pi\lambda^2 r^4}\sigma. \tag{2.5}$$

Now, consider the scattering due to small fluctuations in the refractive index (n), which is continuous in space. Assuming that the scattering is due to uniformly distributed targets in the radar range volume (V), the volume refractivity ($\overline{\eta}$), which is the scattering cross-section per unit volume, is defined as

$$\overline{\eta} = \frac{\mathrm{d}\sigma}{\mathrm{d}V}. \tag{2.6}$$

For a radar with a circular antenna, V is represented as

$$V = \pi(r\theta_r)^2 \Delta r, \tag{2.7}$$

where θ_r is the one-way half-power half-width of a radar antenna beam and Δr is the range resolution. Moreover, *Probert-Jones* [1962] showed that the relationship between θ_r and G_t is

$$G_t = (\frac{\pi a}{2\theta_r})^2, \tag{2.8}$$

where a is a factor representing the antenna's non-uniformity of illumination. The radar equation for a uniformly distributed target is then rewritten as

$$P_r = \frac{P_t A_e^2 L}{4\pi\lambda^2 r^4}\int \overline{\eta}\mathrm{d}V = \frac{P_t A_e^2 L}{4\pi\lambda^2 r^4} V\overline{\eta} = P_t \frac{\pi a^2 A_e \Delta r}{64 r^2}\overline{\eta}. \tag{2.9}$$

For turbulence echo observation, the volume refractivity by turbulence ($\overline{\eta_{turb}}$) can be derived from P_r.

However, this discussion is based on the idealized condition that the radar range volume is fully filled with turbulence. Rather than being continuously distributed, true atmospheric turbulence is isolated in thin layers that are 10 to

30 m thick with a vertical spacing of a few ten to a few hundred meters [*VanZandt and Vincent*, 1983; *Hocking et al.*, 1991; *Woodman and Chu*, 1989]. Thus, we need to introduce the volume filling factor (F) of turbulence layers within a radar range volume.

$$\overline{\eta_{turb}} = F\eta_{turb}, \tag{2.10}$$

where η_{turb} is the actual volume refractivity caused by turbulence. The exact value of F is difficult to determine from observations. However, in several studies, F has been estimated using numerical models. *Gage et al.* [1980] calculated F considering the relationship between wind shear and F under a dry atmosphere condition. *Cohn* [1995] estimated F using the NOAA Aeronomy Laboratory C_n^2 model developed by *Warnock and VanZandt* [1985] using wind and temperature profiles from simultaneous *in-situ* measurements.

$\overline{\eta_{turb}}$ is related to both a three-dimensional spectrum of the refractive index fluctuation caused by turbulence ($\Phi_n(\vec{\kappa})$) and the wavenumber of turbulence ($\vec{\kappa}$) that satisfy the Bragg scattering

$$\overline{\eta_{turb}} = \frac{\pi}{8}\kappa^2\Phi_n(\vec{\kappa}), \tag{2.11}$$

where $\kappa = |\vec{\kappa}|$. $\Phi_n(\vec{\kappa})$ attributable to isotropic turbulence can be related to a one-dimensional spectrum ($S(\kappa)$) of refractive index fluctuation as follows:

$$\Phi_n(\vec{\kappa}) = -\kappa\frac{\partial S}{\partial \kappa}. \tag{2.12}$$

Assuming that the energy from the large-scale source cascades to smaller eddies until the energy is transformed to heat without any energy input or output, *Kolmogorov* [1941] and *Heisenberg* [1948] described S as

$$S(\kappa) \propto \kappa^{-5/3}. \tag{2.13}$$

Then, using Equations (2.11), (2.12), and (2.13), $\overline{\eta_{turb}}$ is written as

$$\overline{\eta_{turb}} = -\frac{\pi}{8}\kappa^3\frac{\partial S}{\partial \kappa} = \frac{5}{3}\frac{\pi}{8}\kappa^2 S(\kappa). \tag{2.14}$$

While $S(\kappa)$ is described by a structure constant for the refractive index ($\overline{C_n^2}$) as follows:

$$S(\kappa) \sim \frac{1}{4}\overline{C_n^2}\kappa^{-5/3}. \tag{2.15}$$

Combining Equation (2.15) with Equation (2.14), we obtain

$$\overline{\eta_{turb}} = 0.38\overline{C_n^2}\lambda^{-\frac{1}{3}}, \tag{2.16}$$

where $\lambda = 4\pi/\kappa$.

Note that an anisotropic specular reflection can also be detected in addition to the isotropic turbulence scattering by a VHF radar [*Tsuda et al.*, 1986, 1997]. Thus, the MU radar observes both isotropic turbulence scattering and specular reflection. From their investigation of the aspect sensitivity of the echo power, *Tsuda et al.* [1986] showed that the echo power rapidly decreases between a zenith angle of 0° and 10°. At a zenith angle larger than about 10°, the echo power reaches a constant value, which seems to correspond to the level of the isotropic turbulence echo. In this study, we used the clear air echoes at a zenith angle of more than 10° to remove the influence of the specular reflection.

2.1.2 Turbulence Echo Intensity

The refractive index (n) in the neutral atmosphere is described as follows [*Balsley and Gage*, 1980]:

$$n - 1 = 77.6 \times 10^6 \left(\frac{p}{T} + 4810\frac{e}{T^2}\right), \tag{2.17}$$

where p (hPa) is the atmospheric pressure, e (hPa) is the partial pressure of water vapor, and T (K) is the atmospheric absolute temperature. The first and second terms of Equation (2.17) are called the dry and wet terms, respectively. The potential temperature (θ) can be defined from temperature and pressure. θ corresponds to the temperature at which an air parcel at p is compressed or expanded adiabatically to a standard pressure ($p_0 = 1000$ hPa).

$$\theta = T\left(\frac{p_0}{p}\right)^{\frac{R}{C_p}}, \tag{2.18}$$

where R is the gas constant and C_p is the specific heat at a constant pressure, and $R/C_p = 0.286$ in the lower atmosphere. Note that θ is a Lagrangian conserved quantity under adiabatic conditions.

Brunt Väisälä frequency squared (N^2) is defined as:

$$\frac{N^2}{g} = \frac{\mathrm{d}\ln\theta}{\mathrm{d}z} = \frac{1}{T}\left(\frac{\mathrm{d}T}{\mathrm{d}z} + \Gamma\right), \tag{2.19}$$

where z is the height, g is the gravitational acceleration, and $\Gamma = g/C_p = 9.80$ (K/km) is the dry adiabatic lapse rate. N^2 is an index for the vertical stability of the atmosphere. The atmosphere is statically stable when $N^2 > 0$ and unstable when $N^2 < 0$.

The ratio of the water vapor density to the atmospheric density in a moist atmosphere is defined as a mixing ratio (q), which is also a Lagrangian conserved quantity. q is described as

$$q = 0.622 \frac{e}{p}. \tag{2.20}$$

From Equations (2.18), (2.19), and (2.20), Equation (2.17) is rewritten as

$$n - 1 = -77.6 \times 10^{-6} \frac{p}{\theta} (\frac{p_0}{p})^{\frac{R}{C_p}} \{1 + 7800 \frac{q}{\theta} (\frac{p_0}{p})^{\frac{R}{C_p}}\}. \tag{2.21}$$

Then, if we ignore the vertical gradient of p, the vertical gradient of the refractive index (M) becomes [*Ottersten*, 1969]

$$M = -77.6 \times 10^{-6} \frac{p}{T} (\frac{N^2}{g} + 15600 \frac{q}{T} \frac{N^2}{g} - \frac{7800}{T} \frac{\mathrm{d}q}{\mathrm{d}z}). \tag{2.22}$$

The fluctuation of refractivity due to turbulence depends on M as well as the echo power intensity. The variance of n ($\overline{(\delta n)^2}$) due to turbulence satisfies the following equation:

$$\overline{(\delta n)^2} = \frac{5}{12} C_n^2 \int_0^{L_0} \kappa^{-5/3} d\kappa, \tag{2.23}$$

where L_0 is the outer scale of the inertial sub-range. Then, $\overline{C_n^2}$ becomes as follows

$$\overline{C_n^2} = 5.45 L_0^{-2/3} \overline{(\delta n)^2}. \tag{2.24}$$

Tatarski [1961] investigated the relationship between L_0 and $\overline{(\delta_n)^2}$ to estimate $\overline{\eta_{turb}}$ quantitatively, and derived $\overline{C_n^2}$ as follows:

$$\overline{C_n^2} = \zeta^2 \xi L_0^{4/3} M^2 F, \tag{2.25}$$

where ζ^2 is a constant and ξ depends on the turbulence diffusion coefficient ($\simeq$1.0). Many studies have estimated the energy dissipation rate (ε) and found the following relationship between L_0, ε, and N:

$$L_0 \propto \varepsilon^{1/2} N^{-3/2}. \tag{2.26}$$

Combining Equations (2.16), (2.25), and (2.26), a general expression relating the volume reflectivity for turbulence scattering to the turbulence parameter is given as

$$\overline{\eta_{turb}} = C F \varepsilon^{2/3} M^2 N^{-2}, \tag{2.27}$$

where C is a constant determined by the radar system parameters.

2.1.3 Estimation of ε from the Turbulence Echo

The most commonly used radar methods to estimate ε from the turbulence echo are the returned power and the spectral width methods (both are reviewed well by *Gage and Green* [1978] and *Hocking* [1983, 1985, 1999]). We will explain the theoretical background of both methods.

First, we will briefly describe the former, which is also called the echo power method. As shown in Equation (2.27) ε is related to $\overline{\eta_{turb}}$ as follows:

$$\varepsilon = DN^3M^{-3}\overline{\eta_{turb}}^{3/2}, \tag{2.28}$$

where $D = C^{-3/2}F^{-3/2}$. In this method, an additional instrument must be used to accurately determine the detailed time-height variations of N and M. *Hocking and Mu* [1997] derived ε using this method by measuring the turbulence echo power and using radiosondes, then compared the ε obtained from the turbulence echo power with those that have been determined in recent years by other techniques. However, as described above, an accurate measure of F is difficult to obtain and this value directly affects the echo power intensity. With this method, the ambiguity concerning the variation of F may thus cause a substantial error in the estimated ε.

The other method for estimating ε, the spectral width method, is as follows. Small air parcels within a radar sampling volume show random motion due to turbulence. Therefore, the radial velocity is the sum of the background wind velocity at which the turbulence is advecting as a whole and the relative velocity of the individual parcels. As a result, the Doppler spectrum is broadened around the mean wind velocity. Therefore, the Doppler spectral width can be related to ε as follows:

$$\varepsilon = 0.5N\sigma_{turb}^2, \tag{2.29}$$

where σ_{turb} is the spectral width caused by the turbulence. However, other factors cause additional broadening of the observed spectral width. Three important types of spectral broadening not due to turbulence have been identified: beam broadening, shear broadening, and broadening caused by changes in wind velocity [*Hocking*, 1983, 1985]. The impact of these types of broadening must be removed from the observed spectral width (σ_{obs}) as follows:

$$\begin{aligned} \sigma_{turb}^2 &= \sigma_{obs}^2 - \sigma_{corr}^2 \\ &= \sigma_{obs}^2 - \sigma_{beam}^2 - \sigma_{shear}^2 - \sigma_{wave}^2, \end{aligned} \tag{2.30}$$

where σ_{corr} is the total broadening and σ_{beam}, σ_{shear}, and σ_{wave} represent the deviation of wind velocities due to beam broadening, shear broadening, and broadening caused by changes in wind velocity, respectively.

Two methods for removing broadening effects have been proposed: one is the conventional method studied by *Hocking* [1985] and the other is a more recent method developed by *Nastrom* [1997]. In the conventional method, each broadening effect is independently estimated and removed from the observed spectral width. The detailed expression of each broadening effect is as follows. The beam broadening can be estimated from the antenna beam pattern and background wind velocity. *Hocking* [1985] proposed an approximate equation as follows:

$$\sigma_{beam} = \frac{1}{\sqrt{2}}\theta_r V_h, \tag{2.31}$$

where V_h is the horizontal wind velocity. When wind shear is present the wind velocity changes with height within a radar sample volume. Assuming a constant wind shear, σ_{shear} can be described as

$$\sigma_{shear} = \frac{1}{2}\left(\left|\frac{\partial u}{\partial z}\right| \sin\alpha\Delta r\right), \tag{2.32}$$

where $\dfrac{\partial u}{\partial z}$ is the wind shear, α is the zenith angle of the radar beam, and Δr is the range resolution. We can then estimate the broadening effect due to the transience of the wind velocity field. The resultant spectral width could spread due to temporal fluctuations of the wind velocity during the observation. The transience effects can be written as

$$\sigma_{wave} = \sqrt{\frac{2\ln 2}{3}}\frac{dv_{beam}}{dt}\tau, \tag{2.33}$$

where dv_{beam}/dt is the derivative of the line-of-sight wind velocity and τ is an incoherent integration time. The magnitude of σ_{wave} is generally smaller than that of the other two effects and is negligible in the troposphere and lower stratosphere [*Nastrom and Eaton*, 1997]. In the conventional method, the beam and shear broadening effects are independently estimated. However, there is another source of broadening which depends on both wind spread and wind shear, and these effects may become powerful under strong wind or shear conditions. *Nastrom* [1997] proposed a method to estimate beam and shear broadening that takes these effects into account by using a two-dimensional fan beam model with an observation region defined by two radii separated by $2\theta_r$. The broadening ($\sigma_{beam+shear}$) becomes

$$\sigma^2_{beam+shear} = \frac{\theta_r^2}{3}\left[\left(\cos^2\alpha U^2 + V^2\right) - 2\cos\alpha\sin^2\alpha U\left(\frac{\mathrm{d}U}{\mathrm{d}z}R\right) + \sin 4\alpha\left(\frac{\mathrm{d}U}{\mathrm{d}z}R\right)^2\right], \tag{2.34}$$

where U and V are the horizontal wind components parallel and perpendicular to the vertical plane of the beam, R is the radar sampling range, and α is the zenith angle of the radar beam. Equation (2.34) is an expansion of the exact expression for a fan beam [*Nastrom*, 1997, Equation (15)] in a power series of θ_r^2, ignoring the terms of order θ_r^4 and $(\Delta R/R)^2$, where ΔR is the range gate width. All of the quantities on the right side of the equation are known: α and R are the zenith angle and range, and the radar will measure U, V, and $\mathrm{d}U/\mathrm{d}z$. Note that since α is generally as small as 10°, $(U^2\cos^2\alpha + V^2) \sim (U^2 + V^2)$.

The same expression holds for a three-dimensional, circular, conical beam, but with a coefficient of 1/4 instead of 1/3. This suggests that the functional form of Equation (2.34) is rather general, although the coefficients depend on the shape of the observation volume.

Despite recent progress made using the spectral width method [*Cohn*, 1995; *Bertin et al.*, 1997; *Delage et al.*, 1997; *Narayana Rao et al.*, 1997; *Gossard et al.*, 1998], there are still difficulties. That is, the broadening effects may be comparable to σ_{turb}, especially under strong wind or shear conditions such as within the jet-stream, and the broadening effects may also be comparable to σ_{obs}^2, so that the small errors in broadening cause a large error in σ_{turb}^2 as discussed by *Fukao et al.* [1994]. Indeed, *Kurosaki et al.* [1996] and *Nastrom and Eaton* [1997] found a significant fraction of the σ_{turb}^2 values to be negative and so clearly in error. Similar errors are surely present in positive values of σ_{turb}^2, but have gone undetected. In Chapter 3, we describe a new broadening estimation method which is independent of the approximations in the model and the error of the observed wind velocity.

2.2 Temperature Observation with RASS

With normal wind profiler radar, we can observe successive profiles of three components of the wind velocity, the echo power, and the spectral width with a high time and height resolution. In addition, by applying RASS, we can simultaneously monitor temperature profiles [e.g, *May et al.*, 1989; *Tsuda et al.*, 1989]. In this section, we describe the basic principle and the observational procedure of RASS.

2.2.1 Fundamental Principle of RASS

Figure 2.1 shows the basic configuration of RASS observation. Transmitted acoustic pulses from the ground produce refraction-index fluctuations. We can detect the Doppler shift between the transmitted signal and received echoes

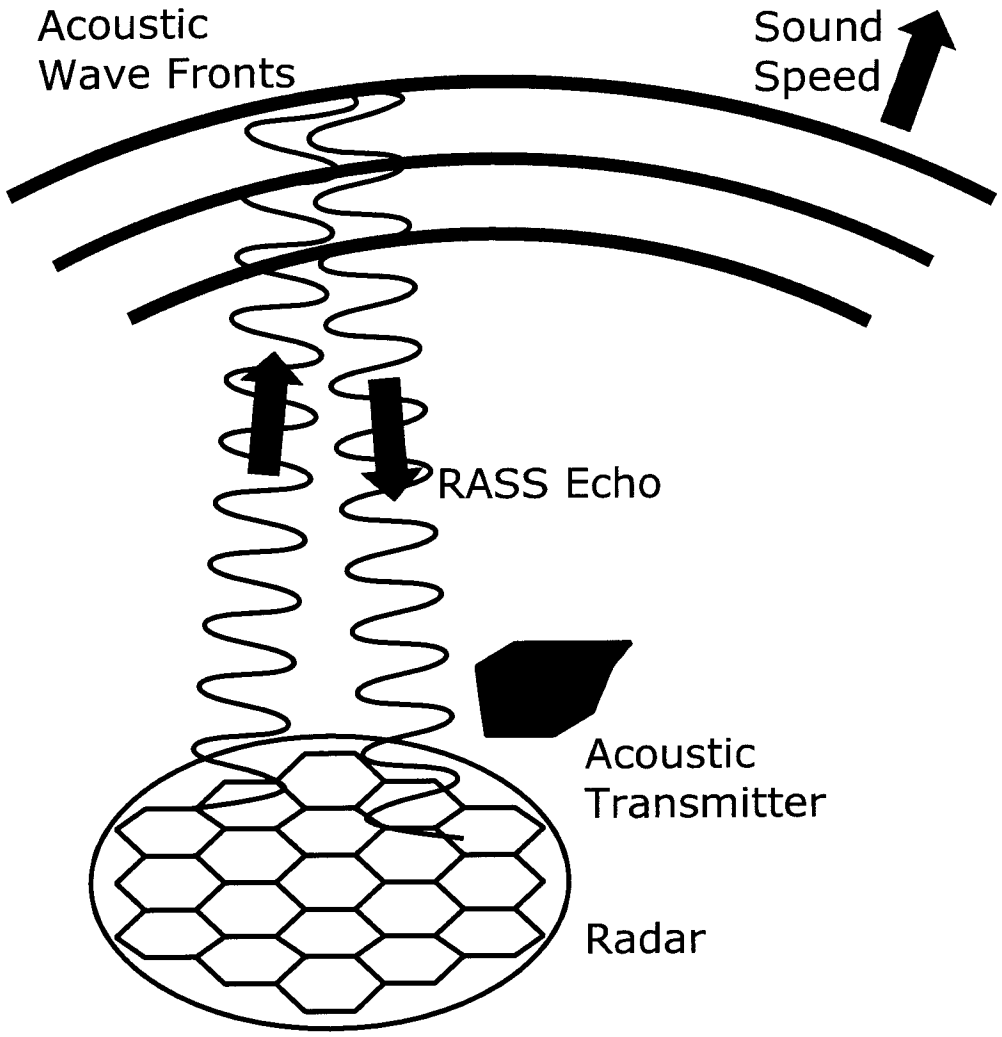

Figure 2.1: Basic principle of RASS.

scattered by acoustic wavefronts and determine their propagation speed. In the actual atmosphere, the apparent acoustic speed ($\vec{c_s}$) is the summation of the true acoustic speed ($\vec{c_a}$) and the background wind velocity ($\vec{v_r}$).

$$\vec{c_s} = \vec{c_a} + \vec{v_r}. \tag{2.35}$$

The acoustic speed (c_s) measured by RASS then becomes

$$c_s = \vec{c_a} \cdot \vec{n} + \vec{v_r} \cdot \vec{n}, \tag{2.36}$$

where $\vec{n}$ is a unit vector parallel to the radar beam direction. The atmospheric temperature can be derived as

$$c_a = K\sqrt{T}, \tag{2.37}$$

where K is a value which depends on the humidity. In a dry atmosphere we can describe K as

$$K = K_d = \sqrt{\frac{\gamma R}{M_d}} = 20.047 \ \ (\mathrm{m\ s^{-1}\ K^{-1/2}}), \tag{2.38}$$

where γ is the ratio of specific heat, R is a gas constant, and M_d is the mean molecular weight.

In a moist atmosphere, sound moves slightly faster than in a dry atmosphere, so Equation (2.37) becomes

$$T_v = \left(\frac{c_a}{K_d}\right)^2, \tag{2.39}$$

where T_v is the atmospheric virtual temperature which is the equivalent temperature for a dry atmosphere whose pressure and volume are the same as an actual moist atmosphere with a water vapor mixing ratio of q (kg kg^{-1}). The virtual temperature is defined as

$$T_v = (1 + 0.608q)T \tag{2.40}$$

2.2.2 Radar Equation for the RASS Echo

In this section, we briefly review the radar equation for the RASS echo given by *Marshall et al.* [1972]. The geometric configuration is shown in Figure 2.2. They applied a radiowave echo model of turbulence scattering to the RASS echo by assuming the following conditions.

- The atmospheric temperature is constant over the entire height, and the background wind is negligible.

- The radar beamwidth (θ_r) is sufficiently smaller than the acoustic beamwidth.
- The effects of any distortions of the acoustic wave fronts caused by turbulence are negligible.

Under these conditions, *Marshall et al.* [1972] derived the electric field of a RASS echo at ground level ($E_r(\vec{r_0})$) as

$$E_r(\vec{r_0}) = \frac{k_e^2}{2\pi} \int_v \frac{\exp(jk_e[\vec{r_0} - \vec{r}])}{|\vec{r_0} - \vec{r}|} \overline{n}(\vec{r}) E(\vec{r}) dv, \tag{2.41}$$

where $E(\vec{r})$ and $\overline{n}(\vec{r})$ are, respectively, the electric field and the atmospheric refraction index in the radar range volume, and $\vec{k_a}$ and $\vec{k_e}$ are, respectively, the acoustic and radio wavenumber.

Marshall et al. [1972] supposed that the following fluctuation of the refractive index exists in only a radar sampling volume.

$$\overline{n}(\vec{r}) = \begin{cases} A_a \exp(jk_a|\vec{r}|) & R - \frac{\Delta R}{2} \le r \le R + \frac{\Delta R}{2} \\ 0 & r < R - \frac{\Delta R}{2}, \quad r > R + \frac{\Delta R}{2}, \end{cases} \tag{2.42}$$

where A_a is the amplitude of the refraction index fluctuation.

If we assume the radar beam direction is vertical and the returned RASS echo projected onto the ground does not depend on ϕ_0, we can substitute Equation (2.42) to Equation (2.41) to obtain

$$\begin{aligned} E_r(r_0) &= \frac{k_e E_o A_a}{2\pi R} \int_0^{\theta_r} \sin\theta d\theta \int_0^{2\pi} \exp[jk_e(-r_0 \sin\theta \cos\phi)] d\phi \\ &\qquad \int_{R-\Delta R/2}^{R+\Delta R/2} \exp[j(2k_e + k_a)r] dr \qquad (2.43) \\ &= \frac{k_e^2 E_0 A_a}{2\pi R} (\pi\theta_r^2) \frac{2J_1(k_e r_0 \theta_r)}{k_e r_0 \theta_r} \int_{R-\Delta R/2}^{R+\Delta R/2} \exp[j(2k_e + k_a)r] dr, \qquad (2.44) \end{aligned}$$

where $J_1(x)$ is a first-order Bessel function of the first kind. Note that $\theta_r \ll 1$ is assumed in this equation. $E_r(r_0)$ is then proportional to $J_1(k_e r_0 \theta_r)/(k_e r_0 \theta_r)$.

The RASS echo intensity ($I(r_0)$) at the point of $\vec{r_0}$ can be expressed as

$$I(r_0) = \frac{|E_r(r_0)|^2}{Z_0} \propto \frac{J_1(k_e r_0 \theta_r)^2}{k_e^2 r_0^2 \theta_r^2 Z_0}, \tag{2.45}$$

where Z_0 is the characteristic impedance. The radar beamwidth is approximated well as

$$\theta_r = \frac{1.03}{D_r k_e} \pi, \tag{2.46}$$

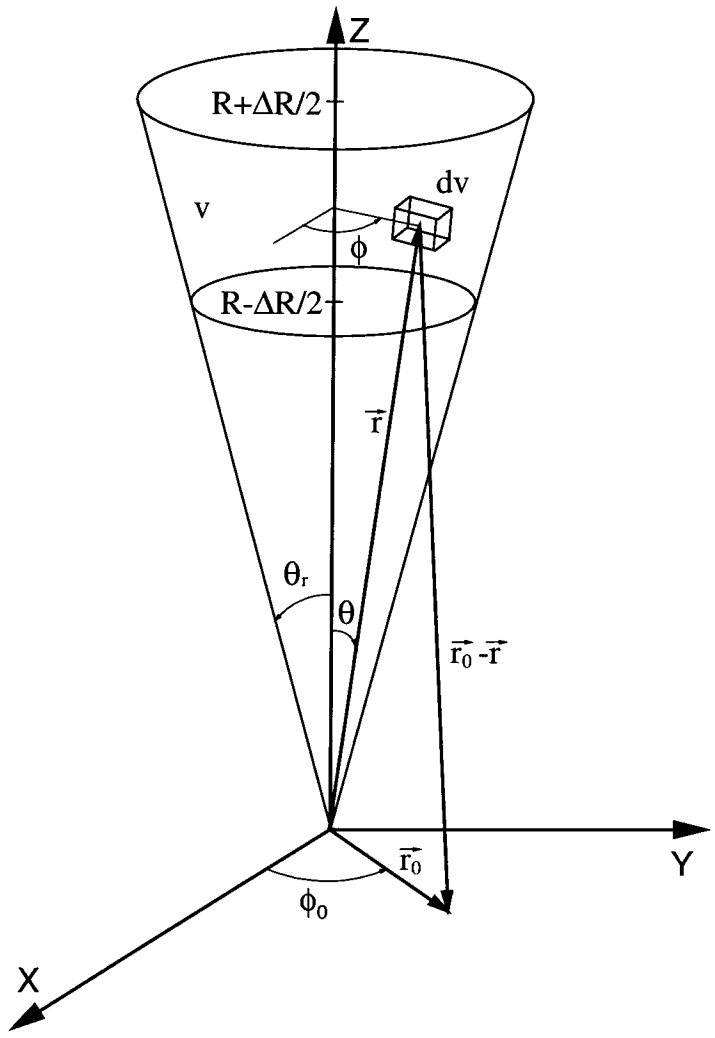

Figure 2.2: Geometric configuration for a radar equation representing RASS echoes. Both radar and acoustic waves transmitted from the origin have spherical wave fronts. The radar beamwidth is $2\theta_r$ and a radar sampling volume located at a range R has a range resolution of ΔR. A volume element dv at (r, ϕ, θ) in the sampling volume scatters the radar waves and produces a RASS echo at $(r_0, \phi_0, \pi/2)$ [*Marshall et al.*, 1972].

where D_r is the diameter of the transmitting antenna. Then, using Equations (2.45) and (2.46), $I(r_0)$ is written as follows:

$$I(r_0) = C_I \left\{ \frac{J_1(1.03\pi r_0/D_r)}{1.03\pi r_0/D_r} \right\}^2, \tag{2.47}$$

where C_I is a constant value. The distribution of $I(r_0)$ is shown in Figure 2.3. The echo intensity becomes the half-power of the peak value, where $r_0 \sim D_r/2$. The RASS echo at ground level will be circular in shape with the same diameter as the transmitter antenna. *May et al.* [1996] confirmed this empirically through an MU radar–RASS experiment using a single acoustic transmitter. However, in the actual RASS observation, multiple speakers are frequently used. $\overline{n}(\vec{r})$ with two acoustic sources located at $\vec{r_{s1}}$ and $\vec{r_{s2}}$, respectively, is

$$\overline{n}(\vec{r}) = \overline{n_1}(\vec{r} - \vec{r_{s1}}) + \overline{n_2}(\vec{r} - \vec{r_{s2}}), \tag{2.48}$$

where $\overline{n_1}(\vec{r} - \vec{r_{s1}})$ and $\overline{n_2}(\vec{r} - \vec{r_{s2}})$ are the refractive index fluctuations due to each acoustic source. The synthetic electric field of a RASS echo with multiple acoustic sources is the summation of each electric field when only each acoustic source is used. Therefore, when a multi-acoustic source is used, each speaker can cause interference between the RASS echoes.

2.2.3 Ray-tracing of Acoustic Wavefronts

In the case of the scattering caused by isotropic turbulence, the Bragg condition is satisfied in any beam direction. However, for the RASS measurements, refractive index fluctuations are artificially produced. Therefore, the wavenumber spectrum consists of only specific components corresponding to the acoustic wave vector. The Bragg condition with a mono-static Doppler radar can be described as

$$\vec{k_a} = 2\vec{k_e}. \tag{2.49}$$

The Bragg condition requires agreement on both the direction and the magnitude of the wavenumber vectors. We can rewrite the relationship as

$$|\vec{k_a}| = 2|\vec{k_e}|, \tag{2.50}$$

$$\vec{k_a} \;//\; \vec{k_e}. \tag{2.51}$$

Since temperature generally decreases with height in the troposphere, $|\vec{k_a}|$ increases with height. Thus, for actual observation, an FM chirped acoustic wave is transmitted whose sweep frequency range is adjusted to satisfy the Bragg condition throughout the observation height range.

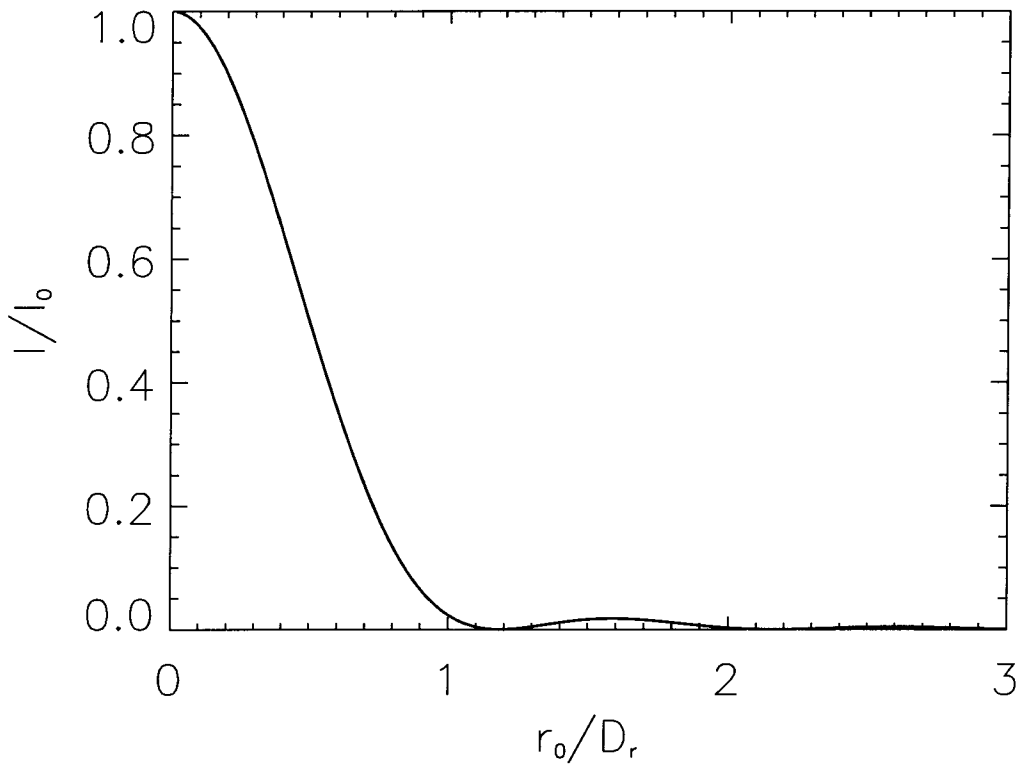

Figure 2.3: Distribution of the RASS echo intensity I. D_r is the radar diameter. The RASS echo intensity is normalized by I_0, the maximum value of I.

On the other hand, the propagation of acoustic waves is strongly affected by the background wind velocity and acoustic temperature, and this can greatly modified the shape of the acoustic wavefront. Therefore, the acoustic wavefronts may not always be perpendicular to the radar beam. *Masuda* [1988] applied a two-dimensional ray-tracing model of acoustic wavefronts to investigate the wavefront shape. They calculated acoustic wavefronts assuming that vertical gradients of horizontal wind ($\mathrm{d}u/\mathrm{d}z$) and acoustic speed ($\mathrm{d}c_a/\mathrm{d}z$) are invariable with time.

Figure 2.4a shows the acoustic wavefronts when $u = 0$ ms^{-1} and $\mathrm{d}c_a/\mathrm{d}z = -2.8 \times 10^{-3}$ s^{-1}. The shape of the acoustic wavefront becomes an ellipsoid, which is symmetrical relative to the z-axis. When $\mathrm{d}u/\mathrm{d}z = 9.0 \times 10^{-3}$s^{-1} and $\mathrm{d}c_a/\mathrm{d}z = -2.8 \times 10^{-3}$ s^{-1}, the acoustic wavefronts drifted downwind, and the longer axis of the ellipsoid slanted windward as shown as Figure 2.4b.

The effective scattering area is now defined as the region where the normal vector of acoustic wavefronts crosses the antenna surface and RASS echoes can be detected. Figure 2.5a and b shows the acoustic wavefronts in the effective scattering area when the wind shear is larger and smaller, respectively, than the absolute value of the acoustic speed gradient. Note that the acoustic transmitter is located r meters windward of the radar center.

When $r = 0$ m in Figure 2.5a, the effective scattering area is downwind of the narrow shape. During strong winds, Figure 2.5b shows the effective area moves both downwind and windward, but it is narrower than in the previous figure. In addition, as r increases, the effective scattering region becomes higher in Figure 2.5b. Thus, we can extend the height range of RASS observation by directing the radar beam windward. Moreover, when the horizontal wind velocity is very high ($\mathrm{d}u/\mathrm{d}z \geq -\mathrm{d}c_a/\mathrm{d}z$), locating the acoustic transmitters windward of the radar improves performance.

In actual observation, three-dimensional ray-tracing of the acoustic wavefronts is applied to the MU radar–RASS. The group velocity of the acoustic waves is described as

$$\frac{\partial \omega}{\partial k_i} = \frac{dp_i}{dt}, \tag{2.52}$$

where k_i and ω are the wavenumber and the angular frequency of an acoustic wave, respectively, and p_i is the ray point coordinates. Note that i represents the Cartesian coordinates (x, y, z). Moreover, the acoustic wave must satisfy the following relationship:

$$\frac{\mathrm{d}k_i}{\mathrm{d}t} = -\frac{\partial \omega}{\partial p_i}. \tag{2.53}$$

We can then numerically solve Equations (2.52) and (2.53) to get temperature and wind velocity profiles if we assume the temperature and wind velocity of the

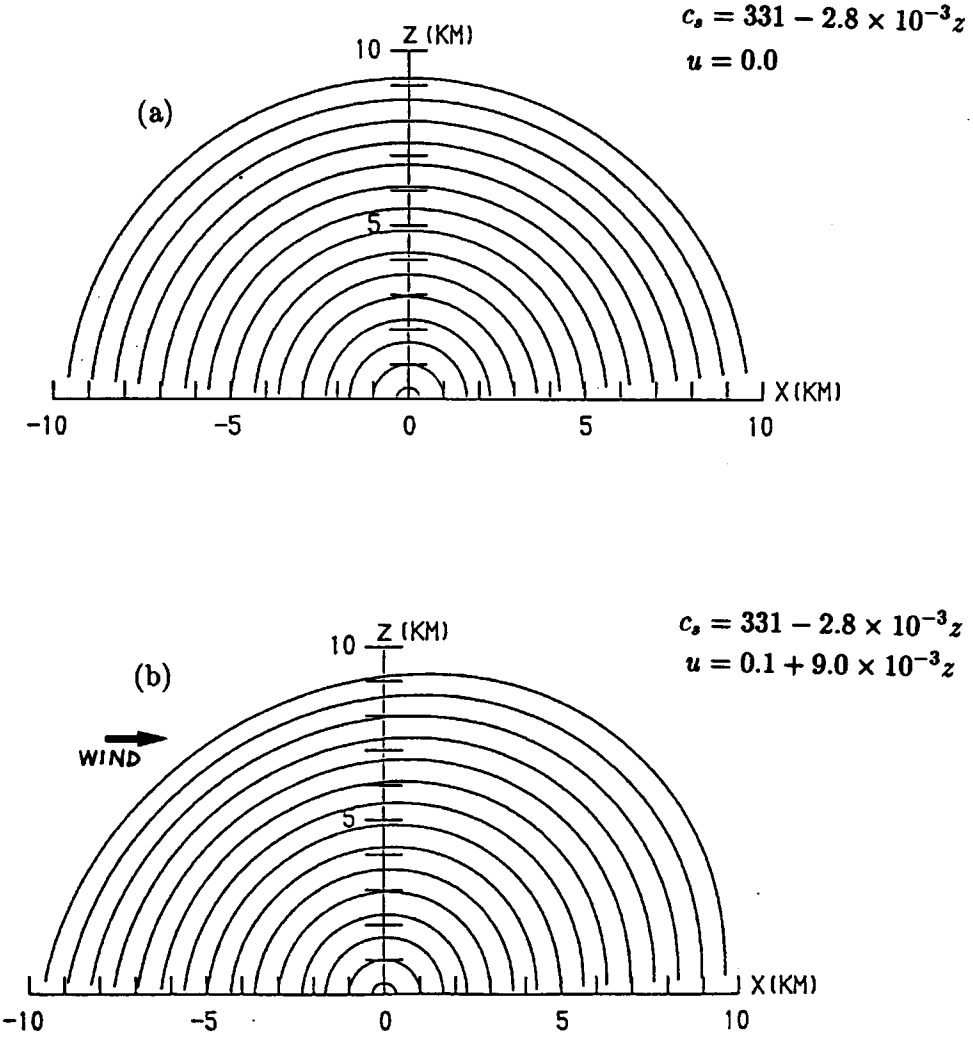

Figure 2.4: Vertical cross-section of acoustic wavefronts calculated every three seconds by the ray-tracing method. X and Z show, respectively, horizontal distance and altitude. An acoustic source is located at the origin. (a) represents the windless condition and $\mathrm{d}c_a/\mathrm{d}z(< 0)$ is constant. In (b), $\mathrm{d}c_a/\mathrm{d}z(\neq 0)$ and $\mathrm{d}u/\mathrm{d}z$ is constant [*Masuda,* 1988].

(a)

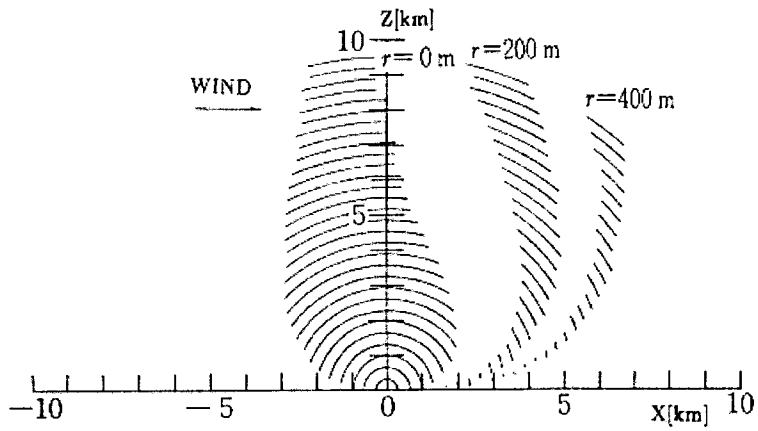

(b)

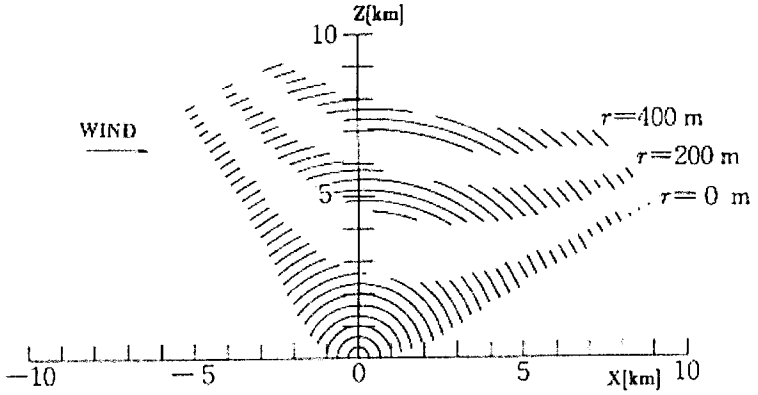

Figure 2.5: Vertical cross-sections of the effective backscatter region under various background conditions. r is defined as the distance between the center of the radar and an acoustic transmitter placed windward of the radar. (a) $dc_s/dz = -2.8\times 10^{-3}$ s^{-1}, $du/dz = 5.6\times 10^{-4}$ s^{-1}, (b) $dc_s/dz = -2.8\times 10^{-3}$ s^{-1}, $du/dz = 5.6 \times 10^{-3}$ s^{-1} [*Masuda*, 1988].

atmosphere is horizontally constant. In actual MU radar–RASS observation, the beam direction and position of the acoustic source is decided based on the results of ray-trace calculations using wind velocity profiles obtained by turbulence echo observation and the temperature obtained from simultaneous radiosonde results.

2.3 The MU Radar–RASS System

In this section, we describe the MU radar and its incorporation with RASS. Typical results from MU radar–RASS observation are also examined.

2.3.1 The MU Radar

The MU radar is a monostatic pulse Doppler radar operating at 46.5 MHz that has an active phased array system. (Basic parameters of the MU radar are given in Table 2.1.) The MU radar was completed in November 1984 at the Shigaraki MU Observatory (36°51' N, 146°06' E, 375 m MSL) and has been in operation for 18 years. Its observations have greatly contributed to studies of various dynamical phenomena in the troposphere, the middle atmosphere, and the upper atmosphere.

The peak and average transmitting power of the MU radar is 1 MW and 50 kW, respectively. The shortest sampling interval is 1 μs, corresponding to 150 m range resolution. The active phased array system of the MU radar consists of a circular array of 475 Yagi antennas. The one-way half-power half-width of the radar beam width is about 1.87° when the arrays are fully employed. The main antenna lobe of the MU radar can be steered within each inter-pulse-period (IPP) to a direction within a zenith angle of about 30°. The step angle for the zenith and azimuth angles is 1–2° and 5°, respectively.

The antenna array is divided into 25 sub-arrays, and the signal received by each sub-array can be sent to four independent receiver (RX) channels. Because of this MU radar's capability, two receiver channels can be used for RASS observation: one for the normal radar detection of turbulence echoes and the other for the detection of RASS echoes with the local reference signal appropriately shifted in order to detect the Doppler spectrum caused by sound waves travelling at the sound spread near the center of a narrow frequency window.

2.3.2 Signal Processing with the MU Radar

This section describes the signal processing applied to turbulence echo observation with the MU radar. Sinusoidal waves generated by an oscillator are mod-

Table 2.1: Parameters of the MU radar [*Fukao et al.*, 1985, 1990].

Parameter	Value
Location	Shigaraki, Shiga, Japan (34°51′N, 136°06′E)
Radar system	monostatic pulse radar; active phased array system
Operational frequency	46.5 MHz
Antenna	circular array of 475 crossed Yagi antennae
aperture	8330 m^2 (103 m in diameter)
beam width	$\simeq$1.87° (one-way half-power half-width)
steerability	steering is completed within the switching time from receiver to transmitter.
beam directions	1657; 0–30° off zenith angle
polarizations	linear and circular
Transmitter	475 solid-state amplifiers (TR modules; each with output power of 2.4 kW peak and 120 W average)
peak power	1 MW (maximum)
average power	50 kW (maximum duty ratio is 5%)
bandwidth	1.65 MHz (maximum)
inter-pulse period	400 μs to 65 ms (variable)
Receiver	
bandwidth	1.65 MHz (maximum)
dynamic range	70 dB
IF	5 MHz
A/D converter	14 bits $\times$ 8 channels
Pulse compression	binary phase coding up to 32 elements; Barker and complementary codes

Table 2.2: Typical parameters for the MU radar observation in the troposphere and lower stratosphere.

Turbulence Echo Observation		
	Tropospheric Mode	Stratospheric Mode
range (km)	0.15–19.20	5.10–24.15
range resolution (m)	150	150
sample range number	128	128
inter-pulse period(μs)	400	400
sub-pulse length (μs)	1	1
pulse compression bit	1	16
number of beams	5	5
number of RX channels	1	1
coherent integrations	38	38
number of FFT points	128	128
incoherent integrations	5	6
observation duration (s)	49	58
beam direction	(0°, 0°), (0°, 10°), (90°, 10°),	
(azimuth angle, zenith angle)	(180°, 10°), (270°, 10°)	

ulated by pulse compression and transmitted into the atmosphere. The backscattered signal is then detected by the superheterodyne quadrature detector.

The signal is converted to a digital signal by an A/D converter, and the digital signal is then integrated to increase S/N. This process is called coherent integration. The coherently integrated complex signal is further Fourier transformed to the Doppler spectrum. Then the derived spectrum is incoherently integrated to make it easier to detect. Finally, the Doppler parameters – the Doppler shift, spectral width, and echo power – are estimated.

Consider an example of the Doppler spectra of turbulence echoes derived from MU radar observation. Table 2.2 shows the typical parameters for turbulence echo observation in the troposphere and lower stratosphere. The parameters for both the tropospheric and lower stratospheric mode are similar except for the pulse code, start range, number of coherent integrations, and number of incoherent integrations. Figure 2.6 shows a typical Doppler spectrum observed with the beam zenith angle of 10° at 5.7 km. A signal can be recognized by the increased broadening around 5 ms^{-1}. Random fluctuations that broaden the entire frequency range are caused by white noise. The sharp peak around 0 ms^{-1}

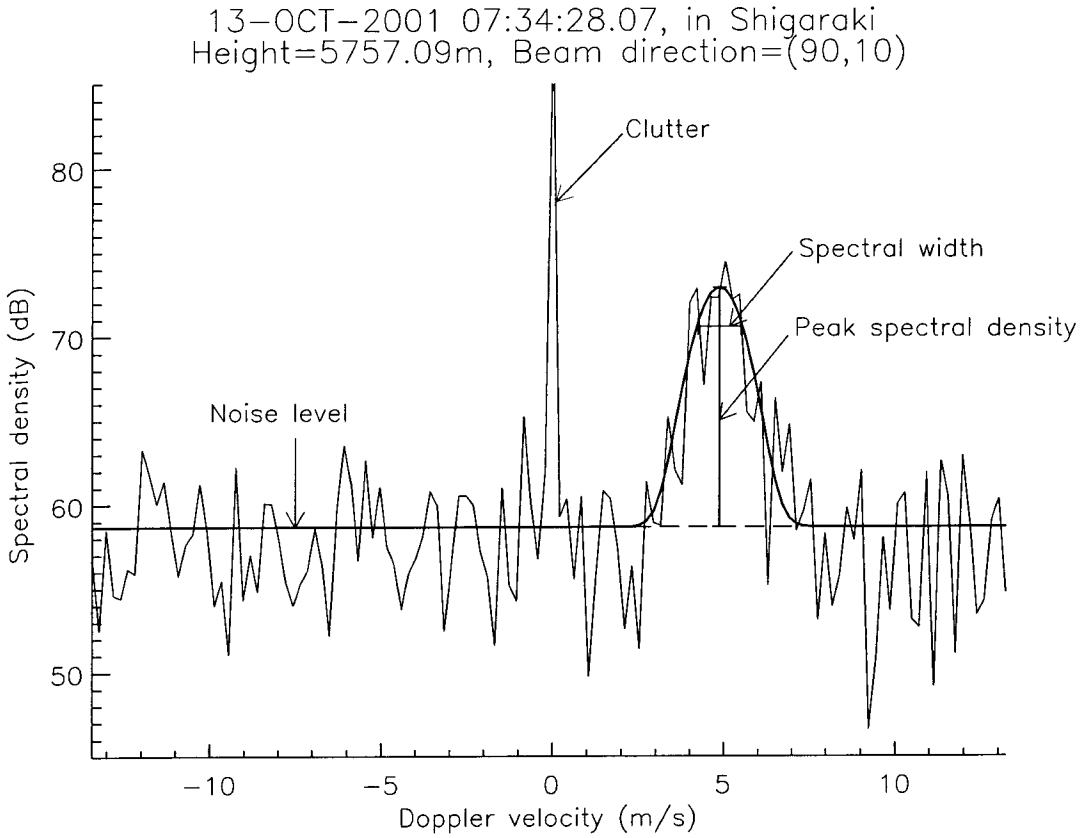

Figure 2.6: Typical example of a Doppler velocity spectrum observed by the MU radar at 5 km at 7:34 LT on October 13, 2001. The beam direction was (azimuth angle, zenith angle) = (90°, 10°). The thick line shows the result of a least-squares fitting to the Gaussian function.

is caused by ground clutter. The mean noise level is estimated from the Doppler spectrum. The Doppler parameters are detected by applying least-squares fitting according to the Gaussian function to the observed spectrum. Note that the ground clutter is removed before the spectral parameters are estimated. The derived spectral parameters are used to study the atmospheric phenomena.

2.3.3 The MU Radar–RASS System

The MU radar–RASS is capable of monitoring a T_v profile and turbulence echoes from 1.5 km to the near tropopause with an accuracy of T_v within 0.5 K [*Matsuura et al.*, 1986; *Adachi et al.*, 1993; *Tsuda et al.*, 1989, 1994].

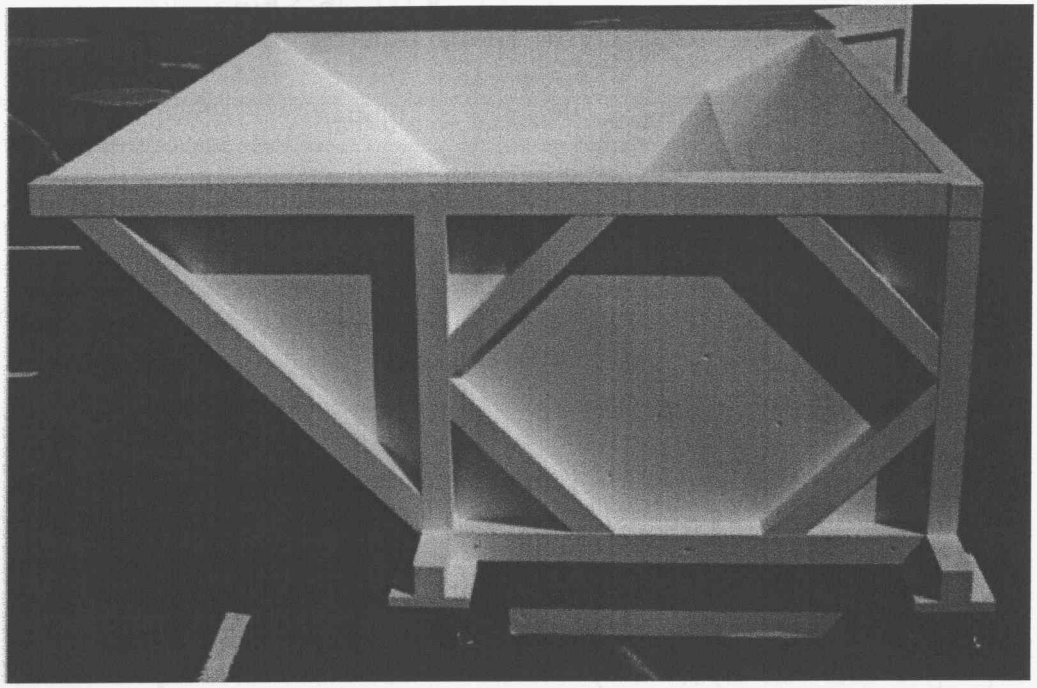

Figure 2.7: The hyperbolic horn speaker system. The speaker is mounted on a wooden frame with casters.

Three types of acoustic transmitters have been used for the MU radar–RASS: a pneumatic transducer with a hyperbolic horn, an electro-dynamic loudspeaker with a standard enclosure, and an electro-dynamic loudspeaker with a hyperbolic horn. The pneumatic transducer which can produce a transmitted acoustic wave as strong as 147 dB, allowing RASS echoes to be detected up to 22 km, was developed some time ago [*Matsuura et al.*, 1986].

However, ray-tracing results indicated that an acoustic transmitter should be placed windward of the radar antenna. Under disturbed meteorological conditions, the wind velocity tends to fluctuate greatly causing considerable changes in the best position for the acoustic source. To enable continuous observation even under disturbed conditions, several acoustic sources composed of a loudspeaker unit and an amplifier were located around the radar antenna. The output power of a pair of these loudspeaker units was 132 dB. Because of the lower acoustic power, though, the observation height was limited to below about 8 km.

To monitor temperature throughout the troposphere and the lower stratosphere a more powerful speaker system was needed. Thus, an original horn speaker was designed [*Adachi*, 1996]. Figure 2.7 shows a photo of the devel-

oped enclosure. This provided a maximum sound pressure of about 140 dB. A total of 20 horn speakers were located around the MU radar antenna, as shown in Figure 2.8, with 14 speakers close to the radar antenna and six other speakers located 100–200 m west of the antenna. [*Adachi*, 1996].

As explained in section 2.2.2, acoustic signals transmitted from multiple transmitters have slightly different wavenumber vectors. Thus, acoustic waves transmitted by different speakers can satisfy the Bragg condition in the radar sampling volume. However, the received RASS echo could suffer from interference due to the overlapping of these scattered radiowaves, thus reducing the intensity of the RASS echoes, if the received radiowaves are not in-phase (see Appendix A.). A control system was therefore developed that would change the initial phase of the individual hornpeakers to make the wavefronts roughly in-phase.

This thesis includes MU radar–RASS data obtained in August 1995, November 1997, and July 1999. The pneumatic transducer and loudspeakers were used in 1995, and the hyperbolic horn speakers were used in 1997 and 1999.

2.3.4 Temperature Measurements with the MU radar–RASS

MU radar–RASS measurement has been carried out for 10 years. In this section, we look at examples of the temperature profiles obtained during this time. Profiles of three components of wind velocity and temperature were obtained with a time and height resolution of 3.6 minutes and 150 m, respectively, over four days from 3:00 LT (hereafter, LT means Japan standard time) on August 2 to 00:00 LT on August 6, 1995. During this campaign, radiosondes were launched every 6 hours. Figure 2.9 shows successive T_v profiles observed every 3.6 minutes by RASS with a height resolution of 150 m. The minimum temperature near the tropopause appeared at about 16–17 km. Although some data points from above 14 km were missing, we were able to continuously monitor the temperature structure up to the tropopause. Simultaneous radiosondes were launched at the times indicated by triangles in the figure. Temperature profiles obtained with the MU radar–RASS show a small peak at about 8 km, which moved downward over time. Above 14 km, the amplitude of temperature fluctuation increased, and short-term fluctuations which could not be detected by the simultaneous radiosondes were observed.

The tropopause height (h_{trop}) was also determined. According to the World Meteorological Organization (WMO) definition, this is the lowest height at which the temperature lapse rate, $\mathrm{d}T/\mathrm{d}z$, falls to less than 2 K km^{-1}, and the $\mathrm{d}T/\mathrm{d}z$ within the next 2 km does not exceed -2 K km^{-1}. Figure 2.10 shows the trop-

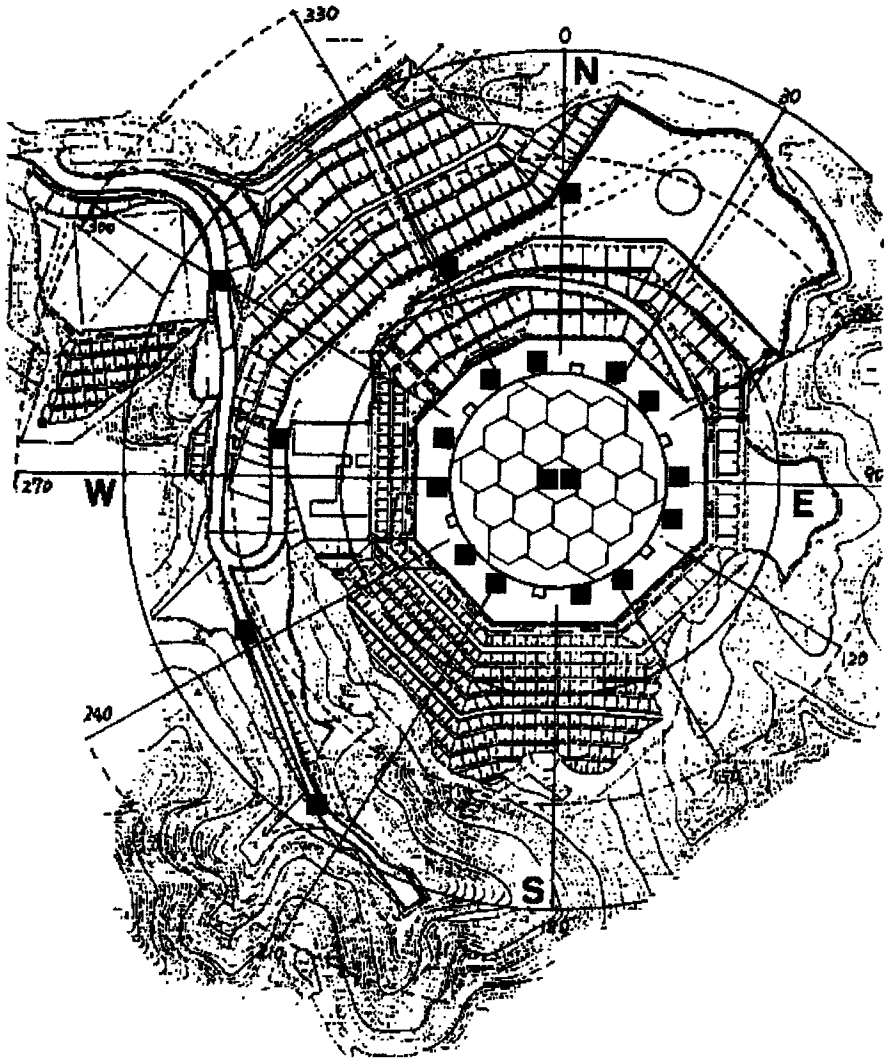

Figure 2.8: The positions of electro-dynamic loudspeakers with the hyperbolic horn. The location of each acoustic source is indicated by the black box.

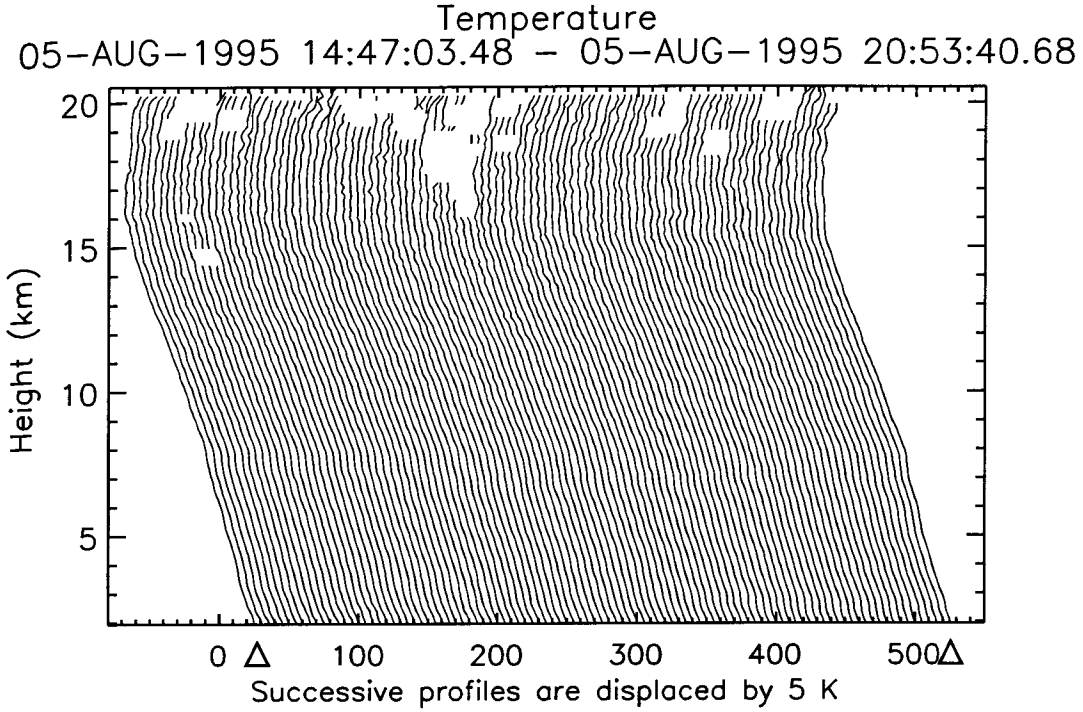

Figure 2.9: Successive temperature profiles observed every 3.6 minutes with the MU radar-RASS from 14:47 to 20:53 LT on August 5, 1995. Triangles indicate the times at which radiosondes were launched.

opause height every 3.6 minutes as indicated by the MU radar–RASS. The tropopause height showed a very rapid stair-like variation from 15.5 to 17.5 km with an r.m.s. deviation of 0.81 km. Figure 2.11 shows a time-height section of the transient component of temperature (T') after subtracting the time mean value over four days. Warm and cold colors correspond respectively to positive and negative T'. It varied by about 2 K in the lower atmosphere below 8 km, and there is a clear structure moving downward. At 10–15 km, the amplitude was smaller, but increased again above about 15 km.

The MU radar–RASS therefore offers a great advantage in that it enables us to monitor successive temperature profiles over the entire troposphere and into the lower stratosphere with high time and height resolution. The high-resolution temperature data thus obtained will be discussed in Chapters 4, 5, and 6.

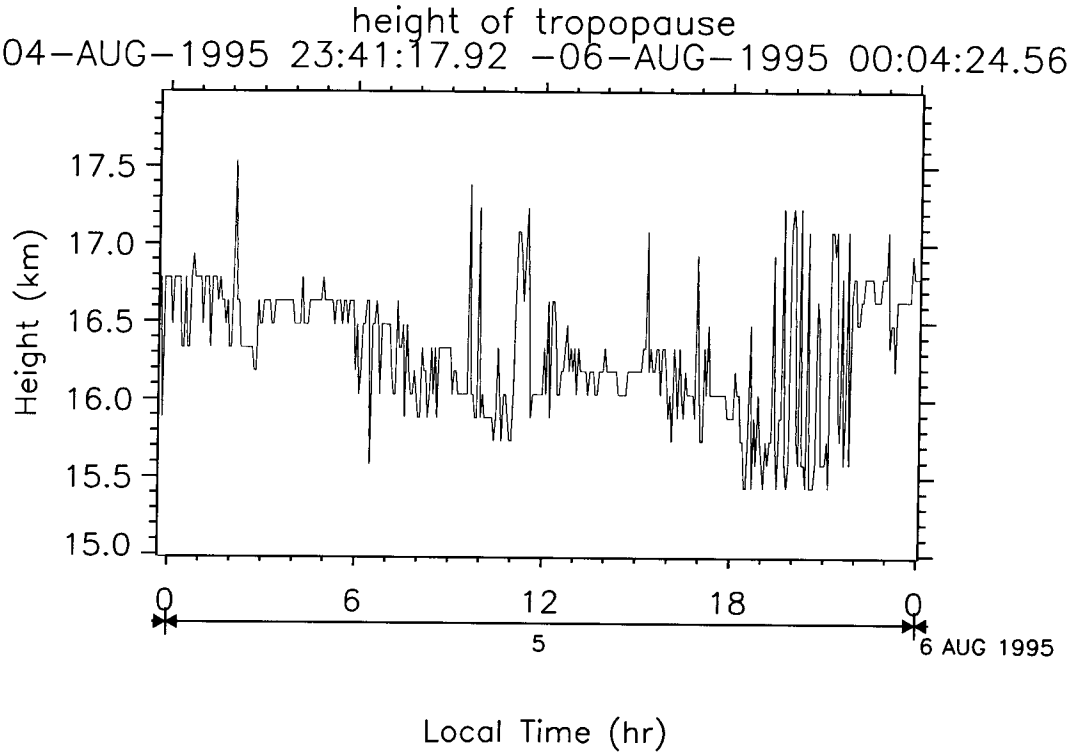

Figure 2.10: Time variation of the tropopause height measured with the MU radar–RASS from 0:00 LT on August 5 to 0:00 LT on August 6.

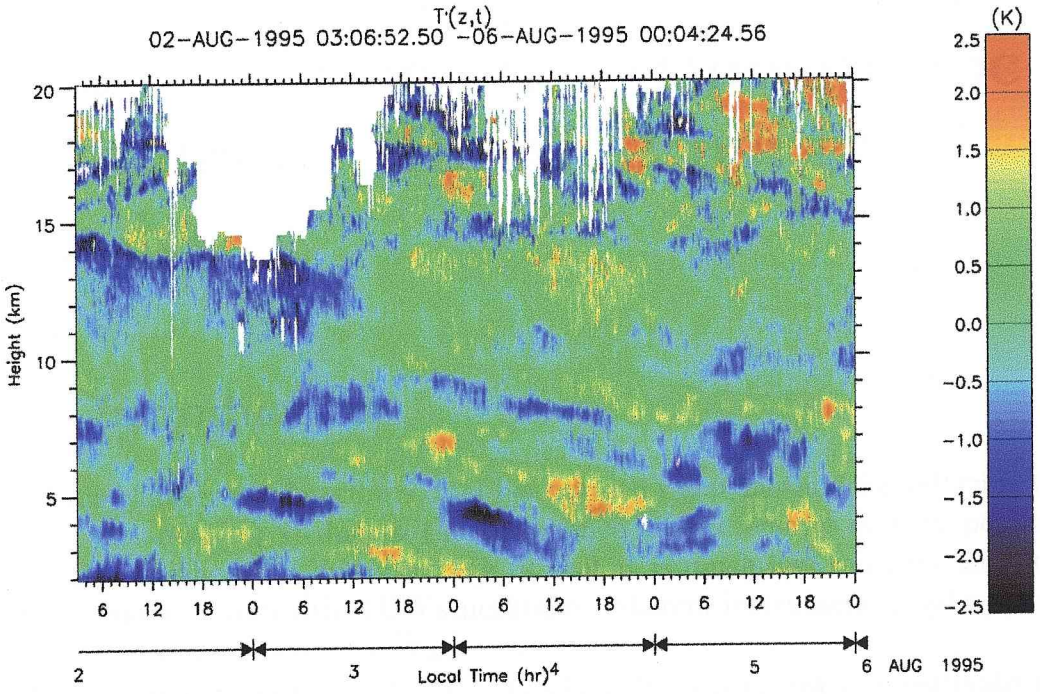

Figure 2.11: Time-height temperature section with the mean temperature profile removed. Obtained with the MU radar–RASS from 3:00 LT on August 2 to 0:00 LT on August 6, 1995.

Chapter 3

Dual-Beamwidth Radar Method for Measuring the Atmospheric Turbulence Kinetic Energy Density

3.1 Introduction

In this chapter we describe a dual-beamwidth radar method for inferring the velocity variance (σ_{turb}) due to the turbulence kinetic energy density per unit mass. This method has an advantage in that it is much less sensitive than the standard single-beamwidth (1BW) method to inherent instrumental correction of the observed velocity variance, σ_{obs}.

As explained in section 2.1.3, two methods have been used to estimate the turbulence energy dissipation rate: the echo power and the Doppler spectral width methods. In the returned power method (the echo power method) radar data are analyzed by means of a theory that involves several assumptions and parameters [*VanZandt et al.*, 1978; *Hocking and Mu*, 1997]. The theory of the spectral width method requires fewer assumptions, but the observed spectral width is affected by certain broadening effects. However, these effects are removed by using the horizontal wind velocity and shear in this method. The difficulty is that large values for the horizontal wind velocity or shear can make a small error in the estimation of the broadening effects comparable in magnitude to the observed width. To obviate these difficulties, the dual-beamwidth (2BW) spectral width method uses effectively simultaneous observations of nested sampling volumes with two different beamwidths.

In general, σ_{obs} is related to σ_{turb} and σ_{corr} as shown by Equation (2.30). Moreover, *Nastrom* [1997] described the variance caused by beam and shear broadening as Equation (2.34). The 1BW method consists of evaluating $\sigma^2_{corr} = \sigma^2_{beam+shear} + \sigma^2_{wave}$ by evaluating $\sigma^2_{corr} = \sigma^2_{beam+shear}$ with Equation (2.34) (or a generalization of it for a more sophisticated treatment of the observation volume), estimating σ_{wave} (which is usually negligible in the lower atmosphere according to *Nastrom and Eaton* [1997]), and then subtracting σ^2_{corr} from σ^2_{obs} to obtain σ^2_{turb}.

In this chapter, the underlying theory of the 2BW method is explained. The 2BW and 1BW methods are then compared using σ_{obs} between 5.0 and 7.5 km as measured by the MU radar [*VanZandt et al.*, 2002].

3.2 Theoretical Development

VanZandt et al. [1999] noted that since the dominant terms in $\sigma^2_{beam+shear}$ are proportional to θ_r^2, then σ^2_{corr} also be approximately proportional to θ_r^2. Thus, if σ^2_{obs} is measured simultaneously in nested sampling volumes with two different beamwidths, θ_a and θ_b (with a and b denoting the narrower and broader beamwidths, respectively), the two simultaneous equations of Equation (2.29) for σ^2_{obs} can be solved for σ^2_{turb} and σ^2_{corr}:

$$\sigma^2_{turb} = \frac{(\theta_b^2\sigma^2_{obs-a} - \theta_a^2\sigma^2_{obs-b})}{(\theta_b^2 - \theta_a^2)}, \tag{3.1}$$

$$\sigma^2_{corr-a,b} = \frac{\theta^2_{a,b}(\sigma^2_{obs-b} - \sigma^2_{obs-a})}{(\theta_b^2 - \theta_a^2)}. \tag{3.2}$$

This method assumes that the mean value of σ^2_{turb} is the same in the two nested sampling volumes. This may be a good approximation if turbulence fills the sampling volumes, but in other cases, such as when the reflectivity is from a thin layer, the mean values of σ^2_{turb} may differ. The effect of thin layers of turbulence is the subject of a separate study.

The principal advantage of the 2BW method is that it is independent of the model for σ^2_{corr} as long as the terms in σ^2_{corr} that are not proportional to θ_r^2 are negligible or can be estimated. Also, the 2BW method takes into account ALL beam-broadening processes that are proportional to θ_r^2, whether or not they are included in $\sigma^2_{beam+shear}$ and σ^2_{wave}. For example, for a three-dimensional pulse volume there are small terms proportional to $V(\mathrm{d}V/\mathrm{d}z)R$ and $R^2(\mathrm{d}V/\mathrm{d}z)^2$. Since these terms are proportional to θ_r^2, they are implicitly included in σ^2_{corr} in this way.

3.3 MU Radar Observations in 2000

During the year 2000, the campaigns were conducted at the MU radar in February, May and August. In particular, the antenna is divided into 25 sub-arrays, which during these experiments were configured into three different groups consisting of 25, 12, and 7 sub-arrays, with θ_r of 1.870°, 2.650°, and 3.460°(0.033, 0.046, and 0.060 radian), respectively. Each of the 25 sub-arrays consists of 19 Yagi antennas, which were separately phased to form beams toward the vertical and toward 10° zenith angles in the cardinal azimuths.

Spectra for all 15 beamwidth/beam-direction pairs were obtained approximately every 3 minutes in February and every 5 or 6 minutes in May and August. By phase steering between each pulse, observations were made essentially simultaneously in each of the five directions for the narrow beamwidth. Then this process was repeated for the medium and the broad beamwidths.

The power-aperture product decreased from 4×10^8 to 3×10^7 in going from the narrowest to the broadest, so that useful data were typically obtained to 14 km for the narrow beamwidth, about 12 km for the medium, and 9 km for the broadest. Pertinent radar settings for February, May, and August, respectively, were: inter-pulse-period = 400, 640, 640 μs; number of Doppler spectral points = 128, 128, 128; number of coherent integrations = 38, 38, 38; number of incoherent integrations = 6, 3, 3; range gate width = 150, 300, 300 m HPFW; pulse compression bits = 16, 16, 16. σ_{obs} was determined from each Doppler spectrum by the Gaussian fitting method [*Fukao et al.*, 1990].

Results will be given for three time periods in August, May, and February 2000, with small wind speeds (< 10 ms^{-1}) in August, moderate speeds in May, and large speeds (up to ~ 60 ms^{-1}) in February. Since the instrumental corrections given by Equation (2.34) depend on the wind speed and shear, case studies under such different conditions may illuminate both the 1BW and 2BW methods.

3.3.1 Weak Wind Condition on August 10, 2000

The mean vertical profiles of σ^2_{corr} and σ^2_{turb} over the five hours from 7:00–12:00 LT are shown in Figure 3.1a, b, and c for the 1BW method with the 25-group and in Figure 3.2a, b, and c for the 2BW method for the combination of the 25- and 7-group pair. The mean horizontal winds during this period were about 11 ms^{-1} at 5 km and decreased steadily to about 2 ms^{-1} at and above 6.5 km with correspondingly small vertical shears. Thus, above 6.5 km, σ^2_{corr} was small and $\sigma^2_{turb} \simeq \sigma^2_{obs}$ for both the single-beam and dual-beam methods. The profiles for the cardinal azimuths agree within the statistical errors. Below 6 km, σ^2_{corr} is not negligible, so $\sigma^2_{turb} < \sigma^2_{obs}$. For the 2BW results there is more scatter among the

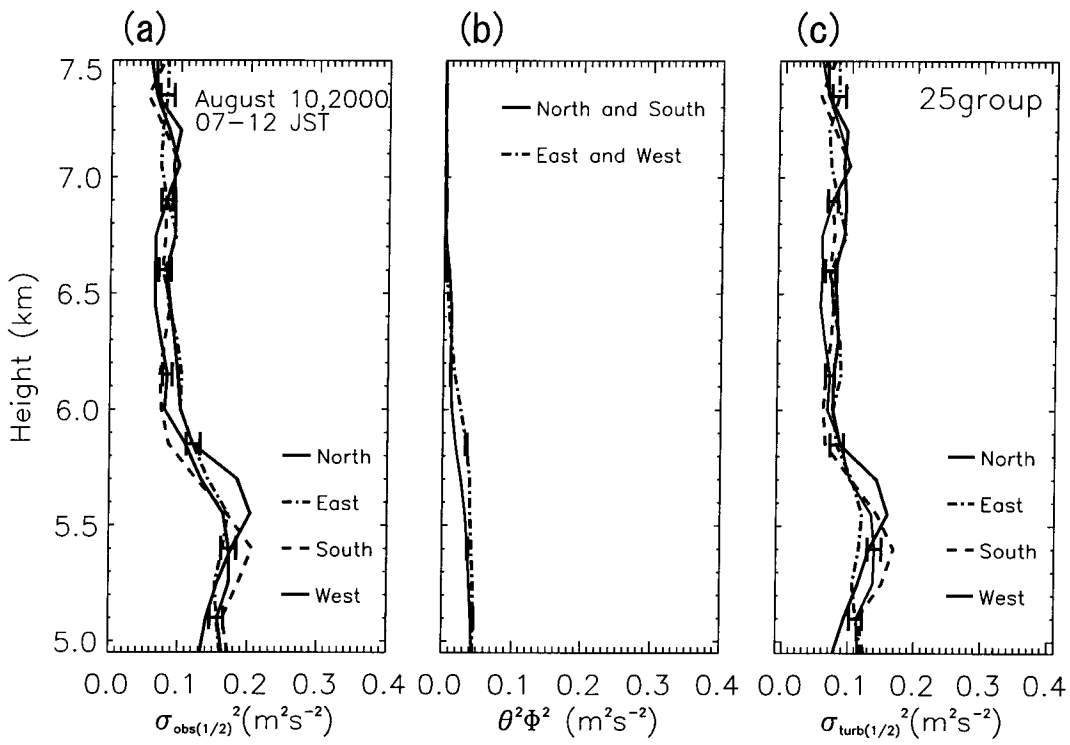

Figure 3.1: Data profiles for 7–12 LT on August 10, 2000, for the 1BW method, with the 25-subarrays group. (a) Observed spectral widths σ_{obs}^2 in the cardinal azimuths. (b) σ_{corr}^2 for the meridional (North and South) and zonal (East and West) beams. (c) $\sigma_{turb}^2 = \sigma_{obs}^2 - \sigma_{corr}^2$ for the cardinal azinmths.

beams (due to the greater scatter among the 7-group σ_{obs}^2. Values of σ_{turb}^2 the 2BW method are significantly smaller than from the 1BW method.

Figure 3.3 shows time series of σ_{turb}^2 averaged over hour time segments and from 5.25 to 6.75 km from the 1BW method and the 2BW method for both the 25-7 and 25-12 group pairs. The three time series are significantly correlated, with a maximum correlation of 0.91 between results from the 1BW and the 2BW 25-7 groups. Winds near 6 km were relatively light (< 10 ms^{-1}) throughout this period. The mean values of σ_{turb}^2 during this period ranged up to about 0.20 m^{2}s^{-2} with median values of about 0.07 m^{2}s^{-2} between 6 and 7.5 km. Error bars showing the standard deviation of σ_{obs}^2 versus time are plotted only for the north and east beams, since those for the south and west beams are similar.

3.3.2 Moderate Wind Condition on May 1, 2000

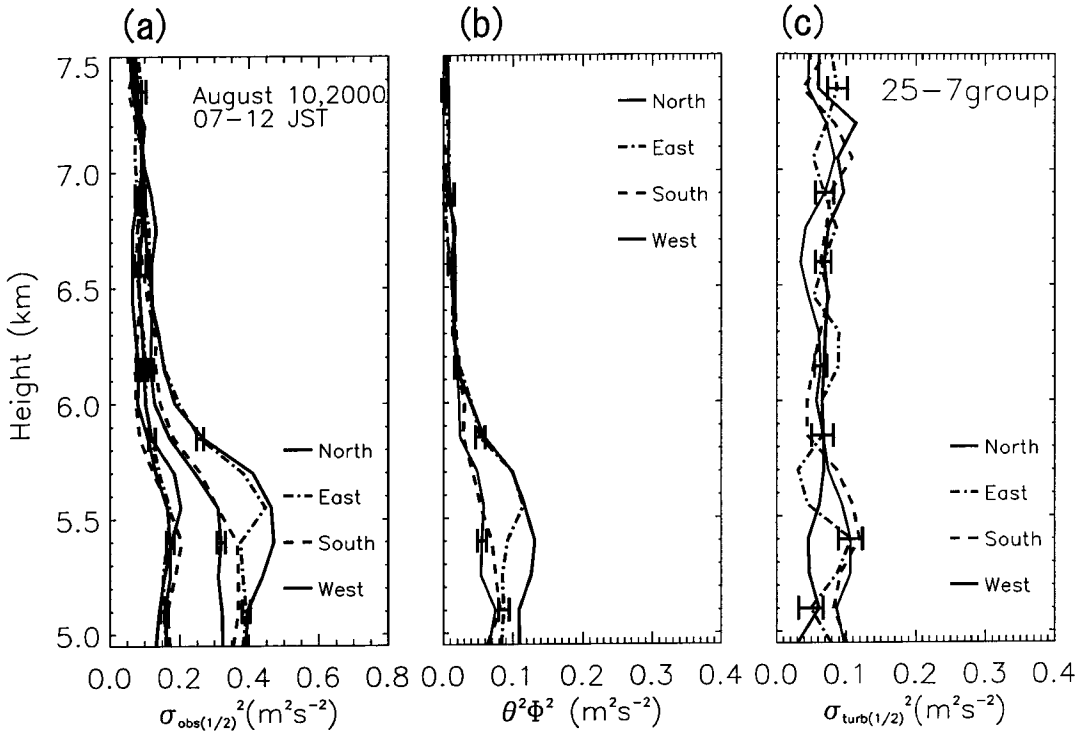

Figure 3.2: Data profiles for 7–12 LT on August 10, 2000, for the 2BW method, with the 25- and 7-group pair. (a) As in Figure 3.1 except there are σ_{obs}^2 profiles for both the 25-group (left-hand set) and the 7-group (right-hand set). (b) and (c) as in Figure 3.1.

During the period 17:00–22:00 LT on May 1, 2000, the mean horizontal winds increased with altitude from about 13 ms^{-1} at 6 km to 19 ms^{-1} at 7.5 km. Figure 3.4 shows the cardinal-azimuth profiles of σ_{turb}^2 determined by the 1BW method. Figure 3.4 for the 2BW 25-7 groups shows the σ_{turb}^2 profile only from the south azimuth (at the other azimuths the 7-group S/N was too small for meaningful analysis). The 1BW and 2BW profiles agree very well, except between 6.1 and 6.5 km. During this period typical values of σ_{turb}^2 between 6 and 7.5 km were about 0.15 m^2s^{-2}.

3.3.3 Strong Wind Condition on February 25, 2000

During the period 17:00–23:00 LT on February 25, 2000, the mean zonal winds were strong, with the total horizontal wind increasing from 28 ms^{-1} at 5 km to 58 ms^{-1} at 7.5 km. Figures 3.5a and 3.6a show mean profiles of σ_{obs}^2

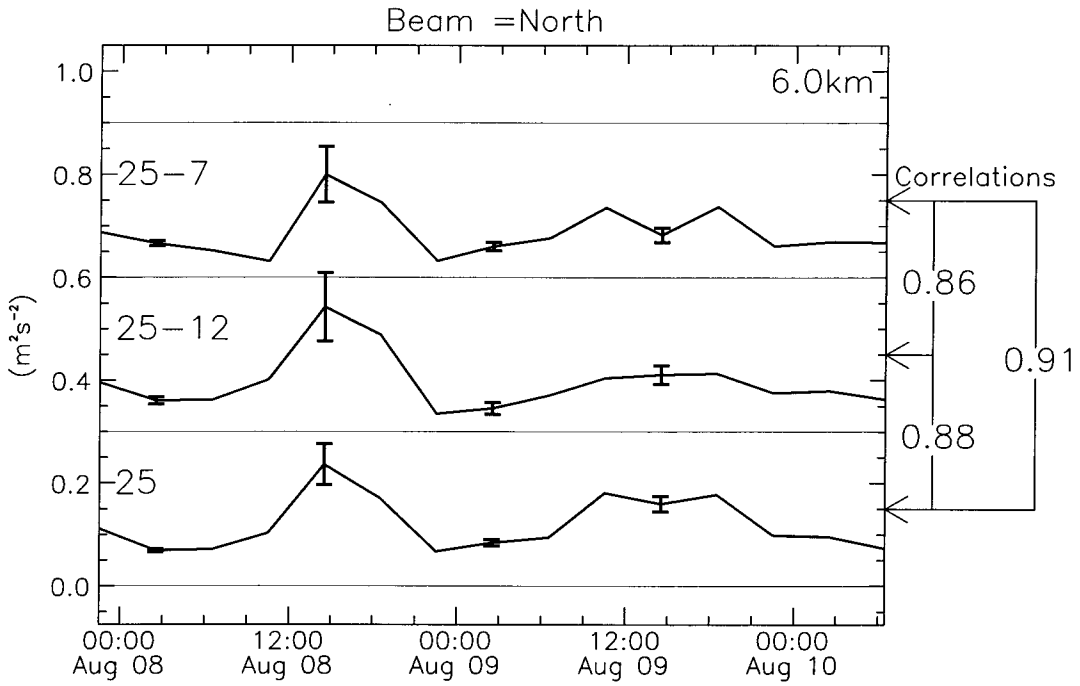

Figure 3.3: Time series of σ^2_{turb} averaged over 4-hour time segments from 23:00 LT on August 7 to 7:00 LT on August 10 and from 5.25 to 6.75 km. Top panel: 25- and 7- group pair 2BW method; Middle panel: 25- and 12-group pair 2BW method; Bottom panel: 25-group 1BW method. The correlation coefficients between the panels are given on the right.

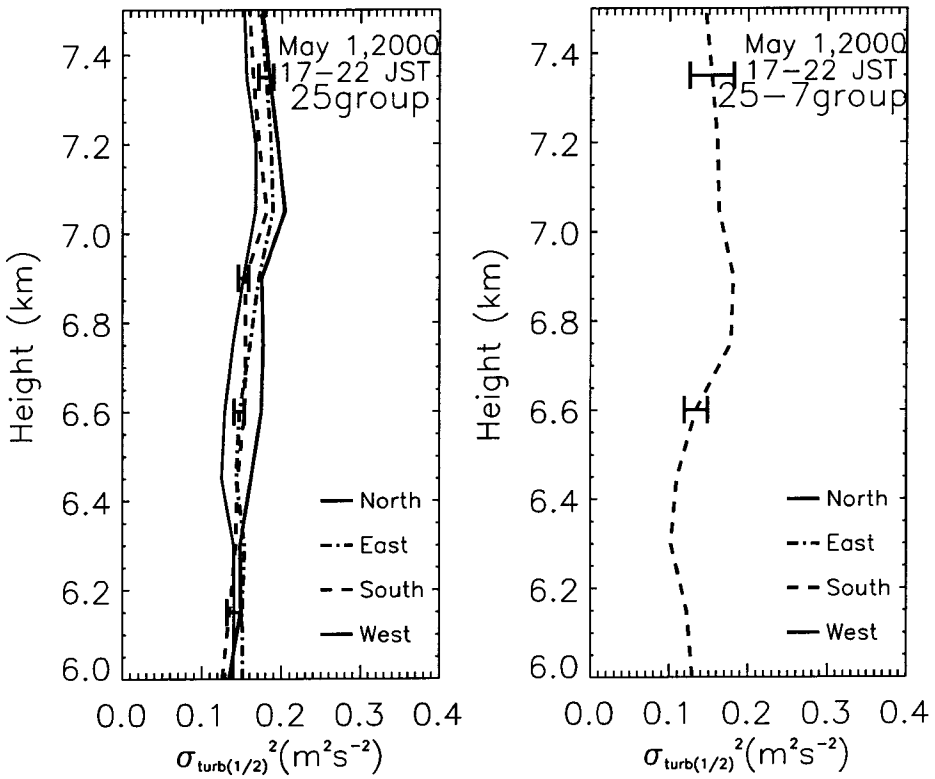

Figure 3.4: σ^2_{turb} profiles for 17–22 LT on May 1, 2000, for the 1BW method with the 25-group (left), and 2BW method with the 25- and 7-group pair (right). The profile for only the south azimuth is shown.

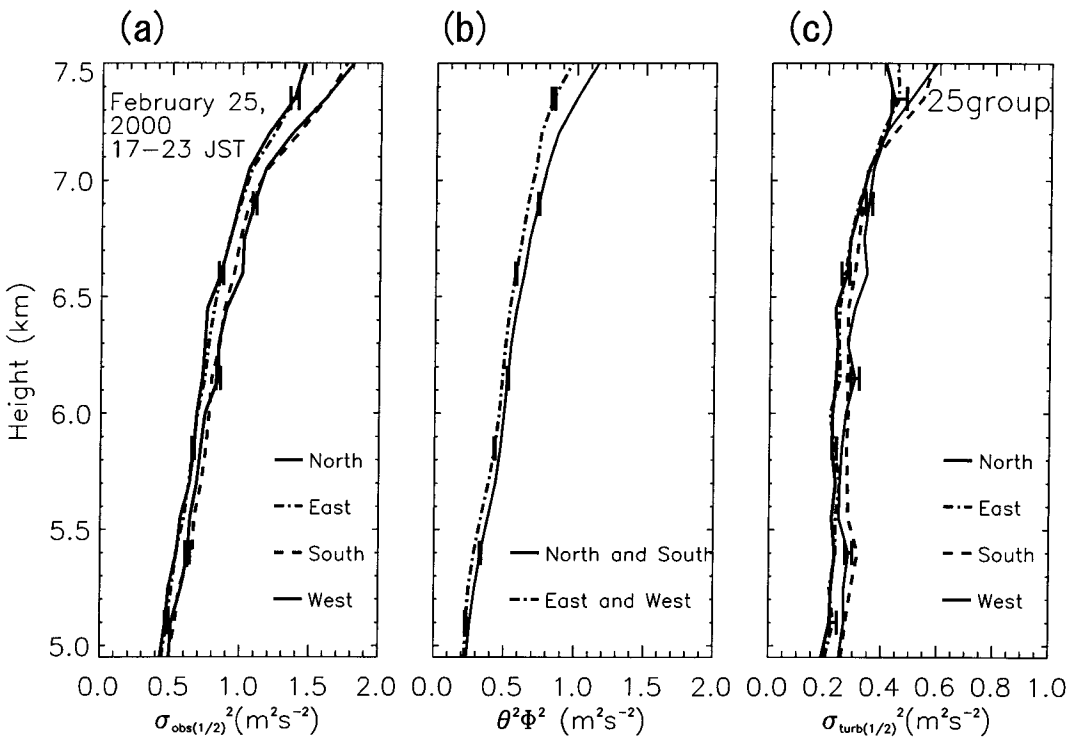

Figure 3.5: As in Figure 3.1, but for 17–23 LT on February 25, 2000.

for the beams in the cardinal azimuths. The east and west or north and south spectral widths agree very well, but the meridional widths are always larger than the zonal widths. Since the winds were strong, the values of σ^2_{corr} shown in the middle panels of Figures 3.5 and 3.6 are much larger than those seen under the lighter wind conditions shown in Figures 3.1 and 3.2. In fact, the values of σ^2_{corr} are more than half of σ^2_{obs} and thus larger than the resulting values of σ^2_{turb}. In such a case, relatively small fractional errors in estimation of $\sigma^2_{beam+shear}$ with Equation (2.34) would lead to relatively large errors in σ^2_{turb}. In fact, the 1BW values of σ^2_{turb} are about 25% larger than the 2BW values, which are not subject to such errors. For both methods the value of σ^2_{turb} increases slowly with altitude from 5 to 7 km. For the 2BW method the median values are around 0.20 m^2s^{-2}. Above 7 km all determinations of σ^2_{turb} increase rapidly with height: the reasons for this pattern are under study.

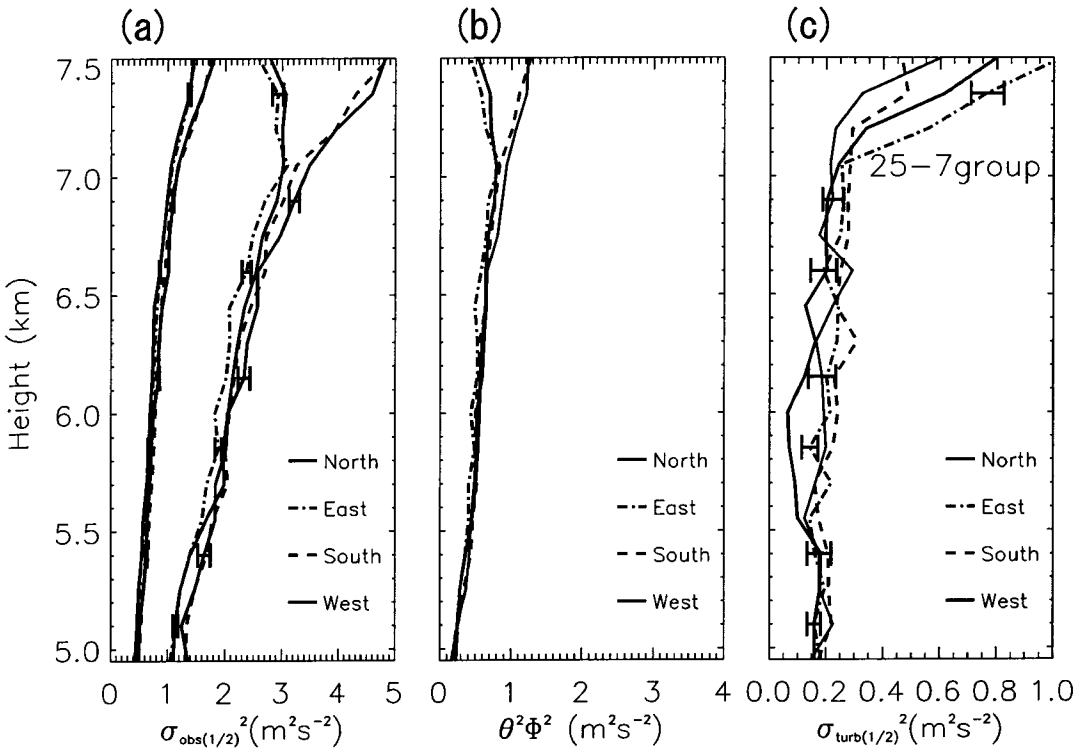

Figure 3.6: As in Figure 3.2, but for 17–23 LT on February 25, 2000.

3.4 Error Analysis

Error analysis of Equation (3.2) leads to

$$\Delta\sigma^2_{turb} = \frac{\theta_b^2\Delta\sigma^2_{obs-a} - \theta_a^2\Delta\sigma^2_{obs-b}}{\theta_b^2 - \theta_a^2} + \frac{2\theta_a^2\theta_b^2}{\theta_b^2 - \theta_a^2}\frac{\sigma^2_{corr}}{\theta^2_{a,b}}\left(\frac{\Delta\theta_b}{\theta_b} - \frac{\Delta\theta_a}{\theta_a}\right), \qquad (3.3)$$

where σ^2_{turb}, σ^2_{obs} and $\Delta\theta_r$ are the uncertainties. Clearly, using beamwidths as different as possible (i.e., maximizing $\theta_b^2 - \theta_a^2$) will help to minimize σ^2_{turb}.

The first term on the right in Equation (3.3) can be approximated by $\Delta\sigma^2_{obs} = 2\sigma_{obs}\Delta\sigma_{obs} \simeq 2.8\sigma^{3/2}_{obs}$ with the relationship $\Delta\sigma_{obs} = 1.1\sqrt{\sigma_{obs}/\tau} = 0.14\sqrt{\sigma_{obs}}$ [*Yamamoto et al.*, 1988], where $\tau = 58$ and 47 seconds for the February or August experiment. The $\Delta\sigma^2_{turb}/\sigma^2_{turb}$ due to the first term is about 100% (5%) for the February (August) experiment.

As regards the second term, Monte Carlo simulations of the MU radar antenna pattern show that for 1% element outage, the 25 (7) group $\Delta\theta_r/\theta_r \sim 0.2$ (0.5); i.e., the uncertainties caused by equipment malfunction do not scale with beam-

width and therefore will cause a contribution to σ^2_{turb}. Of course, there may be other sources of uncertainty of θ_r; for example, if the beam is not filled with homogeneous, isotropic turbulence but is only partially filled by one or more thin layers, then the effective beamwidth is not necessarily equal to θ_r.

The aspect sensitivity is another source of uncertainty of θ_r, because the effective spectral width becomes smaller than θ_r. Since the decreasing rate of θ_r generally increase with θ_r, ε with the dual-beamwidth method may become smaller than the actual value under the strong aspect sensitivity. Estimating the magnitude of such an effect will be addressed in a future study.

3.5 Concluding Remarks

A new, dual-beamwidth (2BW) spectral-width method for estimating σ^2_{turb} from the wind profiler radar observations of Doppler spectral width has been presented. The principal advantage of the 2BW method over the usual single-beamwidth (1BW) spectral width method is that it is only weakly dependent on the model for $\sigma^2_{beam+shear}$, since the principal contribution to σ^2_{corr}, is approximately proportional to θ_r^2. The non-proportional contributions to $\sigma^2_{beam+shear}$ as well as σ^2_{wave}, are negligible in cases studied here. Moreover, the 2BW method takes into account ALL beam-broadening processes that are proportional to θ_r^2, whether or not they are included in the model for σ^2_{corr}. Since the 2BW method involves fewer assumptions than other methods, determinations of σ^2_{turb} with this method can be used as a quasi-standard for estimates of σ^2_{turb} made by other methods, such as the 1BW method. For any method of measuring the turbulent kinetic energy density – whether remote-sensing or *in-situ* – a fundamental requirement is that the observations of turbulent fluctuations not be contaminated by non-turbulent processes. In the VHF band the principal contaminations are echoes from horizontally stratified refractivity fluctuations and echoes from aircraft and meteors. In the present experiment the former were obviated by pointing the antenna beams toward 10° zenith angle and the latter were largely eliminated by standard quality control procedures. The dual-beamwidth method can be used at any radar frequency, but at higher frequencies the echoes are often contaminated by scatter from particulates such as hydrometers, insects, and birds. Uncontaminated turbulent echoes can be extracted by identifying the particulate echoes using simultaneous observations by UHF- and S-band radars, as shown by *Gage et al.* [1999]. Moreover, *VanZandt et al.* [2000] demonstrated that such dual-frequency data can be used to measure ε. If the two radars have different beamwidths as well as different frequencies, then simultaneous measurements of ε and σ^2_{turb} could be used to test the theoretical relation between ε and σ^2_{turb}. Case

studies of comparisons between results found using the 1BW and 2BW methods at the MU radar indicate the following:

- During light wind conditions in August, the profiles of σ^2_{turb} from the two methods agree very well. Thus, 1BW method removing the broadening effects from wind velocity seems to have sufficiently good accuracy under weak wind condition.

- As wind speed increases, the agreement between the two methods degrades, so that, for winds larger than about 30 ms^{-1} February, the 1BW σ^2_{turb} are about 25% larger than the 2BW results. Because the 2BW makes fewer assumptions it is reasonable to attribute the observed differences to errors in the 1BW model.

- For the 2BW method, typical values of σ^2_{turb} in the altitude range from 6.0 to 7.5 km increase from about 0.07 m^2s^{-2} in August with winds of $\sim$ 2 ms^{-1} up to about 0.20 m^2s^{-2} in February with winds between about 30 and 60 ms^{-1}.

Chapter 4

Characteristics of the Turbulence Energy Dissipation Rate and the Effect of Humidity on Turbulence Echo Power

4.1 Introduction

In this chapter, we compare the turbulence energy dissipation rate (ε) obtained using the radar echo power and the Doppler spectral width methods. In the spectral width method, ε is derived from Equation (2.29) as follows:

$$\varepsilon = 0.5 N \sigma_{turb}^2. \tag{4.1}$$

However, the spectral width is affected by other factors that cause additional broadening of the spectrum. This additional broadening must be carefully removed from the observed spectral width.

On the other hand, the echo power method is based on the relationship between $\overline{\eta_{turb}}$, ε, M, and N from Equation (2.28) as follows:

$$\varepsilon = D N^3 M^{-3} \overline{\eta_{turb}}^{3/2}. \tag{4.2}$$

A detailed time-height variation of N^2 and M must be accurately estimated when this method is used, and F must also be estimated.

The values of ε provided by these two methods have been compared by several studies [*Cohn*, 1995; *Narayana Rao et al.*, 1997; *Delage et al.*, 1997; *Bertin et al.*, 1997; *Gossard et al.*, 1998]. *Cohn* [1995] derived ε for the two methods by

combining data from the Millstone Hill UHF radar and from CLASS soundings launched approximately 25 km away and found some similarity in the magnitude and shape of the two sets of ε values, which ranged from 10^{-6} to 10^{-1} m^2s^{-3}. In these earlier studies, temperature profiles from nearby radiosondes were used to derive N, under the assumption that N would not vary greatly during the balloon flight (3 to 6 hours long).

We also discuss the ε values obtained from N^2 profiles estimated through RASS observations. The MU radar–RASS campaign was carried out on August 2–6, 1995 and both radar echoes and T_v values were obtained with good time resolution. During the campaign there was a small background wind. The conventional single-beamwidth spectral width method was adapted to remove the broadening effects because the estimation error is sufficiently small under weak wind conditions as was shown in Chapter 3. In this chapter, we present characteristics of ε and the effects of humidity on η_{turb} according to the result of *Furumoto et al.* [2001].

We will begin by comparing the accuracy of N^2 values obtained from the RASS temperature profiles to the accuracy of values derived from data provided by radiosondes launched from the radar site. The ε values obtained by the two radar methods are evaluated using the N^2 obtained by RASS. The main factor that determines the echo-power intensity is also considered.

4.2 MU Radar–RASS Campaign during August 2–6, 1995

The MU radar–RASS campaign was carried out during August 2–6, 1995. The observation parameters are summarized in Table 4.1. Three components of wind velocity and temperature were acquired every 3.6 minutes for nearly four days, from 3:00 LT on August 2, 1995, to 00:00 LT on August 6, 1995. Both wind and RASS echoes were observed in three height ranges: 1.20–10.65 km, 4.80–14.25 km, and 10.80–20.25 km. The acoustic frequency range was adjusted taking into consideration the changes in atmospheric temperature to satisfy the Bragg condition in each height region. The IPP, sub-pulse length, and pulse compression code were appropriately modified as shown in Table 4.1. Five radar beam directions were used for RASS observation, (azimuth angle, zenith angle) = (315°, 10°), (330°, 10°), (300°, 14°), (315°, 14°) and (330°, 14°), which were found to be suitable based on a ray-tracing of acoustic wave-fronts.A cycle of two wind and three RASS observations were repeated, and the total duration for a single cycle of measurements was 3.6 minutes.

Table 4.1: Observation parameters of the MU radar–RASS measurement for August 2–6, 1995.

MU radar			
height range (km)	1.20–10.65	4.80–14.25	10.80–20.25
IPP (μs)	412	404	416
sub-pulse length (μs)	2	2	2
number of beams	5	5	5
number of receiver channels	2	2	2
coherent integration	30	28	24
time series	128	128	128
incoherent integration	5	5	5

acoustic source		
transmitter	loudspeaker	pneumatic transducer
waveform	CW	pulse
pulse length (s)	—	0.4 (1.20–10.65 km)
		0.4 (4.80–14.25 km)
		0.5 (10.80–20.25 km)
pulse interval (s)	—	10
repetition period (s)	3.0	—
chirped frequency (Hz)	85–115	85–115 (1.20–10.65 km)
		93–103 (4.80–14.25 km)
		87–97 (10.80–20.25 km)
number of pulses	—	4

For investigating the characteristics of turbulence, the turbulence echo received by the radial wind velocity channel of the RASS mode pointed to (300°, 14°) was used because the wind observation with a beam pointed at a zenith angle of 8° is insufficient for removing the influences of specular echoes.

During this campaign, a total of 17 radiosondes were launched every 6 hours at 3:00, 9:00, 15:00 and 21:00 LT and obtained profiles of virtual temperature, pressure and humidity. Radiosonde data was sampled every 2 seconds, and the original height resolution is about 10 m. The radiosonde data were averaged for the altitude of 150 m in order to make them compatible with the radar data.

4.3 Background Meteorological Conditions

We here describe the basic meteorological conditions during the MU radar–RASS observation. The mean profile of eastward (u), northward (v) and vertical (w) wind velocities measured with the MU radar are shown in Figure 4.1. The amplitudes for vertical wind are magnified by a factor of 10 for clarity. Both u and v were fairly small, since the jet stream was very weak. Below about 10 km, v was as small as -4–0 ms^{-1} and u was generally stronger than v, so the wind direction was nearly eastward. However, it became southward at about 15 km. Throughout the entire height range, w was fairly small. These results indicate calm meteorological conditions.

From the temperature gradient of the RASS profiles, N^2 was derived. The accuracy of N^2 by the MU radar–RASS was examined. Since RASS provides the virtual temperature, which includes the effects of moisture, Atmospheric virtual temperature was calculated by using the humidity data from radiosondes.

The left panel of Figure 4.2 shows a typical profile of N^2 with the MU radar–RASS (N^2_{RASS}) and radiosondes (N^2_{sonde}). It normally takes about two hours for a balloon to reach 22 km, the maximum height range of the RASS observation. Accordingly, N^2_{RASS} was averaged for two hours in this comparison. The error bar indicates the standard deviation of N^2_{RASS}, representing temporal variations of N^2. Most of N^2_{sonde} is within the error bar. These deviations seemed to be caused by natural variability, though in the lower altitudes some exceeded the standard deviation of N^2_{RASS}. Below 8 km the fluctuation in N^2 existed with a dominant vertical scale of about 2 km, and an amplitude of 1.0×10^{-4} s^{-2}. The distinct peaks of N^2 can be seen at 4 km and 7.5 km Between 8–13 km the values gradually decreased, but they increased sharply above 13 km near the tropopause.

The right panel of Figure 4.2 indicates a profile of the normalized discrepancy

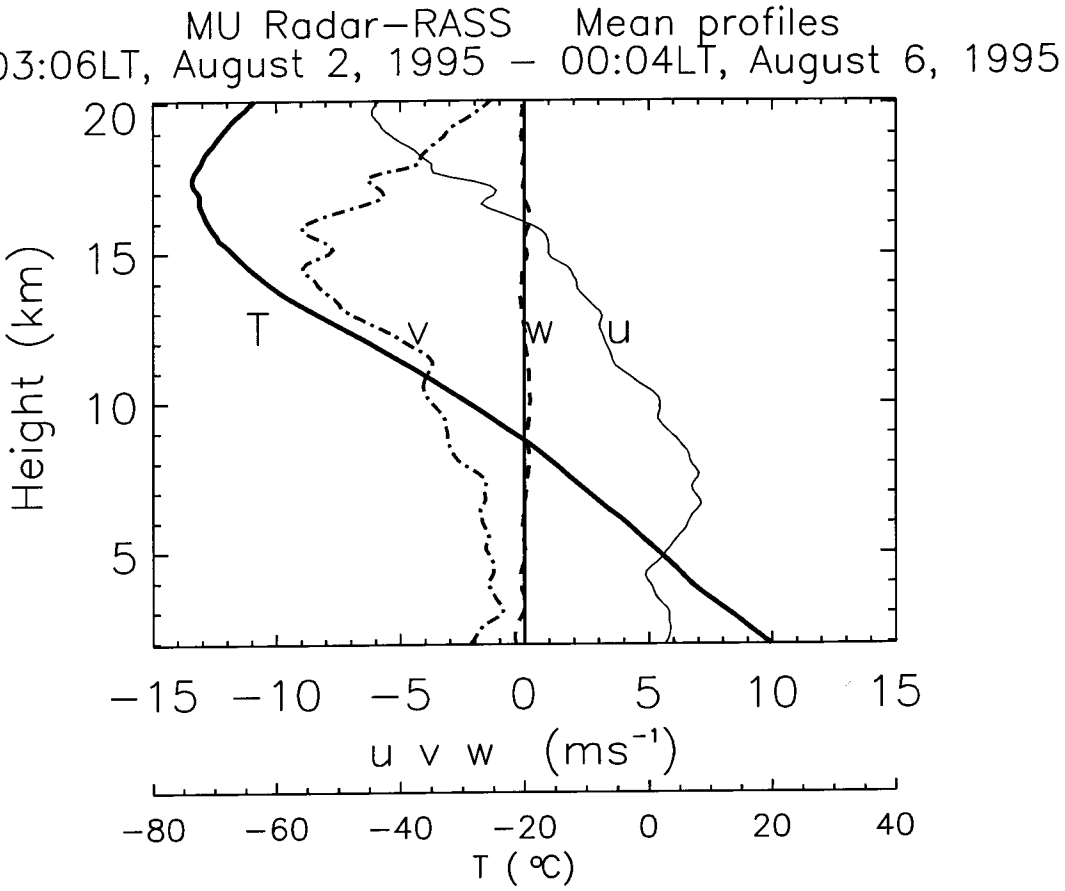

Figure 4.1: Mean profiles of zonal wind velocity u (solid), meridional wind velocity v (long-dashed), vertical wind velocity w (short-dashed), and temperature T_v (thick solid) observed with the MU radar–RASS on August 2–6, 1995. The vertical wind velocity is magnified by 10 times.

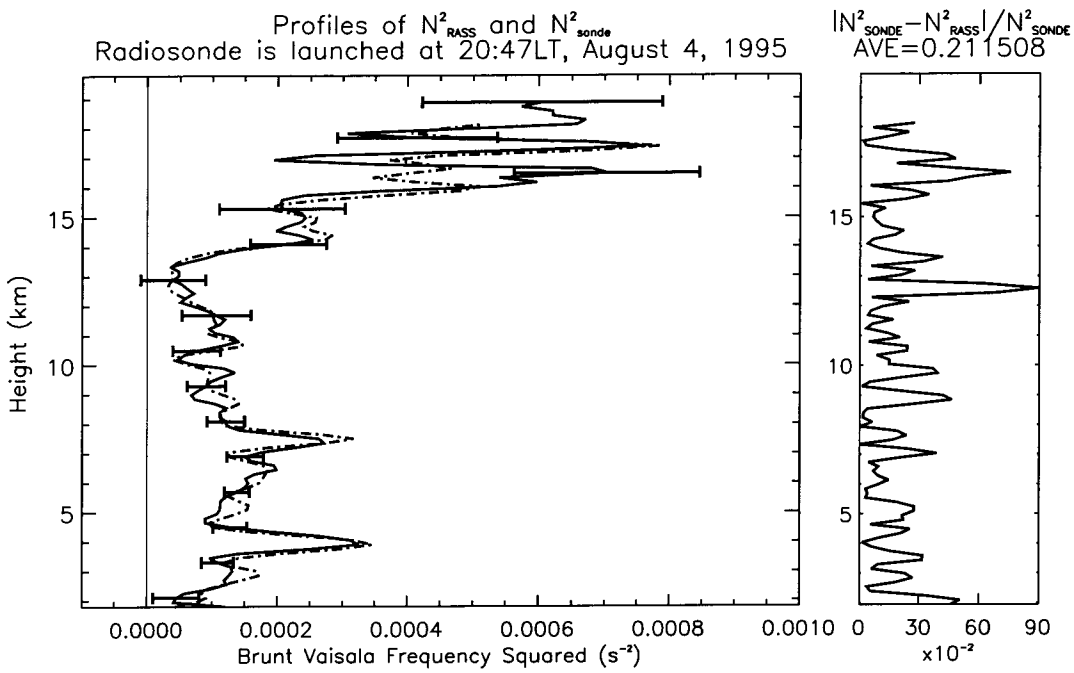

Figure 4.2: Profiles of N^2 with radiosondes launched at 20:47 LT on August 4, 1995 (solid), and N^2 by RASS averaged for 2 hours (short-dashed). Right panel shows a profile of the normalized discrepancy. The averaged value throughout the observation height is 0.21.

defined as

$$\frac{\Delta N^2}{N^2_{sonde}} = \frac{|N^2_{RASS} - N^2_{sonde}|}{N^2_{sonde}}. \tag{4.3}$$

Fluctuations in the normalized discrepancy were large around 13 km corresponding to the small N^2. Further, $\Delta N^2/N^2_{sonde}$ averaged in the four height ranges (1.7–5.8 km, 5.9–10.0 km, 10.1–14.2 km and 14.3–18.4 km) was calculated from the data of 12 radiosondes as shown in Table 4.2. The mean $\Delta N^2/N^2_{sonde}$ is about 0.2, except between 10.1–14.2 km, where a large discrepancy exists that may be caused by the small N^2 values there.

4.4 Profile of ε with Echo Power and Spectral Width Methods

In this section, we evaluated ε from both the spectral width and the echo intensity and compared the characteristics of ε by focusing on the agreement.

Table 4.2: Averaged $\Delta N^2/N^2_{sonde}$ for 12 radiosondes in four height ranges.

Height Range[km]	$\Delta N^2/N^2_{sonde}$
1.7 – 5.8	0.19
5.9 – 10.0	0.21
10.1 – 14.2	0.38
14.3 – 18.4	0.21

the spectrum parameters: echo power, Doppler velocity and spectral width were determined by applying a least squared Gaussian fitting method to the observed spectrum in this analysis. However, the accuracy of the Gaussian fitting is firstly confirmed compared with an alternate estimation of directly calculating the spectral moments.

Figure 4.3 shows a single profile of S/N and spectral width obtained by the Gaussian and moment methods at 10:12 LT on August 4, 1995. The spectrum parameter was averaged for 30 minutes to smooth out small-scale variations. Below 7 km, fluctuations in S/N in the Gaussian method show a dominant vertical scale of about 1 km, where S/N ranged 5–25 dB and distinct peaks were seen at 5.7 km, 6.3 km and 7.6 km. Between 7–9 km S/N suddenly decreased, and above 9 km it gradually decreased. S/N profiles were consistent for the two methods, except for the fact that the peak values at 5.7 km, 6.3 km and 7.6 km had slightly smaller values for the Gaussian fitting.

The aspect sensitivity of clear air echoes were also confirmed. The ratio of echo powers pointed at a zenith angle of 14° to that of the vertical beam was calculated. The averaged ratio value along the altitude becomes more than -13 dB. Consequently we assumed that the influence of the specular reflection in the clear air echoes at the zenith angle of 14° is sufficiently attenuated enough to be neglected.

The spectral width estimated by the Gaussian method was large below 5 km and above 13 km, and ranged between 0.6 and 2.0 ms^{-1} except for a notable peak of 2.1 ms^{-1} at 5.3 km. The estimated spectral width was larger by the moment method by about 0.2 ms^{-1}, although the height structure displayed good agreement. Although the results from both methods showed slight differences, a good correlation was seen.

It is noteworthy that the spectral width became small at the altitudes with large S/N in Figures 4.3. This anti-phase relation between the spectral width and S/N is puzzling, since a positive correlation would be expected considering

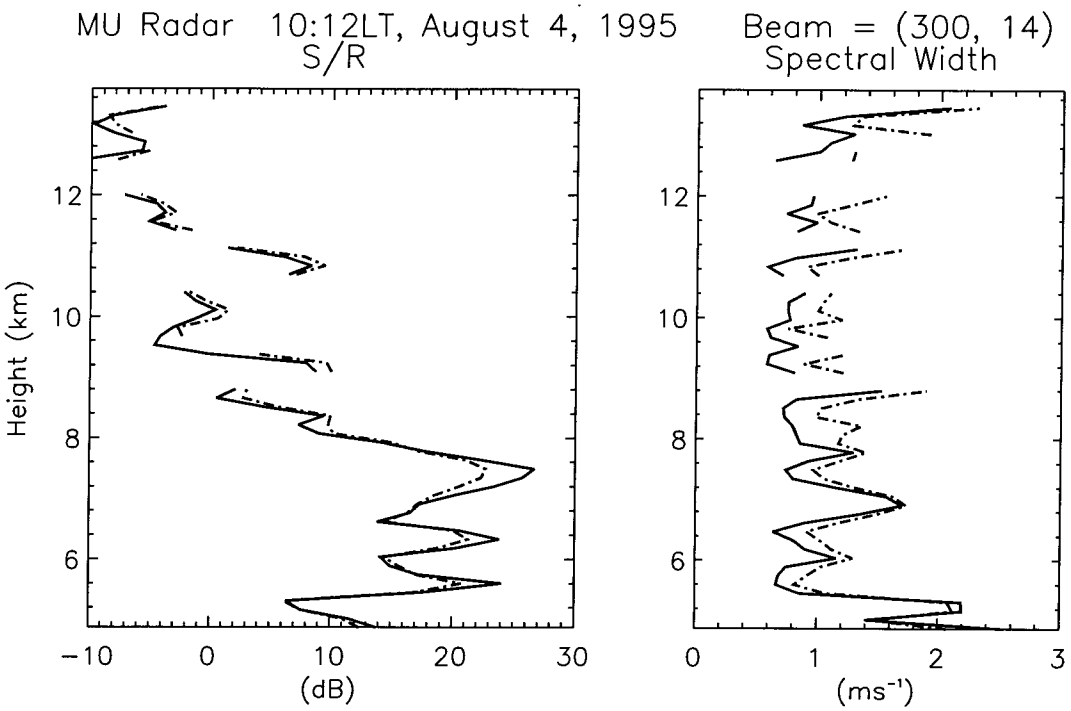

Figure 4.3: Profiles of S/N(left) and spectral width (right) at 10:12 LT on August 4, estimated by Gaussian and the moment methods shown by the solid and short-dashed lines, respectively.

Equations (4.1) and (4.2) on ε. That is, if ε, representing the turbulence intensity, is the dominant factor in these relations, a positive correlation between the spectral width and S/N could be expected. The analyzed results suggest that other factors, e.g., the relative magnitude of M^2/N^2 and N, determine the structure of the profiles.

4.4.1 Profile of ε from Spectral Width

Now ε from the spectral width is derived. Firstly, relative magnitudes of the broadening effects is discussed in comparison to the observed spectral width. σ_{obs} can be expressed as a convolution of each spectral width. Provided that the spectra due to both turbulence and the broadening effects can be approximated by a Gaussian distribution, the spectral width by the turbulence, σ_{turb} is expressed as Equation (2.30). Because the horizontal wind velocity was small throughout the campaign, the convensional single-beamwidth method was adapted to estimate the broadening effects, whose error is small under weak wind condition.

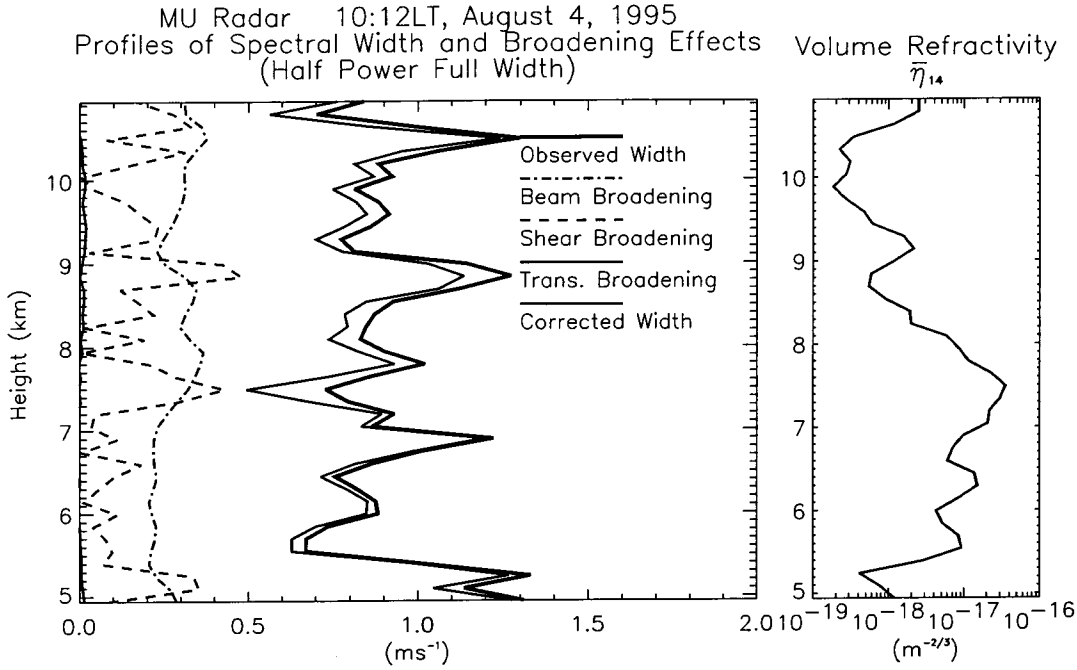

Figure 4.4: Profiles of actual observed spectral width (solid), beam broadening (short-dashed), shear broadening (long-dashed), wave broadening (dash dot) and the corrected spectral width after removing the three broadening effects (dash dot dot dot). Right panel shows a profile of $\overline{\eta_{14}}$. Profiles are obtained by single observation at 10:12 LT on August 4, 1995. Throughout a given altitude, the broadening structures of the three profiles are fairly small compared with observed spectral width.

Figures 4.4 and 4.5 show instantaneous profiles at 10:12 LT on August 4, 1995 and 21:58 LT August 3, 1995, respectively. In Figure 4.4 the observed spectral width fluctuates widely from 0.7 to 1.3 ms^{-1}. The beam broadening has an almost constant value of about 0.3 ms^{-1}. Although the shear broadening was sometimes enhanced, its maximum was limited to 0.5 ms^{-1}. Throughout the altitude range, the shear broadening was much smaller than the observed spectral width. As a result, the corrected spectral width ranged between 0.6–1.3 ms^{-1} and displayed roughly the same structure as the observed spectrum. Note that the volume reflectivity at the zenith angle of 14° ($\overline{\eta_{14}}$) becomes large between 7–8 km, where the observed spectrum becomes narrow, showing the anti-correlation between σ_{turb} and $\overline{\eta_{14}}$.

In Figure 4.5 the observed spectral width is as small as 0.7 ms^{-1} between 7–8 km. The beam broadening effect was not so variable, but the shear broadening

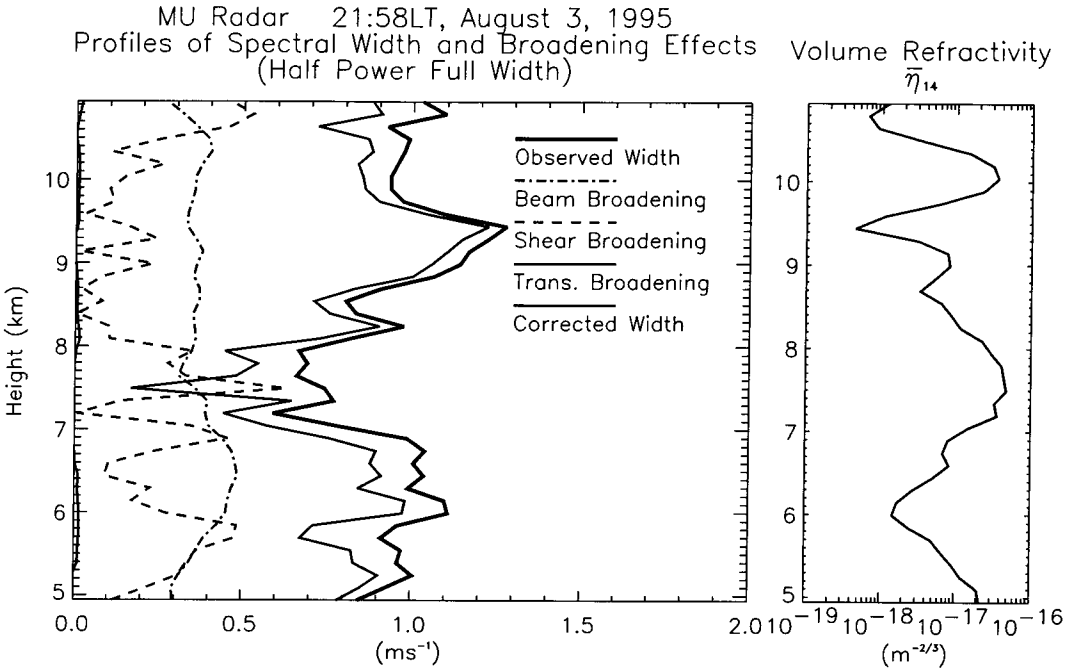

Figure 4.5: The same as Figure 4.4 except profile were obtained by single observation at 21:58 LT on August 3, 1995. We can see that shear broadening becomes large and corrected spectral width becomes very small at 7.5 km.

became large at 6.9 and 7.5 km, causing the corrected spectral width to be very small at 7.5 km. This is one of the worst cases of the corrected spectrum width becoming smaller than the observed one. Fortunately, most of other data did not involve such significant corrections. We note again the anti-correlation between the observed spectral width and $\overline{\eta_{14}}$.

Next, the discrepancy of ε from the spectral width estimated by the Gaussian fitting and moment methods is discussed. Although ε estimated from the spectral width by the Gaussian method is less than 1.4 times that by the moment method, a good correlation between the variation of ε estimated from the spectral width by both methods be seen.

Using N^2 from RASS measurements, ε from the corrected spectral width was derived . Figure 4.6 shows mean profiles of ε averaged for one day and for three days with the spectral width method. ε fluctuates between 4.0×10^{-4} and 1.4×10^{-3} m^2s^{-3}. The profiles of ε do not greatly fluctuate, but are nearly constant along the same altitude.

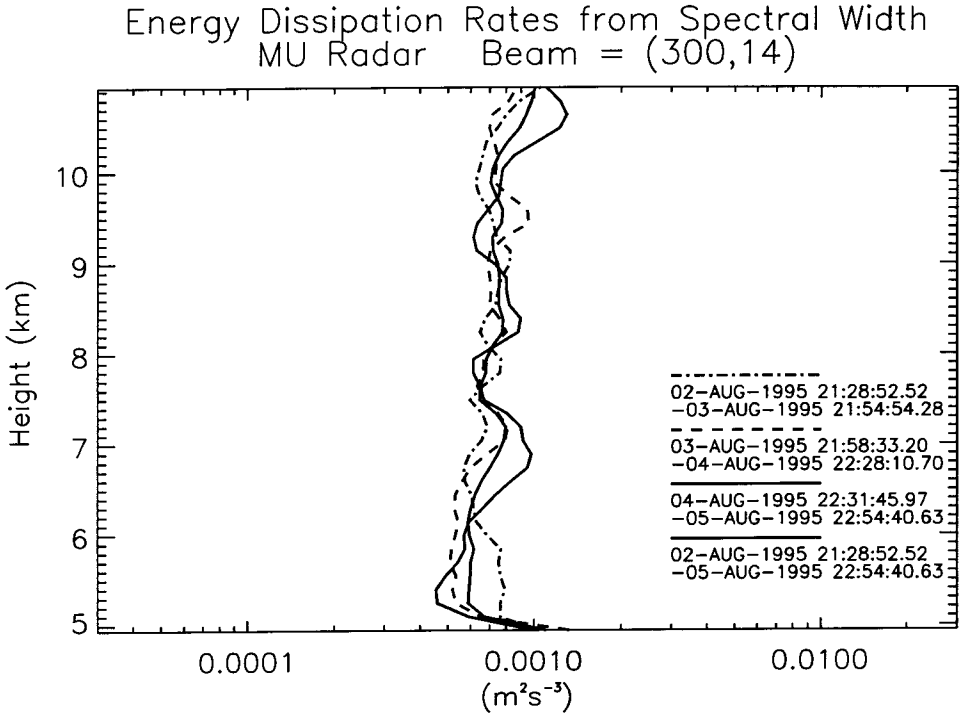

Figure 4.6: Profiles of ε from spectral width averaged for an entire day and that averaged for 3 days. The radar beam direction is (azimuth angle, zenith angle) = (300°, 14°).

4.4.2 Profile of ε from Echo Power

Next, ε from the echo power method was derived as shown in Equation (4.2) by using N^2 derived from RASS temperature profiles, $\overline{\eta_{turb}}$ from echo power at the zenith angle of 14° and M from the RASS temperature and humidity profiles taken by radiosonde. Because of the lack of a calibration system for the amplitude of echo power and the precise value of the noise level, accurate equivalent noise temperature (T_c) and the loss factor of the receiver (L) values could not be estimated, so we used a typical value from a map of cosmic noise for the MU radar [*Maeda and Maeda*, 1991]. The parameters to derive the absolute echo power intensity is shown in Table 4.3.

As described in section 2.1.3, turbulence in the free atmosphere is not stationary with time and nonhomogeneous in space, and the turbulence tends to have a layered structure. Therefore, turbulence does not exist within the whole radar sample volume. Although it is difficult to derive an accurate estimate of a volume filling factor, F, the simplest estimation of F can be obtained by assuming

Table 4.3: Local Parameters.

Parameter	Value
Equivalent Noise Temperature (T_c)	5000K
Loss Factor (L)	0.9
Efficiency of Radar Antenna	1

a single turbulent layer in the radar sampling volume, where the latter is inferred by a two-dimensional Gaussian model of zenith angle and range. Then, F was calcurated for various cases while changing the location of the turbulence layer within the range and found that the average value of F is about 0.12.

For deriving M in Equation (2.22), we use RASS temperature profiles and humidity profiles from radiosondes launched every 6 hours, where the latter is appropriately interpolated. A mean profile of ε from echo intensity is shown in Figure 4.7. ε averaged for three days greatly fluctuates from 6.0×10^{-5} to 2.0×10^{-3} m^2s^{-3}. The averaged ε increased with height below 7 km, became constant, and then decreased above 9 km. Daily mean profile fluctuations were larger than the 3-day mean. The detailed structure of each of the three daily profiles does not show a definite correlation between them.

4.4.3 Comparison of ε from Both Methods

Levels of ε from both methods are roughly on the same order, which seems to reflect the property of the factors F and L, which we used in the deriveration of ε from the echo power. However, their characteristics are much different. It is found that the ε from the echo power significantly fluctuated, while that from the spectral width did not. The daily mean profiles of ε by the echo power method had much larger fluctuation. Moreover, large fluctuations were observed between daily profiles. However, daily averaged profiles of ε from the spectral width had no large changes, and their daily fluctuations were not so large.

The ε from both methods did not agree. Since the background wind during this campaign was ideal for the estimation of ε, the spectral width method seems to be more reliable than the echo power method. We now discuss the reason for the large fluctuations of ε with the echo power method.

We specified the main factor of echo power for investigating the correlations among $\overline{\eta_{14}}$, N^2, and M^2, which are related by Equation (4.2). Temperature profiles with RASS and humidity profiles with radiosondes is necessary to derive M. Therefore, the radar data was selected at the corresponding time and height to the ascending radiosonde and calculated $\overline{\eta_{14}}$, N^{-2}, and M^2. Figure 4.8 shows

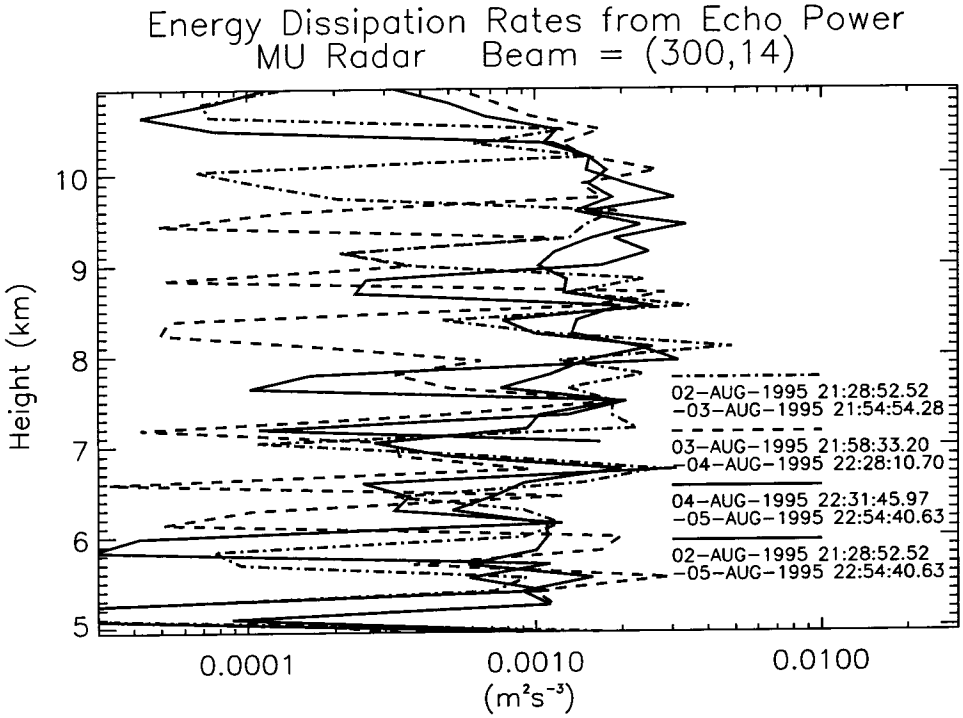

Figure 4.7: The same as Figure 4.6 except ε is from echo intensity.

profiles of $\overline{\eta_{14}}$, N^{-2}, and M^2. There are fluctuations in $\overline{\eta_{14}}$ with a vertical wavelength of about 0.5 km. The outline of $\overline{\eta_{14}}$ maximes at 7 km, and between 8–9 km $\overline{\eta_{14}}$ decreases rapidly to as small as one tenth of the maximum value. Above 9 km, there are the large fluctuation of $\overline{\eta_{14}}$ ranging between 1.0×10^{-19}–6.0×10^{-17} $m^{-2/3}$. While N^{-2} fluctuates with altitude, but the amplitudes of the fluctuations are small, and the maximum value of N^{-2} is less than thirty times the minimum value. Above 8 km, a rapid decrease is not recognized, as in the profile of $\overline{\eta_{14}}$.

We can see a very sharp decrease of M^2 at 5.5 km, 6.8 km and 7.9 km. However, the general outline of the profile decreases with altitude. A sharp decrease can also be found above 8 km. Although the minimum value of N^{-2} and the peak of M^2 is seen at the same altitude of 7.4 km, any such strong correlation between the variations of them cannot seen. This result suggests that M^2 is not primarily influenced by N^2 but probably by variations in humidity. M^2 has sharp decreases at 5.5 km and 10.0 km, which could be caused by the horizontal difference between radar and radiosonde observations.

The profile of M^2 with $\overline{\eta_{14}}$ was further compared. M^2 ranges between 10^{-15} and 10^{-18} m^{-2}, except for the sharp decrease of M^2. This fluctuation is signifi-

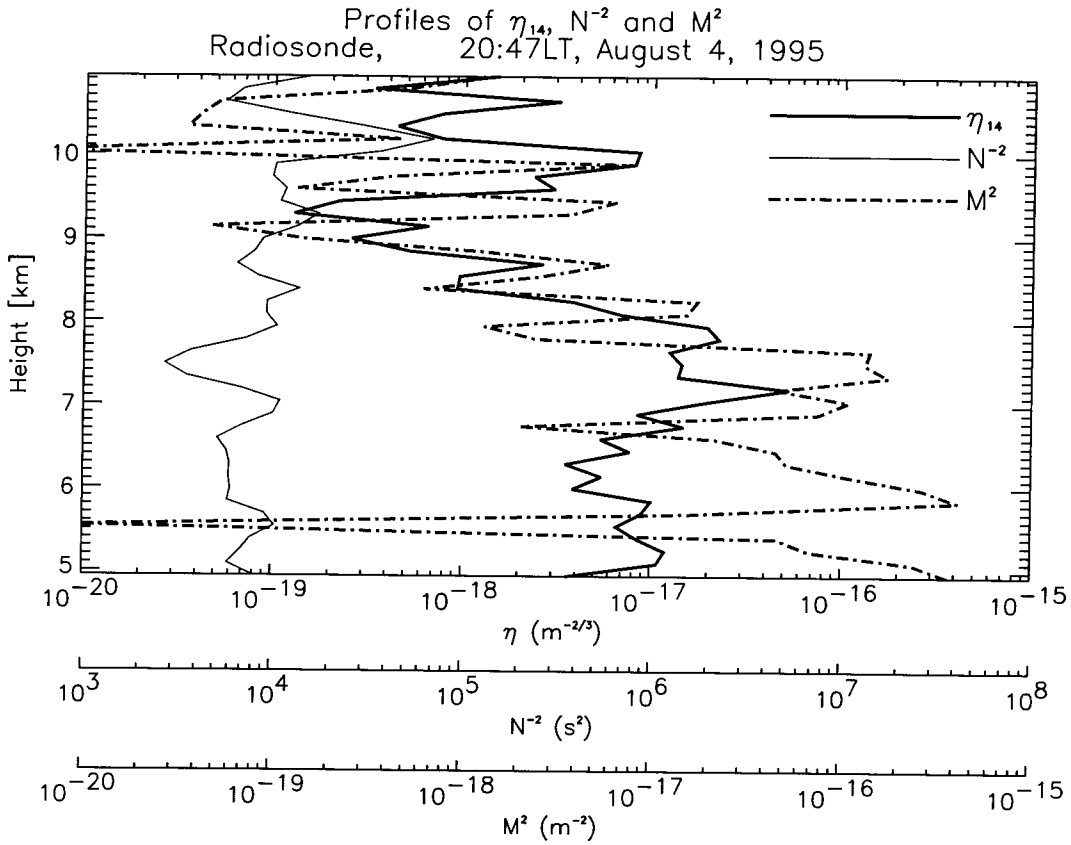

Figure 4.8: Profiles of $\overline{\eta_{14}}$ (thick solid), N^{-2} (solid), and M^2 (dash dot) launched at 20:47 LT on August 4, 1995.

cantly larger than that of N^2 but is on the same order as that of $\overline{\eta_{14}}$. Therefore, M^2 has more influence on the determination of $\overline{\eta_{14}}$ than N^2.

We further estimated the effects of the dry air and humidity for $|M|$ with radiosondes positioned side-by-side. M is shown as Equation (2.22), and the first term of Equation (2.22) indicates the dry air term, while the second and third terms show the influences of q and $\mathrm{d}q/\mathrm{d}z$, respectively. Figure 4.9 shows the ratio of the absolute magnitude of each term to $|M|$ from a typical summer and winter sounding at 21:08 LT on August 2, 1995 and at 2:47 LT on November 1, 1997, respectively. Note that the magnitude of M ($|M|$) generally decreases exponentially with height at high altitude, because it is proportional to p/T, i.e., atmospheric density.

The left panel of Figure 4.9 indicates that in a moist atmosphere below about 6 km and 3.5 km in summer and winter, the third term (**c** in Figure 4.9), depending on $\mathrm{d}q/\mathrm{d}z$, is the largest, giving 70–90% of $|M|$. As a result, M is mostly negative in these height ranges, because q generally decreases with altitude except near the bottom of a cloud. The first (dry) term (**a** in Figure 4.9) becomes dominant in a layer with small q, which can be recognized more evidently in the winter case. The contribution by the second term due to q (**b** in Figure 4.9) is usually less than 10%, although it is sometimes significant in the planetary boundary layer. To summarize, the height structure of M is mainly determined by $\mathrm{d}q/\mathrm{d}z$ in a moist layer, therefore, the profile of M is expected to correlate highly with that of $\mathrm{d}q/\mathrm{d}z$.

To derive M in this analysis, we used the moisture profiles measured by radiosondes launched every 6 hours and interpolated the variation of humidity within the interval between launches. In the actual atmosphere, the spatial and temporal distributions of humidity are complicated and fluctuate significantly. Radiosonde observations cannot detect rapid variations in humidity when the humidity distribution fluctuates drastically within a period shorter than a few hours.

In this case study, the result strongly suggests that $\overline{\eta_{14}}$ mainly depends on the structure of M, which is mainly determined by the humidity gradient. Accordingly, the detailed information of the humidity structure is essential for determining ε from the turbulence echo power. As a result, we can conclude that the echo intensity is mainly affected by the humidity gradient, not by ε in the wet season.

Finally, we considered the effects of humidity on the anti-correlation between the spectral width and $\overline{\eta_{14}}$ in Figures 4.4 and 4.5. From Figures 4.2, 4.4 and 4.5, we can observe that both N^2 and $\overline{\eta_{14}}$ tend to be enhanced between 7–8 km, while σ_{obs} shows the opposite structure, that is, it is depressed between 7–8 km. M largely depends on $-\mathrm{d}q/\mathrm{d}z$ in a moist atmosphere. We also found

(i)

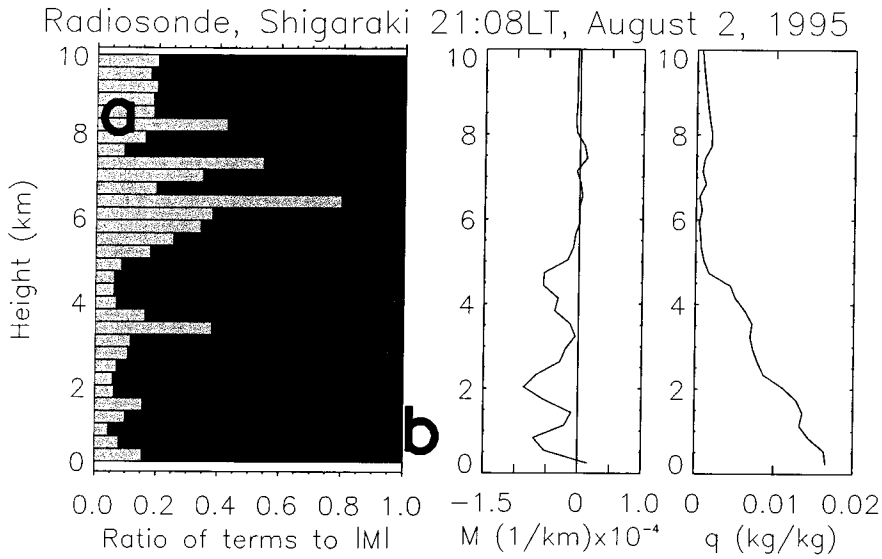

(ii)

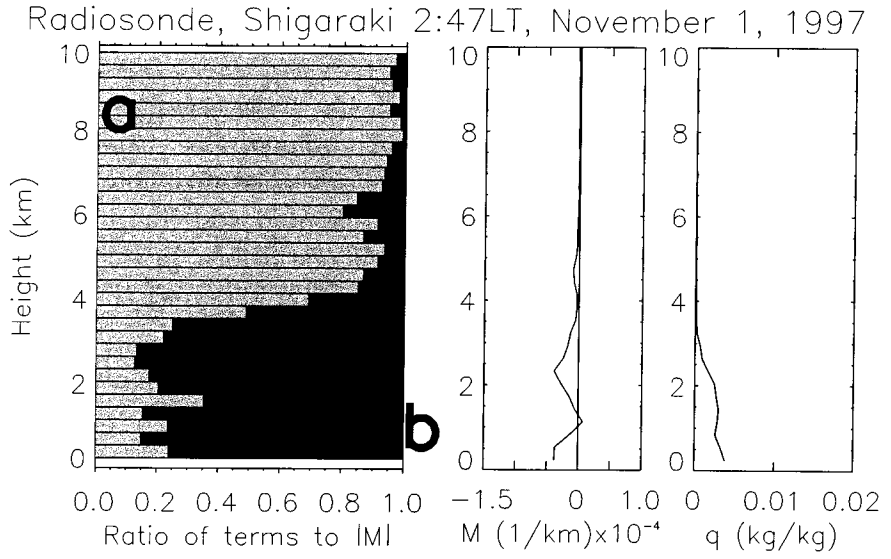

Figure 4.9: Profiles of M (center) and q (right) observed from a radiosonde launched at (i) 21:08 LT on August 2, 1995 and (ii) 2:47 LT on November 1, 1997. Left panel shows the relative magnitude of the three terms in M (see text).

empirically that $-\mathrm{d}q/\mathrm{d}z$ correlates well with N^2. The physical meaning is not fully understood, but it seems to be related to the energy exchange between latent heat and sensible heat. As such, M becomes approximately proportional to N^2. Now Equation (4.2) is rewritten as

$$\overline{\eta_{turb}} \propto \varepsilon^{2/3} N^2. \tag{4.4}$$

If ε is constant along altitude, as analyzed in Figure 4.6, σ_{turb} becomes smaller when N^2 increases (Equation (4.1)). On the other hand, Equation (4.4) suggests an increase in $\overline{\eta_{turb}}$. Thus, the anti-correlation between the σ_{turb} and $\overline{\eta_{14}}$ profiles in Figures 4.4 and 4.5 could be explained by the effects of N^2 on these parameters, giving opposite contributions to their magnitudes.

For a deeper study into the matter, we should investigate the case when the influence of humidity becomes small in the winter season and determine the dominant factor that determines turbulence echo power.

4.5 Temporal Variation of Energy Dissipation Rate

We studied the time variation of ε from both methods and the parameters used for the derivation of ε to investigate the main factor determining ε. In this analysis, the values was averaged for about 11 minutes and 450 m to clarify the variation and to exclude rapid variations from the detailed structure.

Figure 4.10 shows the time variations of σ^2_{turb}, N, and ε estimated by spectral width for about 18 hours at about 9 km. The time variation of N had smaller fluctuations than σ^2_{turb}. ε derived from σ^2_{turb} and N fluctuated with a dominant period of about 20 minutes, and the peaks coincided well with that of σ^2_{turb}. On the other hand, from a comparison between ε and N, any significant correlation could be found. Therefore the temporal variation of ε with the spectral width method is mainly determined by that of σ^2_{turb} in this case study.

In calm conditions, the conventional derivation supposing a constant N is a good approximation for the estimation of ε from spectral width. We investigated the accuracy of the conventional derivation, comparing the two ε values using a constant N and N with RASS observation. We calculated the percentage difference between them and averaged it for 18 hours. The difference averaged over 18 hours is 16%. These results were obtained in calm meteorological conditions such as the summer time in Japan. However, in a disturbed condition, the variation of N is often large, causing the influence of N to become large in such condition.

Next, we investigate the temporal variations of ε from echo power and the parameters used for the derivation. From Equation (4.2) ε is proportional to

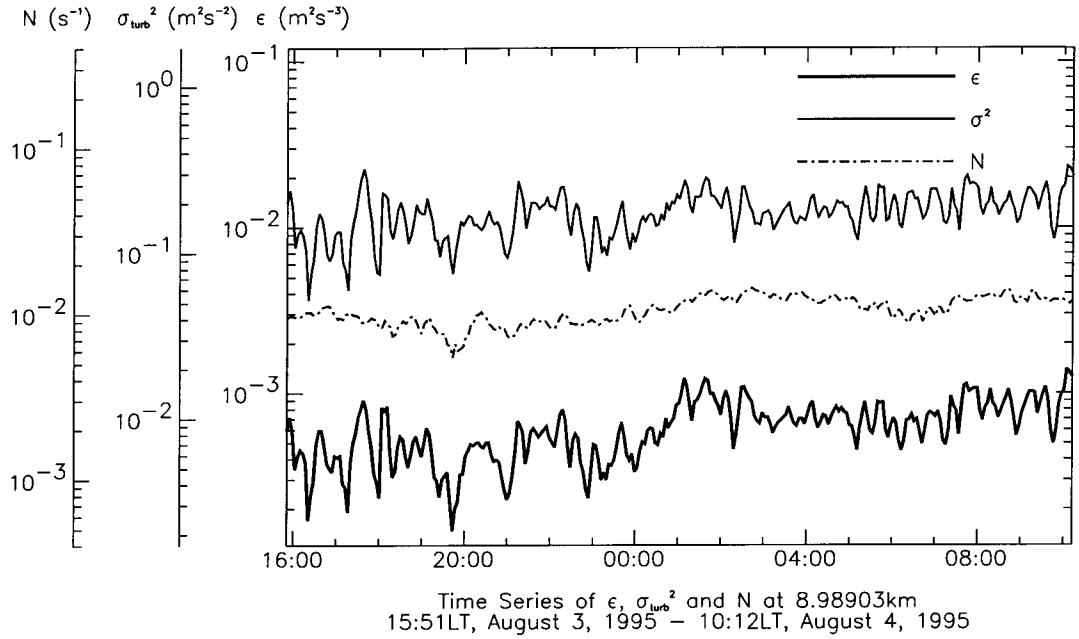

Figure 4.10: Profiles of ε with the spectral with (thick solid), σ^2_{turb} (solid), and N (short-dashed) between 16:00 LT on August 3 and 10:00 LT on August 4. The vertical axis is scaled logarithmically and its extent is 10^3.

$\overline{\eta_{turb}}^{3/2}$, N^3, and M^{-3}. Figure 4.11 shows the temporal variation of ε with the echo intensity method, $\overline{\eta_{14}}^{3/2}$, and N^3. The vertical extent of Figure 4.11 is 10^7, which is broader than that of Figure 4.10. Figure 4.11 shows a good correlation between the small-scale fluctuations of ε from echo power and $\overline{\eta_{14}}^{3/2}$. M^{-3} is anti-correlated with the long period variations in $\overline{\eta_{14}}^{3/2}$. So the large-scale trends of ε are cancelled out by those of M^{-3}, which have a negative correlation to $\overline{\eta_{14}}^{3/2}$.

A small-scale fluctuation in M^{-3} cannot be seen. For the derivation of M we used the humidity information interpolated from radiosonde data launched every 6 hours. Considering that humidity is the main factor determining M below the middle troposphere, and humidity seems to greatly fluctuate in the short period in the wet season, the lack of small-scale fluctuation of M^{-3} is caused by the lack of detailed humidity information.

We compared ε values obtained from both methods. The range of ε from echo intensity is wider than that of ε from spectral width. Moreover, the fluctuations were quite different, and there was no significant correlation between them. This result agrees with that of the comparison of the profiles in the previous section. In this analysis, we assumed that ε from spectral width, which can be derived

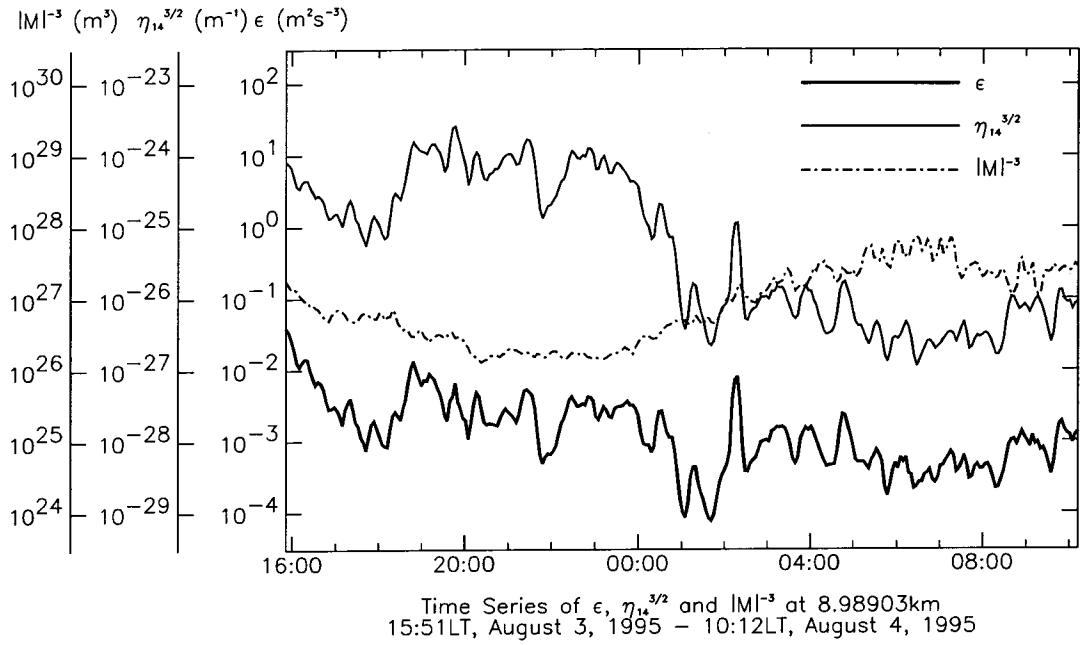

Figure 4.11: The same as Figure 4.10 except profiles of ε are with the echo power (thick solid), $\overline{\eta_{14}}^{3/2}$ (solid), and M^{-3} (short-dashed). The extent of the vertical scale is 10^7.

by only radar data, is correct. However, ε from echo intensity has much larger fluctuations than ε from spectral width. In Figure 4.11 the large fluctuations of ε from echo power are mainly influenced by $\overline{\eta_{14}}^{3/2}$. Because of the lack of detailed humidity information, which is the main factor of M, we cannot represent the detailed variation in M. The temporal variation of $\overline{\eta_{14}}^{3/2}$ is ideally cancelled out by the variation of M^{-3}, which is as large as that of $\overline{\eta_{14}}^{3/2}$, and the variation of ε from echo power should become as small as that for ε estimated with spectral width. However, the small-scale fluctuations of $\overline{\eta_{14}}^{3/2}$ are not actually cancelled out by M^3 because of the lack of temporal resolution in the humidity, although both of the large-scale trends are cancelled.

4.6 Concluding Remarks

We evaluated ε obtained from two methods, using the high-resolution N^2 with RASS. The MU radar–RASS campaign was carried out during August 2–6, 1995. We acquired three components of wind velocity and temperature every 3.6 minutes for almost four days from 3:00 LT on August 2, 1995, to 00:00 LT on

August 6, 1995.

During the campaign, u, v, and w were fairly small throughout the entire height range. This result indicates that the basic meteorological condition during the campaign was calm. We ascertained the accuracy of N^2 by the MU radar–RASS and compared it with the radiosonde result. Most of the error in N^2 between them was within the natural variations of N^2. The normalized discrepancy was about 0.2 except between 10.1–14.2 km.

Next, the accuracy of the Gaussian fitting method was examined by comparison with another estimation using the moment method. A good correlation between the height structures of both methods was observed, although there are slight differences between the results of the two methods.

The adequate zenith angle for extracting only the turbulence scattering was also discussed. Because the beam of the wind observation steered at the zenith angle of 8° is insufficient for removing the influences of specular echoes, we used the turbulence echo received by the radial wind velocity channel of the RASS mode at the zenith angle of 14° for studying the characteristics of turbulence. We aspect sensitivity between the beams pointed at a zenith angle of 14° to that of the vertical beam. The averaged ratio value along the altitude became more than -13 dB. So we assumed that the influence of the specular reflection in the clear air echoes at the zenith angle of 14° is sufficiently attenuated enough to be neglected.

The profiles of ε from the spectral width and from the echo power were compared. For the derivation of ε from the spectral width, we first discussed relative magnitudes of the broadening effects in comparison to the observed spectral width. The observation conditions were ideal for calculation of ε from the spectral width because all of the three broadening effects were small.

We found that ε from spectral width is mainly determined by the spectrum width, and the influence of N^2 is relatively small. On the other hand, ε from the echo power method shows fairly large time variations. We investigated the correlation among $\overline{\eta_{14}}$, ε, and N^2, and found that the correlation between $\overline{\eta_{14}}$ and ε is significant. On the other hand, it seems that time variation of ε is not greatly influenced by N^2. Although ε values from both methods are roughly on the same order, their statistical characteristics are fairly different. We suspect that ε from echo power is inaccurate because the term M in the calculation of ε is mainly determined by the humidity gradient, whose detailed temporal variations were not known.

The time variations of ε obtained from both methods were also discussed. An obvious correlation between ε from spectral width and σ^2_{turb} was seen, while a correlation between ε from spectral width and N was not found. Consequently,

the conventional derivation supposing a constant N would not be a bad approximation for this campaign. We thus investigated the accuracy of the conventional derivation. The error between ε utilizing a constant N and N_{RASS} averaged for 18 hours is about 18% at 9 km. In the disturbed condition, we can assume that the short-term variation of N becomes large, so the specific variation of N may have an influence on ε in such conditions.

A comparison of the temporal variations of ε with echo power, M^{-3}, and $\overline{\eta_{14}}^{3/2}$ showed that M^{-3} has no detailed fluctuation as in the case for $\overline{\eta_{14}}^{3/2}$ because the detailed humidity information was not known. ε from echo power has no large-scale trend because the trends of M^{-3} and $\overline{\eta_{14}}^{3/2}$ have a negative correlation. While, ε from echo power has a small-scale fluctuation effected by $\overline{\eta_{14}}^{3/2}$ because of the lack of the small-scale fluctuation in M.

Chapter 5

Humidity Profile Estimation Using Turbulence Echo Characteristics

5.1 Introduction

The previous chapter explained that the turbulence echo power in moist regions depends strongly on M, which in turn is mainly determined by $\mathrm{d}q/\mathrm{d}z$. Using the strong dependence of $\overline{\eta_{turb}}$ on $\mathrm{d}q/\mathrm{d}z$, a radar technique that can be used to determine a height profile of q in the troposphere has been developed.

As Equation (2.28) shows, $\overline{\eta_{turb}}$ depends mainly on M, N^2, ε. Because N^2 and ε can be estimated from, respectively, a RASS temperature profile and the Doppler spectral width of turbulence echoes, a linear relationship between η and M^2 can be derived where a proportional constant should be calibrated by referring to a simultaneous radiosonde measurement.

On the other hand, M below about 10 km depends mainly on $\mathrm{d}q/\mathrm{d}z$, and secondly on T and p (see Figure 4.9). Radar returns can therefore be used to estimate the heat and moisture fluxes [*Gossard et al.*, 1982]. The strong correlation between $\overline{\eta_{turb}}$ and $\mathrm{d}q/\mathrm{d}z$ was shown by comparing observations made with wind profiler radars and radiosondes [*Tsuda et al.*, 1988; *Hocking and Mu*, 1997]. Using the strong dependence of M on $\mathrm{d}q/\mathrm{d}z$, the height structure of $\mathrm{d}q/\mathrm{d}z$ was inferred from radar echoes observed with a wind profiler operating at 449 MHz [*Gossard et al.*, 1998]. Further, a profile of q at altitudes of 0.5–2.0 km was retrieved by incorporating information on PWV with GPS measurements [*Gossard et al.*, 1999]. The purpose of the study discussed in this chapter was to develop a radar technique for monitoring the q profile at 1.5–10 km that would use the

turbulence echoes occurring in a non-precipitating atmosphere.

First, we discuss the basic equation of $\overline{\eta_{turb}}$ in terms of ε, N^2, and M^2. Then, we introduce a method used to retrieve a q profile. However, since $|M|$ is derived from $\overline{\eta_{turb}}$, we need a method that uniquely determines the sign of M. We can infer the sign of $|M|$, which is delineated from the MU radar observations of $\overline{\eta_{turb}}$ by considering the correlation between $\mathrm{d}q/\mathrm{d}z$ and N^2, where N^2 is measured with RASS. Last, we compare the preliminary results from the determination of humidity based on the MU radar–RASS observations made on August 2, 1995 to simultaneously obtained radiosonde results. A similar comparison of results from another MU radar–RASS experiment on July 29–30, 1999, where seven humidity profiles were inferred every 6 hours, is also considered [*Tsuda et al.*, 2001].

5.2 Relation between $\overline{\eta_{turb}}$ and M

In a precipitation-free atmosphere, wind profiler radars operated on VHF frequency detect an isotropic scattering caused by the turbulence-induced refractive index fluctuations. The magnitude of M can be related to $\overline{\eta_{turb}}$, ε and N from Equation (2.28) as

$$|M| = D^{1/3}\varepsilon^{-1/3} N\sqrt{\overline{\eta_{turb}}}. \tag{5.1}$$

ε can be estimated from the width of the Doppler spectrum of turbulence echoes [e.g., *Hocking*, 1985]. While N^2 is determined from a temperature profile observed with RASS measurements. (Note that RASS gives virtual temperature (T_v), which is slightly higher than T in a moist region.)

Figure 5.1 shows a height profile of $|M|$ inferred from the MU radar–RASS observations of ε, N^2 and $\overline{\eta_{turb}}$ at 21:20 LT on August 2, 1995. Note that D is assumed constant along height. $\overline{\eta_{turb}}$ was determined by averaging the received echo power for four oblique beams for about 10 minutes. While ε is derived from the spectral width of Doppler spectra following the procedure of *Fukao et al.* [1994].

The vertical variation of $\varepsilon^{-1/3}$ in Figure 5.1 is rather small and N is also nearly constant except around 1.5 km. On the other hand, $\sqrt{\overline{\eta_{turb}}}$ in the right panel fluctuates significantly at 1.5–8 km. Therefore, the height structure of $\sqrt{\overline{\eta_{turb}}}$ is mainly determined by the behavior of M, while $\varepsilon^{-1/3}$ and N do not contribute significantly to the height variation of $\sqrt{\overline{\eta_{turb}}}$ [*Furumoto and Tsuda*, 2001].

Note that it is rather difficult to accurately calibrate all the system parameters of the MU radar, because a distributed receiver system with 475 pre-amplifiers is employed. So, the measured S/N may not be converted to the absolute volume reflectivity. For a practical application of Equation (5.1), we need to define a

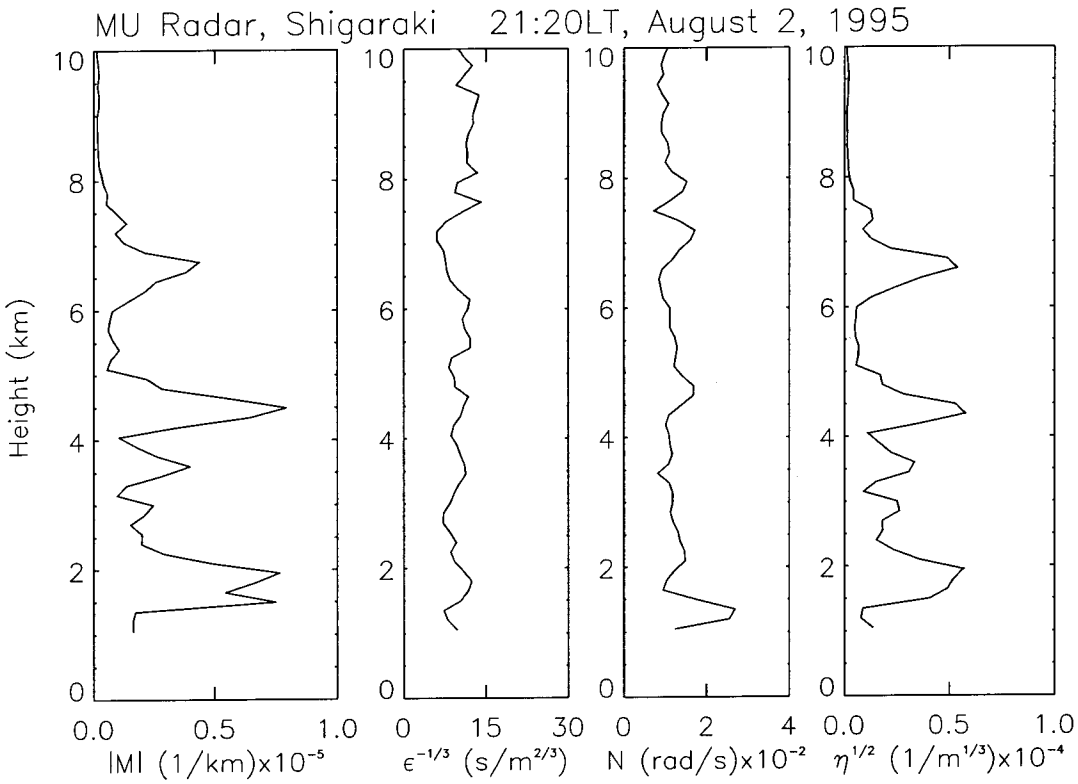

Figure 5.1: Profiles of $|M|$, $\varepsilon^{-1/3}$, N and $\sqrt{\overline{\eta_{turb}}}$ (from left to right) calculated from the MU radar–RASS observations at 21:20 on August 2, 1995.

proportion coefficient (A) between the true value of M and the radar-derived relative value (M^*) as

$$|M| = A|M^*|. \tag{5.2}$$

It is noteworthy that ε in Equation (5.1) is different from ε estimated from the Doppler spectral width by the volume filling factor (F) of turbulence layers. Assuming that F is a constant along altitude, its effect can also be absorbed in the factor A. Note, however, that the time and height variations of F induce errors in the proportion relation of Equation (5.2), as a result, it could produce spurious perturbations in an inferred profile of $|M|$.

It is necessary to calibrate A by comparing $|M^*|$ with $|M|$ from a simultaneous radiosonde sounding. A was calculated at 1.2–10 km by comparing $|M^*|$ in Figure 5.1 with a radiosonde result launched at 21:08 LT on August 2, 1995. Considering that it takes about 30 minutes for a radiosonde to ascend to 10 km altitude, we also averaged $|M^*|$ for about 30 minutes. Two averaging methods can generally be considered for estimating A. That is, A can be obtained by averaging the ratio $|M|/|M^*|$ determined at each height with an equal weighting. Or, A can be obtained by dividing the integrated value of $|M|$ by that of $|M^*|$. The latter determination method of A is preferable in this study, since it gives a better agreement between $A|M^*|$ and $|M|$ in height ranges of large $|M|$. During the MU radar–RASS experiment on July 29–30, 1999, A was calculated for 7 radar profiles by comparing them with simultaneous radiosonde profiles launched every 6 hours. The mean and standard deviation of A is 1.25 and 0.19, respectively, therefore, the relative variations of A can be estimated as about 15%.

5.3 Estimation of the q Profile

We discuss here the fundamental characteristics of M by analyzing radiosonde data. M in the lower atmosphere can be expressed from Equation (2.22) as:

$$M = -77.6 \times 10^{-6} \frac{p}{T} \left(\frac{N^2}{g} + 15600 \frac{q}{T} \frac{N^2}{g} - \frac{7800}{T} \frac{\mathrm{d}q}{\mathrm{d}z} \right). \tag{5.3}$$

In section 4.4.3, we investigated the relative contribution of these three terms to M and found that the height structure of M is mainly determined by $\mathrm{d}q/\mathrm{d}z$ in a moist layer, therefore, the profile of M is expected to correlate highly with that of $\mathrm{d}q/\mathrm{d}z$.

We can simplify Equation (5.3), neglecting the second term, because its contribution to M is small.

$$M = -\frac{77.6 \times 10^{-6} p}{T} \left(\frac{N^2}{g} - \frac{7800}{T} \frac{\mathrm{d}q}{\mathrm{d}z} \right). \tag{5.4}$$

Then $\mathrm{d}q/\mathrm{d}z$ can be approximated as

$$\frac{\mathrm{d}q}{\mathrm{d}z} = 1.65\frac{T^2}{p}M + \frac{T}{7800}\frac{N^2}{g} = 1.65\frac{T^2}{p}M + \frac{1}{7800}\left(\frac{\mathrm{d}T}{\mathrm{d}z} + \Gamma\right). \tag{5.5}$$

By considering Equation (5.1) between $|M|$ and $\overline{\eta_{turb}}$, enhanced echoes observed with a wind profiler radar coincide with large $|\mathrm{d}q/\mathrm{d}z|$ when the background temperature profile does not vary greatly. That is, the profile of $\overline{\eta_{turb}}$ can be related to the height structure of humidity distribution [*Furumoto and Tsuda*, 2001].

We now study the exact solution of Equation (5.3), which can be expressed as a first order differential equation for $q(z)$:

$$\frac{\mathrm{d}q}{\mathrm{d}z} + A(z)\,q = B(z), \tag{5.6}$$

where

$$A(z) = -\frac{2N^2}{g} \tag{5.7}$$

$$B(z) = 1.65\frac{T^2}{p}M + \frac{1}{7800}\left(\frac{\mathrm{d}T}{\mathrm{d}z} + \Gamma\right). \tag{5.8}$$

A general solution of Equation (5.6) becomes

$$q(z) = \frac{1}{e^{\int A(z)\,\mathrm{d}z}}\left\{\int B(z)\,e^{\int A(z)\,\mathrm{d}z}\mathrm{d}z + C_q\right\}, \tag{5.9}$$

where C_q is an integration constant. We can modify $\int A(z)\mathrm{d}z$ in Equation (5.9), considering that

$$\frac{N^2}{g} = \frac{\mathrm{d}\ln\theta}{\mathrm{d}z}, \tag{5.10}$$

which yields

$$\int A(z)\mathrm{d}z = -2\int\frac{\mathrm{d}\ln\theta}{\mathrm{d}z}\mathrm{d}z = \ln\theta^{-2}, \tag{5.11}$$

where θ is the potential temperature. Equation (5.9) can then be rewritten by taking an integration range between a reference height (z_0) and z as

$$q(z) = \theta^2\left\{\int_{z_0}^{z} B(z)\,\theta^{-2}\mathrm{d}z + C_q'\right\}, \tag{5.12}$$

where C_q' is a new integration constant. Applying the boundary condition, $q(z_0) = q_0$ and $\theta(z_0) = \theta_0$ at $z = z_0$, Equation (5.12) gives

$$C_q' = \frac{q_0}{{\theta_0}^2}. \tag{5.13}$$

Thus, the final form of Equation (5.9) becomes

$$q(z) = \theta^2 \left\{ \int_{z_0}^{z} B(z)\, \theta^{-2} \mathrm{d}z + \frac{q_0}{{\theta_0}^2} \right\}. \tag{5.14}$$

Note that we can adopt the climatological value for $p(z)$ in Equation (5.8) when a radiosonde result is not available, since time and height variations of p are small compared to those for q.

To summarize, we can calculate a $q(z)$ profile using Equation (5.14), with given values for q_0 and θ_0, if M is accurately determined from wind profiler radar observations of $\overline{\eta_{turb}}$ for turbulence echoes. It is noteworthy, however, that wind profiler radars can only determine $|M|$ from $\overline{\eta_{turb}}$, therefore, we need to develop a method to uniquely determine the sign of M. Moreover, it is difficult to take the boundary condition on the ground, because wind profiler radars are unable to measure the lowest part of the atmosphere (below about 1.5 km for the MU radar). Instead, we will assume that q becomes nearly zero at an upper boundary (for example, at 10 km). Then, Equation (5.14) can be integrated downward along the altitude.

5.4 Correlation between $\mathrm{d}q/\mathrm{d}z$ and N^2

Fluctuations of q and θ are not independent, but they are closely related through thermodynamics, especially for conservative vertical displacements [e.g., *Mapes and Zuidema*, 1996]. As a matter of fact, *Gossard and Sengupta* [1988] reported a good correlation between $\mathrm{d}q/\mathrm{d}z$ and N^2 under stable conditions. Now, we aim at verifying the correlation between $\mathrm{d}q/\mathrm{d}z$ and $\mathrm{d}\theta/\mathrm{d}z$ (or N^2) using radiosonde results. Figure 5.2 shows profiles of M, $\mathrm{d}q/\mathrm{d}z$, $-N^2$, and q observed with a radiosonde launched at 21:08 LT on August 2, 1995. Although N^2 was employed in Figure 5.2, its height structure is nearly the same as $\mathrm{d}\theta/\mathrm{d}z$, considering Equation (5.10).

We can see in Figure 5.2 that the profile of M is quite similar to that of $\mathrm{d}q/\mathrm{d}z$ as expected from the discussions in the previous section. Further, the height structure of $-N^2$ correlates well with that of $\mathrm{d}q/\mathrm{d}z$ such that the N^2 fluctuations become large at the altitudes where the magnitude of the $\mathrm{d}q/\mathrm{d}z$ is enhanced. As a result, we can see a good correlation between $-N^2$ and M. Note, however, that this relation may not be valid when the effects of horizontal advection become significant, as reported by *Mapes and Zuidema* [1996] from radiosonde results in tropics.

We would not expect, therefore, that the height structure of the magnitudes of M agree precisely with those of $-N^2$, since they are not necessarily proportional.

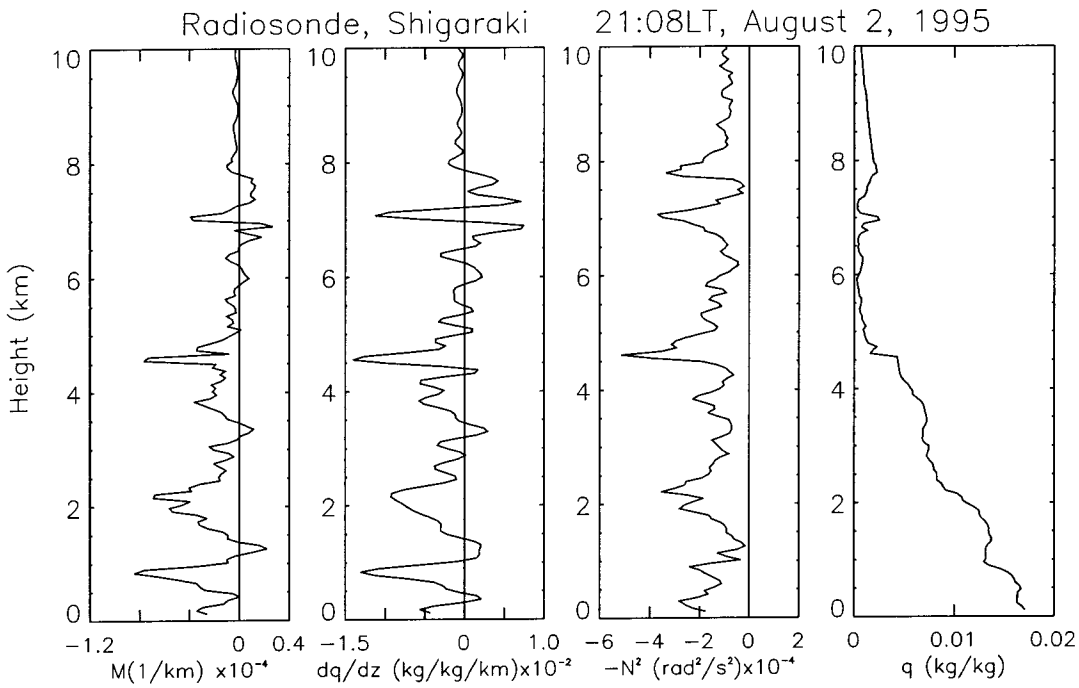

Figure 5.2: Profiles of M, $\mathrm{d}q/\mathrm{d}z$, $-N^2$ and q (from left to right) observed with a radiosonde launched at 21:08 LT on August 2, 1995.

However, in most radiosonde profiles that we have investigated, the height ranges with positive/negative M values coincide fairly well with the negative/positive fluctuations in N^2. Therefore, we can guess the sign on M from an asymptotic height structure of a $-N^2$ profile. It is noteworthy that the continuous temperature measurement with RASS is very useful in this study.

In higher altitude regions where q becomes small, M may not correlate with $\mathrm{d}q/\mathrm{d}z$ any more. But, M still seems to correlate with $-N^2$, considering the first term in Equation (5.3). So, the sign of M can be inferred from $-N^2$ in the entire height range.

It is important to define the threshold of $-N^2$ corresponding to $M = 0$ when we try to infer the sign of the radar-derived M based upon the correlation between M and $-N^2$. Although we could expect height variations of the threshold, we simply assumed a constant value at all altitudes, which is empirically determined as $-N^2 = -1.1 \times 10^{-4}$ s^{-2}. Then, we detected four height regions with positive M values; near 3.4 km, 4 km, 6.0–6.5 km and 7.4 km. the sign of M above 7.5 km was assumed to be negative, since the N^2 values did not significantly exceed the threshold. Moreover, it was assumed that M is negative below about 2 km

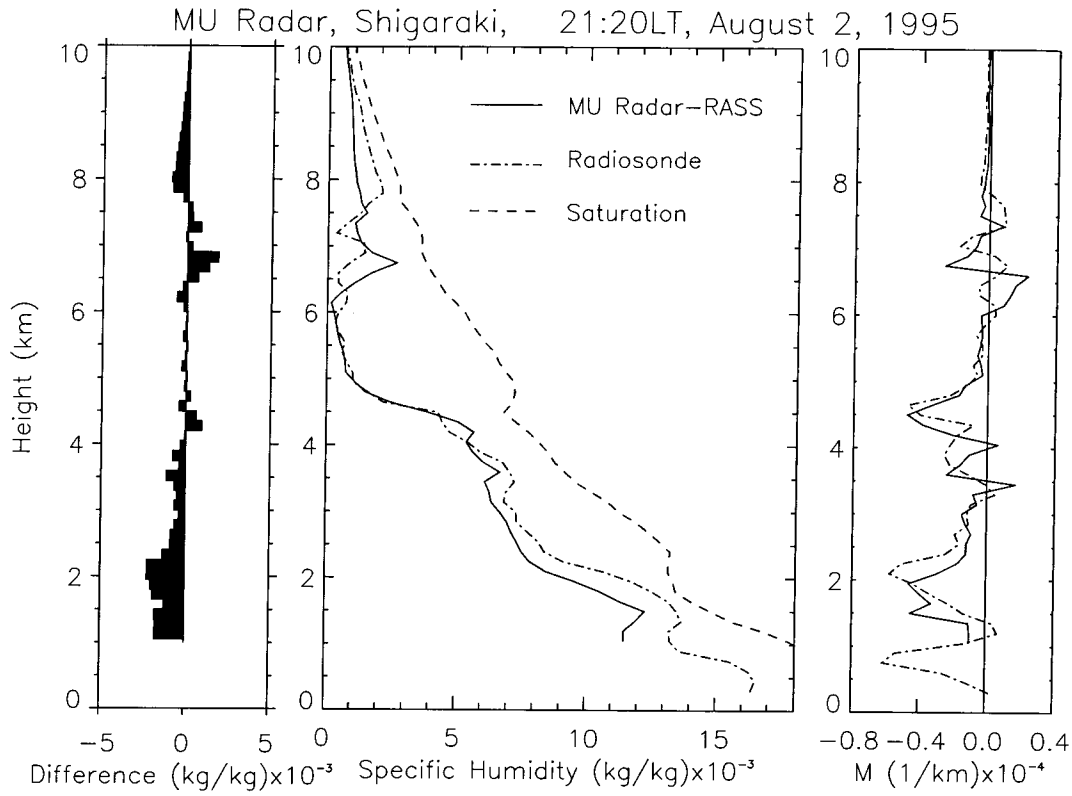

Figure 5.3: Comparison of profiles of q (center) and M (right) between the MU radar–RASS (solid) and radiosonde (dash dot) observations at 21:20 LT on August 2, 1995. A dashed line in the center panel show the saturation value of q (dashed) Left panel shows the difference of q between the radar and radiosonde results.

because the RASS temperature measurement was not accurate enough there.

5.5 The q Profile Derived from Echo Power

Figure 5.3 shows the profiles of q and M inferred from the MU radar–RASS observations, together with the reference radiosonde result at 21:08 LT on August 2. We used the radar profile collected about 12 minutes after the radiosonde release, considering the time delay necessary for a radiosonde to ascend to the height region of our interest. However, the time lag between the radar and radiosonde measurements was as large as about 20 minutes at 10 km, assuming the ascending speed of a balloon to be about 5 ms^{-1}.

In the right panel in Figure 5.3, the magnitude of M inferred from the MU

radar is similar to that of the radiosonde profile. In particular, the signs of M mostly agree with the radiosonde results, although disagreement occurred at around 4 km and 6–7 km. The discrepancy seems to be due to either a misjudgement of the sign of M, or the vertical and/or horizontal variations in q.

The q profile in Figure 5.3 is calculated by using Equation (5.14), where we took upper boundary values at $z_0 = 10$ km from the radiosonde results. The height structure of the radar-derived q profile generally agrees well with that from the radiosonde. In particular, even small height variations of q can be detected with the MU radar. However, Figure 5.3 also suggests that the M values with the MU radar at 1.5–4.0 km are smaller than the radiosonde results. The left panel indicates that the difference in q between the radar and radiosonde values ranges to -1.0×10^{-3} kg kg^{-1} between 2.5 and 4.0 km.

The discrepancy becomes as large as about -2.5×10^{-3} kg kg^{-1} below 2.5 km, probably because the error is accumulated due to the downward integration. Moreover, the echo power at the lowest range gates could be suppressed, because the sensitivity of a radar receiver does not fully recover from the blanking due to a transmitted pulse. This effect might explain the smaller q values with the radar at low altitudes. Nonetheless, the relative error of q is less than about 15% at the lowest range gate (1.2 km).

From another MU radar–RASS observations on July 29–30, 1999, 7 humidity profiles are consecutively estimated as shown in Figure 5.4, which are compared with simultaneous radiosonde profiles launched every about 6 hours. Profiles of $q(z)$ derived from radar echoes are generally consistent with the radiosonde profile, except for the result at 15 LT on July 29, 1999.

5.6 Effects of Boundary Condition

Here we discuss the effects of the error in q_0 at the top boundary. The dashed line in the center panel in Figure 5.3 shows the saturation value of q inferred from the radiosonde sounding. Above about 8 km the q profile from the radiosonde is close to the saturation value. We anticipate that ice particles were attached to the humidity sensor aboard the radiosonde, therefore, the humidity was not accurately measured, causing incorrectly large q values at high altitudes. Although the radiosonde results at the upper boundary (10 km) was used with Equation (5.14), they could generate a large initial error.

Instead, we could assume a boundary condition as $q_0 = 0$ at a significantly high altitude where q becomes very small. This method can be employed even when a reference radiosonde is not available. Another way is to refer to a climatological q profile. We analyzed a number of radiosonde results collected over Shigaraki,

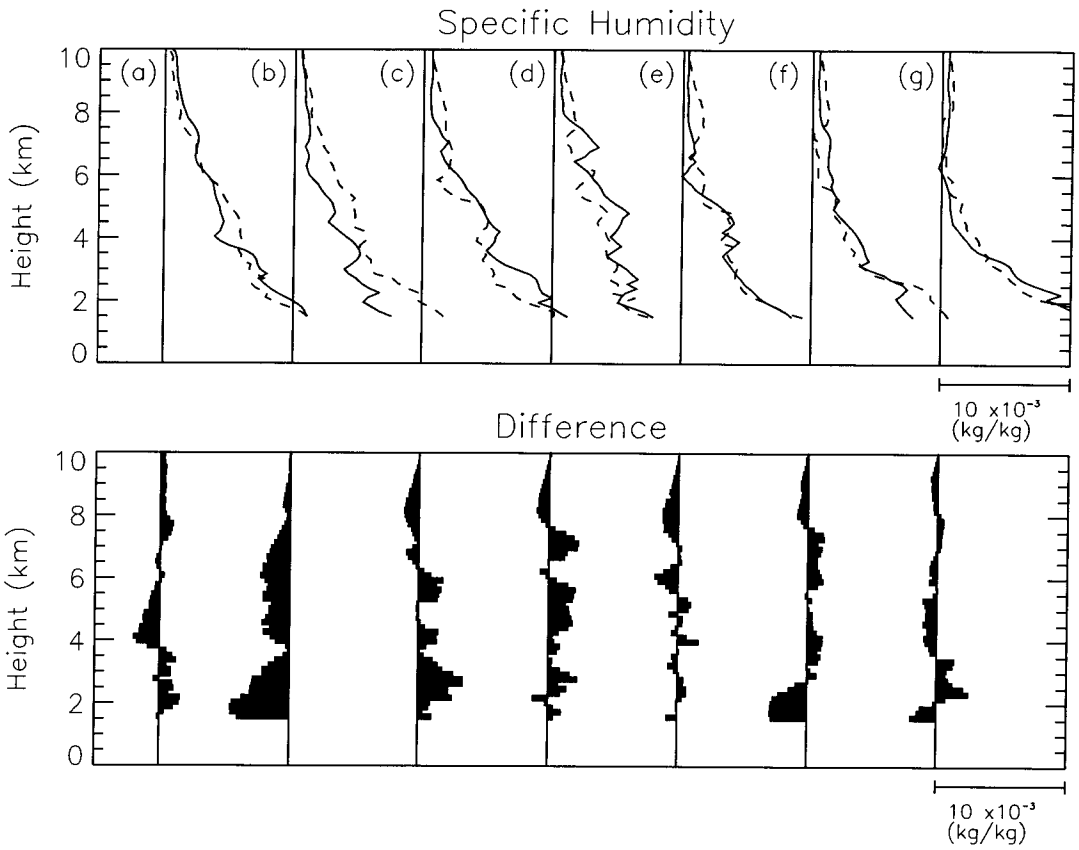

Figure 5.4: Comparison of 7 q profiles (top) between the MU radar–RASS (solid) and radiosonde (dash dot) observations on July 29–30, 1999. Launch time of the radiosondes was 8:45 LT, 14:52 LT, 21:02 LT on July 29, 2:32 LT, 8:44 LT, 14:45 LT and 20:37 LT on July 30, 1999, respectively, while we used radar data collected about 15 minutes after the balloon release. Bottom panel shows the difference of q for individual comparisons between the radar and radiosonde results.

and determined the mean q value, its standard deviation and the saturation value of q at 10 km as 3.1×10^{-4} kg kg^{-1}, 1.7×10^{-4} kg kg^{-1} and 7.3×10^{-4} kg kg^{-1}, respectively. In this case, the maximum error at the top boundary is restricted by the saturation q value. More practically, the error would be limited to the mean q value plus the standard deviation, that is, 4.8×10^{-4} kg kg^{-1}.

From Equation (5.14), an estimation error of q at z caused by inaccuracy of q_0 at the boundary (Δq) becomes

$$\Delta q\,(z) = \Delta q_0 \frac{\theta(z)^2}{{\theta_0}^2}. \tag{5.15}$$

Since θ normally decreases as the altitude descends, the magnitude of $\Delta q(z)$ is also reduced relative to Δq_0. That is, the effects of error at an upper boundary is suppressed for downward integration in Equation (5.14). For example, the discrepancy of 4.8×10^{-4} kg kg^{-1} at 10 km becomes as small as about 2.5×10^{-4} kg kg^{-1} at 1.5 km, which corresponds to about 3% of q (1.5 km).

5.7 Concluding Remarks

The MU radar–RASS observations were applied to the determination of a q profile, using the turbulence echo characteristics. In this paper, the details of the technique and the preliminary results from initial field tests under a moist (summertime) condition were described. Main conclusions of this study are summarized below:

1. Assuming the fundamental equation for the turbulence echoes, we obtained $M^2 \propto \varepsilon^{-2/3} N^2 \overline{\eta_{turb}}$. Since ε and N^2 can be determined from the Doppler spectral width and the RASS temperature profiles, respectively, $\overline{\eta_{turb}}$ is uniquely related to M^2. It was found that height variations of both ε and N^2 are small in comparison to those in M^2. It is noteworthy, therefore, that this technique could be applied to estimate M^2 at a wind profiler radar without the RASS capability.

2. A first-order differential equation for $q(z)$ is delineated, which can be solved, provided a profile of M is accurately determined from $\overline{\eta_{turb}}$. The proportionality constant relating $\overline{\eta_{turb}}$ and M^2 directly affects the amplitudes of q. So, for continuous monitoring of the humidity profile, it is preferable to calibrate time variations of this constant.

3. We proposed a method to estimate the sign of M from the correlation between $\mathrm{d}q/\mathrm{d}z$ and $-N^2$. Although we assumed that the threshold of N^2 for

determining the sign of M is constant with altitude, we should investigate its height variations in a future study. The present method is preliminary and it could be improved by combining other measurement techniques. Since M is normally negative, it is important to find regions of positive $\mathrm{d}q/\mathrm{d}z$, which seem to occur near the lower edges of clouds. So, it is useful to coordinate with a ceilometer measurement of the cloud bottom height. Moreover, $\mathrm{d}q/\mathrm{d}z$ seems to fluctuate around a melting layer, which can be identified from the RASS observations of the height of freezing temperature.

4. Overall height structure of the radar-derived q profile agrees well with a simultaneous radiosonde result. Difference of q values between the radar and radiosonde determinations mostly ranges 1.0–5.0 $\times$ 10^{-3} kg kg^{-1} at 1.5–7.0 km, although a significant discrepancy was sometimes recognized.

5. Magnitude of the error at the upper boundary is reduced when $q(z)$ is integrated downward. However, it is better to provide the boundary condition at the lower end where the q is larger. Since the MU radar is unable to measure the lowest part of the atmosphere (below about 1.5 km), it is difficult to give the boundary condition on the ground ($z_0 = 0$ km). A Raman lidar measurements of the humidity profile below a cloud layer could provide the boundary value at the bottom of the integration region. The error of q seems to be caused by various factors, such as the error of q_0, ε and A and the misjudgement for the sign of M. This chapter discussed the effects of boundary condition. In the next chapter, we will discuss the effects of A and ε and the improvement of the guess method of the sign of M.

We demonstrated that the radar technique proposed in this study has a potential to continuously determine the specific humidity profile. By combining results from other remote-sensing measurements an integrated observation system may be designed to provide complete information about the vertical structure of humidity.

Chapter 6

Continuous Monitoring of Humidity Profiles with the MU Radar–RASS

6.1 Introduction

This chapter looks at an important improvement made to the radar remote-sensing technique used to obtain q profiles. As explained in the previous chapter, we can retrieve a q profile by inferring the sign of M from the correlation between M and $-N^2$. However, M is not fully correlated with $-N^2$ under disturbed meteorological conditions. To achieve a more robust estimation of the q profile under various meteorological conditions, we improved the method by delineating the sign of M through simultaneous GPS measurements of PWV [*Furumoto et al.*, 2002].

We begin by describing the experimental set-up, which was in operation from July 29 to August 4, 1999, and the method used to retrieve humidity profiles. The q profiles are compared to simultaneously obtained radiosonde data, which is followed by a discussion of the correlation between the radar-derived q and the black body temperature (TBB) obtained through irradiance (IR) measurement done with a geostationary meteorological satellite (GMS). After that, we look at the detailed time-height structure of the retrieved q, referring to the rain echo distribution obtained from a meteorological radar. The behavior of the radar-derived q, wind velocity, ε, and T is described, along with that of meteorological parameters observed from the ground, and the correspondence of these behaviors to the movement and the development or decay of rain clouds observed by meteorological radar is discussed.

6.2 MU Radar–RASS Campaign during July 29 and on August 4, 1999

The MU radar–RASS can monitor successive profiles of three components of wind velocity and T_v with time and height resolution of a few minutes and 150 m, respectively. Our MU radar–RASS observation was done over nearly one week from 08:36 LT on July 29 to 21:21 LT on August 4, 1999. The observation parameters are summarized in Table 6.1. We repeatedly observed turbulence and RASS echoes in two height ranges from 1.2 to 10.7 km (low mode) and from 4.80 to 23.85 km (high mode). Each observation cycle took 2.4 minutes.

To observe the turbulence echoes, we steered the radar beam into five positions: one vertical and four oblique directions at a zenith angle of 10°, aligned to the north, south, east, and west. During rainfall, both turbulence and rain echoes are detected by the MU radar. Both types of echo can be analyzed, but only the turbulence echoes were used in this study.

For the RASS observations, we used 20 hyperbolic horn speakers and transmitted an FM chirped acoustic wave whose sweep frequency range was adjusted to satisfy the Bragg condition in the observation-height range. The antenna beam directions were appropriately changed by considering the results of real-time ray-tracing of acoustic wavefronts. Two independent receiver channels were used: one for the radial wind velocity, and one for the acoustic velocity with a local reference signal shifted by 105.5 Hz and 92.6 Hz in the low and high modes, respectively.

To obtain reference humidity profiles, we launched 55 radiosondes every 3 hours at 0, 3, 6, 9, 12, 15, 18, and 21 LT each day in parallel with the MU radar–RASS observations. We used the VAISALA RS-80-15G radiosonde, whose measurement accuracy is 2–3% for relative humidity with a height resolution of a few hundred meters [e.g., *Miloshevich et al.*, 2001]. The radiosonde results were averaged over 150 m of altitude to obtain the same height resolution as with the MU radar results.

We also made continuous surface meteorological observations at the MU radar site by recording the pressure, temperature, humidity, and precipitation with a time resolution of 1 minute. A GPS receiver (Ashtech Z-XII3) was simultaneously operated, which detected the signal from GPS at elevation angles greater than 15° with a sampling interval of 30 seconds. The GPS data was analyzed with the GIPSY-OASYSII software developed at NASA's Jet Propulsion Laboratory (JPL) and the PWV was determined with a time resolution of 5 minutes. We also measured PWV by a dual-frequency microwave radiometer (WVR; Radiometrics WVR-1000), operated at 20.7 and 31.4 GHz, with a time resolution of about 1 minute. During this observation, the WVR was programmed to point only toward

Table 6.1: Observation parameters of the MU radar–RASS experiments from July 29 to August 4, 1999.

Turbulence Echo Observation		
	Low Mode	High Mode
height range (km)	1.20–10.65	4.80–23.85
inter-pulse period(μs)	450	400
sub-pulse length (μs)	1	1
pulse compression bit	2	16
number of beams	5	5
coherent integration	10	60
number of FFT points	256	128
incoherent integration	5	2
observation duration (s)	54	44
beam direction (azimuth angle, zenith angle)	(0°, 0°), (0°, 10°), (90°, 10°), (180°, 10°), (270°, 10°)	

RASS Observation Parameter		
MU radar		
	Low Mode	High Mode
height range (km)	1.20–10.65	4.80–23.85
inter-pulse period (μs)	450	434
sub-pulse length (μs)	1	1
pulse compression bit	2	16
number of beams	3	4
coherent integration	10	16
number of FFT points	256	256
incoherent integration	5	5
observation duration (s)	54	45
Acoustic Source		
transmitter type	hyperbolic horn speaker	
wave form	CW	
repetition period (s)	1.0	
chirped frequency range (Hz)	72.3–109.2	

the zenith direction.

6.3 Estimation of the q Profiles

6.3.1 Theoretical Background

The principle underlying the estimation of a humidity profile using turbulence echo characteristics was given in section 5.3. $\overline{\eta_{turb}}$ basically depends on M^2, N^2 and ε. Thus, we can derive $|M|$ provided N^2 and ε can be estimated from, respectively, the RASS temperature profiles and the spectral width of the Doppler spectrum of turbulence echoes.

Further, M is related to q, $\mathrm{d}q/\mathrm{d}z$, T, and p from Equation (2.22). By solving a first-order differential equation, the height structure of q can be estimated. Note, however, that the sign of the radar-derived M must be determined. $q(z)$ can be solved from Equation (5.14) as shown:

$$q(z) = \theta^2 \left\{ \int_{z_0}^{z} \theta^{-2} \left[1.65 \frac{T^2}{p} M + \frac{1}{7800} \left(\frac{\mathrm{d}T}{\mathrm{d}z} + \Gamma \right) \right] \mathrm{d}z + \frac{q_0}{{\theta_0}^2} \right\}, \quad (6.1)$$

where $q(z_0) = q_0$ and $\theta(z_0) = \theta_0$ are the boundary conditions. Because the MU radar can obtain only the absolute value of M, to precisely estimate q we must unambiguously determine the sign of M. *Tsuda et al.* [2001] successfully retrieved a q profile by inferring the sign of M from the correlation between M and $-N^2$. *Mapes and Zuidema* [1996] showed that q and θ are closely related in terms of the vertical displacement under adiabatic and non-advective conditions. Therefore, $\mathrm{d}q/\mathrm{d}z$ and $\mathrm{d}\theta/\mathrm{d}z$ should be correlated, and M thus closely related to $-N^2$. However, under disturbed meteorological conditions, M is not fully correlated with $-N^2$.

To achieve a more robust estimation of the q profile under various meteorological conditions, we improved the method used to delineate the sign of M by using simultaneous PWV measurements made by GPS. Figure 6.1 shows the block diagram of the method we used to retrieve q.

We derived ε from the spectral width of the turbulence echoes (σ_{turb}) and N^2 from the RASS. Note, however, that the observed spectral width was affected by broadening effects. We removed these effects using the horizontal wind velocity and vertical wind shear observed with the MU radar by *Hocking* [1995]'s method.

As the MU radar did not have a noise-power calibration system, only the S/N could be obtained, so we derived the relative value of $\overline{\eta_{turb}}$ from the S/N. The relative value of $|M|$ ($|M^*|$) was then calculated from ε, $\overline{\eta_{turb}}$, N^2, and F from

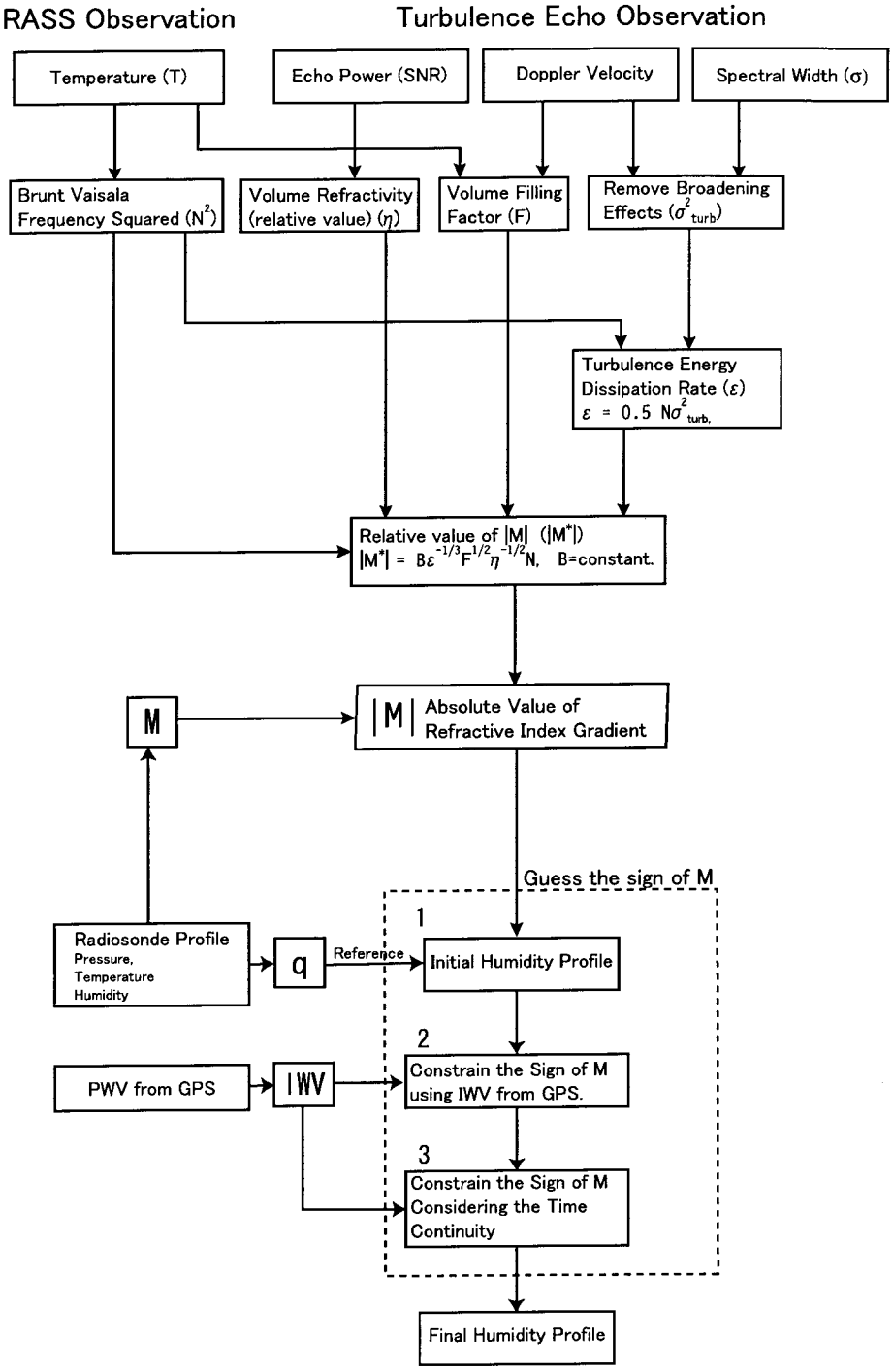

Figure 6.1: Block diagram of an improved retrieval method for estimating q profiles.

Equation (2.27) as

$$|M^*| = \varepsilon^{-1/3} F^{1/2} \overline{\eta_{turb}}^{-1/2} N. \tag{6.2}$$

Note that Though F is included in the relationship between $\overline{\eta_{turb}}$ and the received echo intensity, the exact value of F is difficult to determine from actual observations. We employed the method of *Cohn* [1995] to derive F using the high-resolution wind and temperature profiles we obtained from the MU radar–RASS measurements. The MU radar cannot obtain $|M|$, only $|M^*|$ which contains the system parameter, so we obtained $|M|$ by calibrating $|M^*|$ using the M derived from simultaneous radiosonde results.

6.3.2 The Effects of F and ε on q

In a previous study by *Tsuda et al.* [2001], q profiles were estimated using a constant F versus height derived from simultaneous radiosonde results. We estimated F using the *Cohn* [1995] method from temperature profiles obtained with the MU radar–RASS with good temporal and height resolutions. The mean profile of F estimated with the *Cohn* [1995] method during the campaign ranged between 0.10–0.18, with s.d. of 0.07. We studied the effects of F on the estimated q. That is, we calculated the normalized discrepancy between two estimations of q using the F given by *Cohn* [1995] and a constant F value, respectively. The mean discrepancy over 36 hours was as small as about 10% below 5.3-km altitude, and above 5.3 km the normalized discrepancy fluctuated with a maximum difference of 50%. This large fluctuation may not be meaningful, though, because q becomes small at higher altitudes. The accuracy of the q estimated using the *Cohn* [1995] method below 5.3 km therefore seems to be improved by 10% compared to the value given by *Tsuda et al.* [2001]. While F has been estimated using high-time-resolution temperature data from the MU radar–RASS measurements in this study, only data with low time resolution (such as from radiosondes) may be available in other experiments, in which case the errors of the estimated q's could rise to about 10%.

We also studied the effects of ε on the estimated q. The mean profile of ε estimated from the MU radar–RASS measurement during the campaign fluctuated between 0.5×10^{-3} and 3.0×10^{-3} m^2s^{-3}. The mean and s.d. of ε versus height were 1.5×10^{-3} m^2s^{-3} and 2.5×10^{-3} m^2s^{-3}, respectively, and the variation of ε seemed large. We studied the normalized discrepancy between the two estimations of q with ε with a time resolution of 2.4 minutes and the mean ε profile during the campaign. The discrepancy was as small as 15% below 4.8 km. However, the normalized discrepancy fluctuated between 20 and 40% above 4.8 km. Thus, the estimated q may have had an error of about 15% when ε

was not derived with high time resolution. During the campaign there was little background wind and shear (as described later) which was ideal for estimating ε. When the wind is strong, it is more difficult to accurately determine ε because the broadening effects may become very powerful. The accuracy of the estimated q would probably worsen in such a case because of the higher estimation error of ε.

6.3.3 Determining the Sign of M

We determined the sign of M through three processes as indicated in the dashed box in Figure 6.1:

1. Radiosonde data taken every 6 hours were interpolated with time to make a reference q profile. The sign of M was considered to be that which made the radar-derived q agree with the reference q profile. Although we launched radiosondes every 3 hours, only the soundings at 3, 9, 15, and 21 LT (with intervals of 6 hours) were used to obtain the humidity profile. The other soundings (at 0, 6, 12, and 18 LT) were used to verify the accuracy of the radar-derived q profile.

2. The integrated water vapor (IWV) value between 1.5 and 7.5 km was calculated from the radar-derived q, and compared with the IWV simultaneously determined through GPS measurement. The reference IWV was inferred from PWV as:

$$\mathrm{IWV} = \mathrm{PWV} \times \mathrm{R}_{1.5km}. \tag{6.3}$$

   $\mathrm{R}_{1.5km}$ is the ratio of IWV at 1.5–7.5 km to the PWV determined from radiosonde data, interpolated to correspond to the radar time resolution. The sign of the first guess within the two height points was adjusted to minimize the difference between the IWV values if the difference in the IWV values exceeded a threshold. The threshold was equal to three times the s.d. for the IWV obtained by GPS measurements after removing the linear trend for 3 hours.

3. To suppress the rapid variation in q at each height, the sign of M was changed to make the time deviation of q smaller than the s.d. of q during each 15-minute period.

In the second process, the reference IWV estimated from GPS measurements represents the average value for a wide area around the MU radar, while the MU radar observed IWV only in a narrow area within a zenith angle of less than 10°

above the MU radar. Thus, the IWV was likely to differ from that estimated by GPS when the humidity distribution had a large horizontal gradient. This effect is discussed later in this paper.

6.4 Background Meteorological Conditions

Figure 6.2 shows the mean profile of eastward (u), northward (v), and vertical (w) wind velocities and temperature (T) measured with the MU radar–RASS.

The amplitude of w is magnified by a factor of 10 for clarity. The horizontal bars in Figure 6.2 show the s.d. of each value. Since the s.d. of u was similar to that for v, we did not show it.

Both u and v were small, since the jet stream was very weak. Below 6 km, u and v were as low as 3–6 ms^{-1} and 6–10 ms^{-1}, respectively, and the horizontal wind direction was roughly SSW. Above 6 km u and v became smaller as the height increased, both falling as small as $1\mathrm{ms}^{-1}$ at 9 km. Around 5.5 km, the s.d. of v reached a maximum of about 3 ms^{-1} and became smaller with height above 5.5 km. w was fairly small throughout the entire height range. The s.d. of w decreased with height from 0.35 ms^{-1} at 2 km to 0.15 ms^{-1} at 9 km. The temperature became 0°C around 4.5 km, and the s.d. of T was less than 1.5 K except at 6 km where it rose to about 2 K.

Figure 6.3 shows an IR image of the area around Japan observed by GMS at 17:40 LT on July 30. The asterisk in Figure 6.3 indicates the location of the MU radar. SE of the MU radar, a Pacific anti-cyclone can be recognized as a wide clear air region. A typhoon to the south of the MU radar did not produce significant meteorological disturbances near the MU radar.

The left panel of Figure 6.3 shows a 2000-km-wide cloud band spread along the SW-NE direction NW of the MU radar. The geostrophic wind blowing around the NW edge of the Pacific anti-cyclone caused the NE advection of this cloud band.

An enlarged image around the MU radar, corresponding to the box in the left panel, is shown in the right panel of Figure 6.3. At the edge of the cloud band NW of the radar there were several small cloud clusters with lengths and widths of about 100 km and 10 km, respectively. Such small clouds were generated and dissipated one after another within a few hours, and some clouds passed over the MU radar. The GMS also routinely observed visible images during the daytime that showed the region within 50 km of the MU radar was fully covered by dense cloud.

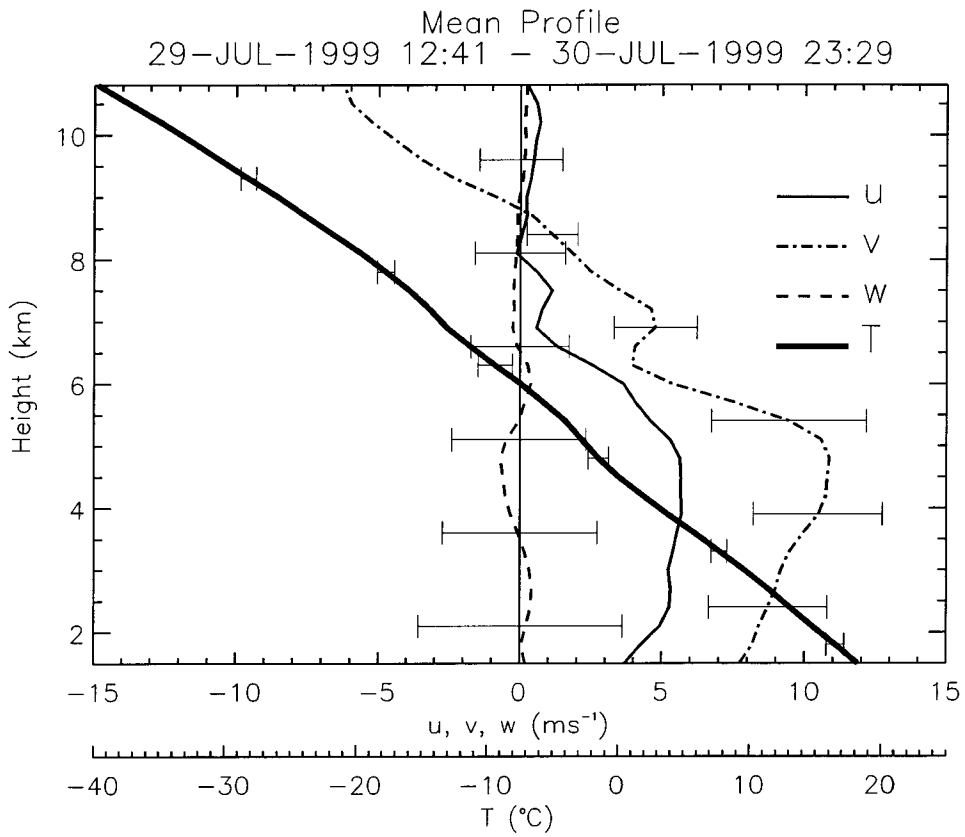

Figure 6.2: Mean profiles of zonal (u: solid), meridional (v: long-dashed), and vertical wind velocity (w: short-dashed) and temperature (T: thick solid) observed with the MU radar–RASS from 12:41 LT on July 29 to 23:29 LT on July 30, 1999. The error bars of v, w and T show s.d. of each value. The value of w and s.d for w are magnified 10 times.

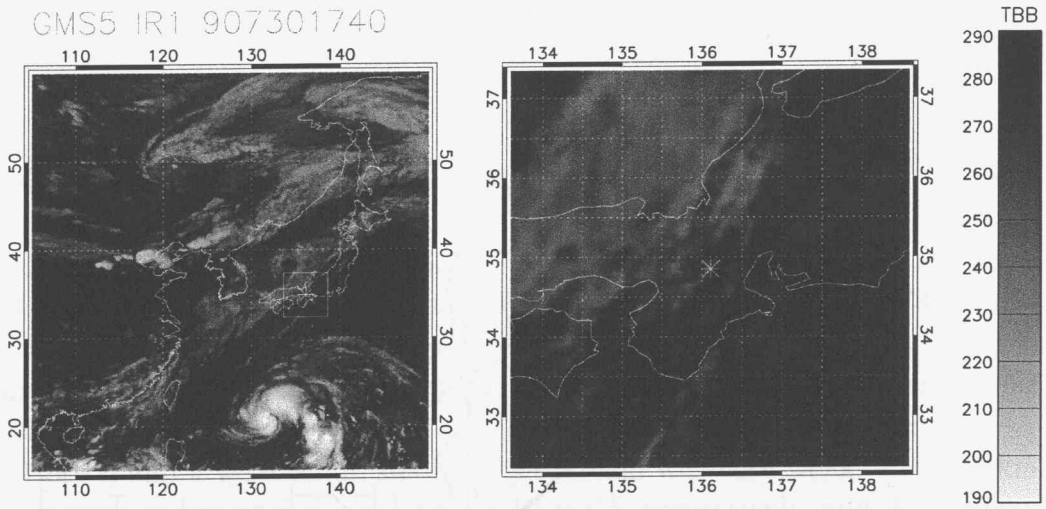

Figure 6.3: Infrared images obtained by GMS at 17:40 LT on July 30. The asterisk indicates the location of the MU radar. The right panel is an enlarged image of the box in the left panel.

6.5 The q Profiles Obtained with the MU Radar–RASS

Using the improved retrieval method we estimated successive humidity profiles from 08:36 LT on July 29 to 21:21 LT on July 30 operating the MU radar–RASS continuously. During this period, the PWV values obtained from the GPS and from a radiometer simultaneously operated at the MU radar site agreed to within 5 mm. As shown in the previous chapter, the accuracy of the radar-derived q is improved when the boundary condition is taken at a higher altitude. Considering the decrease in the turbulence echo power with height, we used an upper boundary of $z_0 = 7.5$ km where the S/N was fairly high and time variation of q was sufficiently small. The boundary values, q_0, θ_0, and pressure (p) in Equation (6.2) were inferred by linear interpolation of radiosonde soundings with respect to time. The top panel of Figure 6.4 shows the time variation of IWV (1.5–7.5 km) measured with the MU radar. GPS and radiosonde results are also plotted for comparison. The radar values were averaged over about 30 minutes. The error bars show three times the s.d. of the IWV obtained from GPS measurements after subtracting the linear trend. The radar-derived q may contain a small, yet not

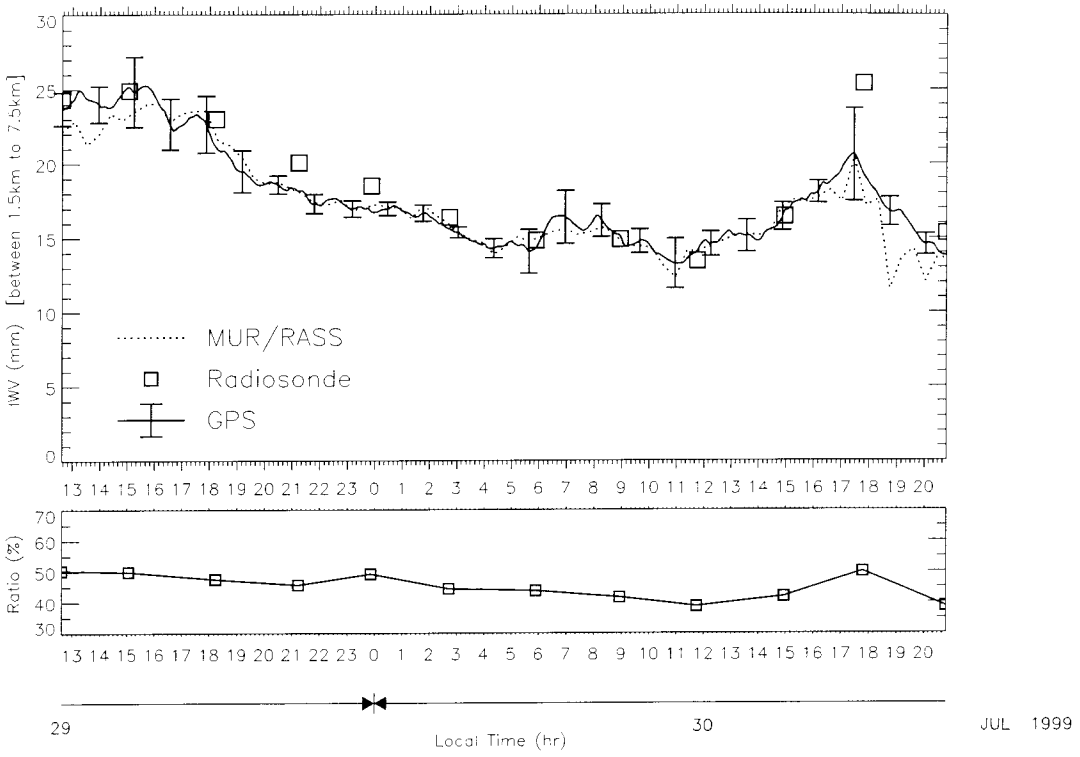

Figure 6.4: Time variation of IWV from 1.5 to 7.5 km (top) calculated from MU radar-derived q (solid), the GPS-derived IWV (dotted) and radiosonde data (squares). The bottom panel shows the time variation of a ratio of the humidity at 1.5–7.5 km to the PWV obtained from radiosonde data.

negligible, error when q above 7.5 km is measured.

The bottom panel of Figure 6.4 shows the time variation of $R_{1.5km}$ which was calculated from radiosonde data taken every three hours. In this analysis, $R_{1.5km}$ ranged mostly from 40 to 60% without fluctuating sharply over time, so the effect of the short-term variation of $R_{1.5km}$ on the IWV value measured by GPS is likely to have been small. The IWV values obtained through GPS and radiosonde measurements agreed well, and IWV with GPS seems to have been well-estimated except for some points at 21:00 LT on July 29 and at 0:00 and 18:00 LT on July 30. The radiosonde-derived IWV at 21:00 LT on July 29 and at 0:00 LT on July 30 was 2 mm larger than that with GPS. However, the radiosonde-derived IWV was 5 mm larger than that with GPS at 18:00 LT on July 30. We attributed this large discrepancy to an estimation error for the radar-derived q. Note that the radiosondes were drifted toward NE by the wind. However, the mean horizontal distances between the radiosonde and the radar site were as small as 2.4, 9.6 and

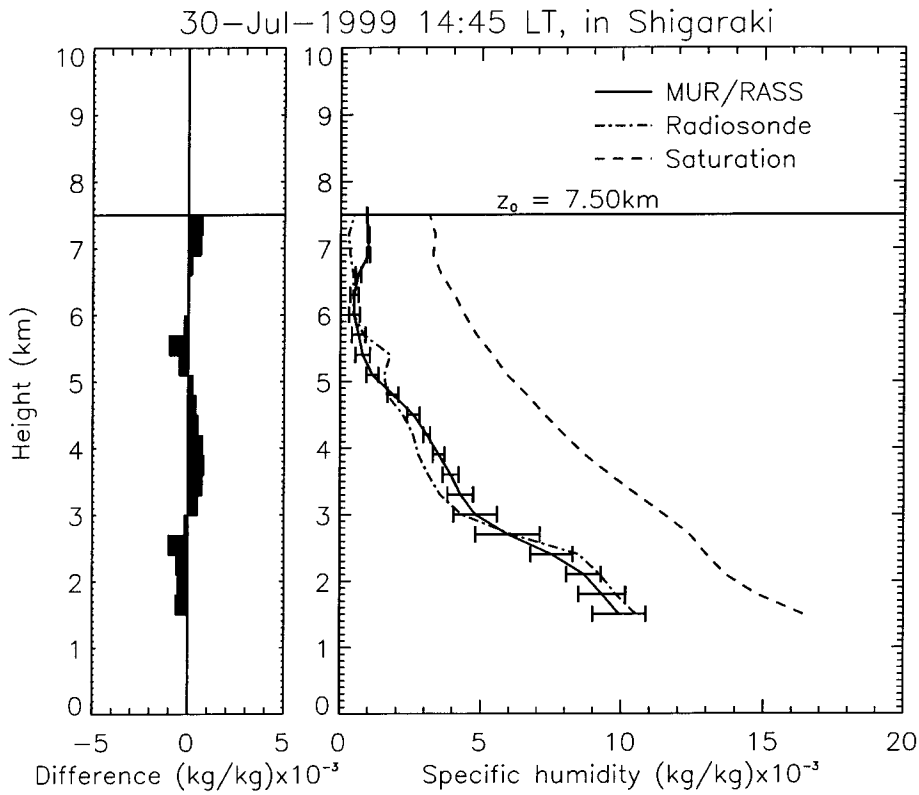

Figure 6.5: Comparison of q (right) from MU radar–RASS observations (solid) and a radiosonde (dash dot) launched at 14:36 LT on July 30, 1999. The error bars shows the s.d. for the radar results. Note that the dashed line indicates the saturation line. The left panel shows the difference in q between the radar and radiosonde results.

12.6 km at the height of 2.0, 5.0 and 7.5 km, respectively.

The radar-derived humidity is constrained by the IWV obtained by GPS in our retrieval procedure, so it is not surprising that the IWV obtained with radar agreed well with that obtained with GPS in Figure 6.4. The IWV showed a diurnal variation with a maximum and minimum around 17:00 LT and 7:00 LT, respectively. However, the radar-derived IWV fluctuated with a time scale of about 1.5–2 hours from 15:00 to 20:00 LT on July 30 in Figure 6.4.

Figure 6.5 shows a profile of q inferred from the MU radar–RASS observation. Data from the radiosonde launched at 14:36 LT on July 30 is also plotted for comparison. The radar-derived q (hereafter, referred to q_R) was averaged over 30 minutes from the launch time of each radiosonde to account for the interval needed by a radiosonde to ascend to an altitude of 10 km. The horizontal bar

shows the standard error of the radar data obtained over the 30-minute period. In the right panel of Figure 6.5, the height structure of the radar-derived q_R profile agrees very well with that from the radiosonde (hereafter, referred as q_s), although at 3–4.5 km and 5.0–5.8 km the difference exceeded the standard error of q_R. The left panel shows that the difference between q_R and q_s was within 1.5×10^{-3} kg kg^{-1} between 1.5 and 7.5 km.

q_s was larger than q_R at 5.5 km, this was above the melting layer at 4.5 km where the q_s was larger in other periods such as from 14:00 LT on July 29 to 6:00 LT on July 30 as we will show later.

6.6 Detailed Time-Height Structure of q

Figure 6.6 shows the time-height variation of relative humidity (RH) inferred from the MU radar–RASS data (RH_R) (bottom) and radiosonde data (RH_s) (top). We estimated individual humidity profiles with the intrinsic time resolution of the MU radar observation (2.4 minutes) and averaged eight profiles obtained over about 30 minutes. On the other hand, we launched radiosondes every 3 hours at the times indicated by asterisks below the top panel. Thick contour lines (purple, blue, orange and red) correspond, respectively, to 50, 60, 70, and 80% RH.

The asterisks connected by a thin line show the cloud-top height in a cell of 0.05° × 0.05° in longitude and latitude (about 4.6 × 4.6 km) around the MU radar, which was located near the center of the cell. The cloud-top heights were estimated from the TBB by referring to simultaneous temperature profiles obtained with RASS. Note that the cloud-top height is an instantaneous value at 40 minutes after the hour. We compared the TBB values used in Figure. 6.6 with other TBB values in the neighbouring cells and found that they agreed to within 5 K except from 13:40 to 15:40 LT on July 29 and from 15:40 to 18:40 LT on July 30 when the TBB difference became as large as 10 K.

The bottom panel of Figure. 6.6 shows the time variation of RH at the cloud-top height from both radiosonde and radar data. Under calm meteorological conditions from 22:40 LT on July 29 to 0:40 LT on July 30, the RH values at the cloud top agreed well. However, during disturbed conditions from 12:40 to 20:40 LT on July 29 and from 13:40 to 21:40 LT on July 30, RH_R at the cloud-top height was lower than RH_s by about 10%. This discrepancy was probably caused by a difference in the horizontal observation area between GPS which is used to constrain q_R and the radiosonde. We will discuss this point later. Although RH_R were somewhat lower than RH_s, the overall structure of the RH height-time variation obtained by the two methods was consistent.

The cloud top height had two distinct peaks at 6.5 km at 15:40 LT on July

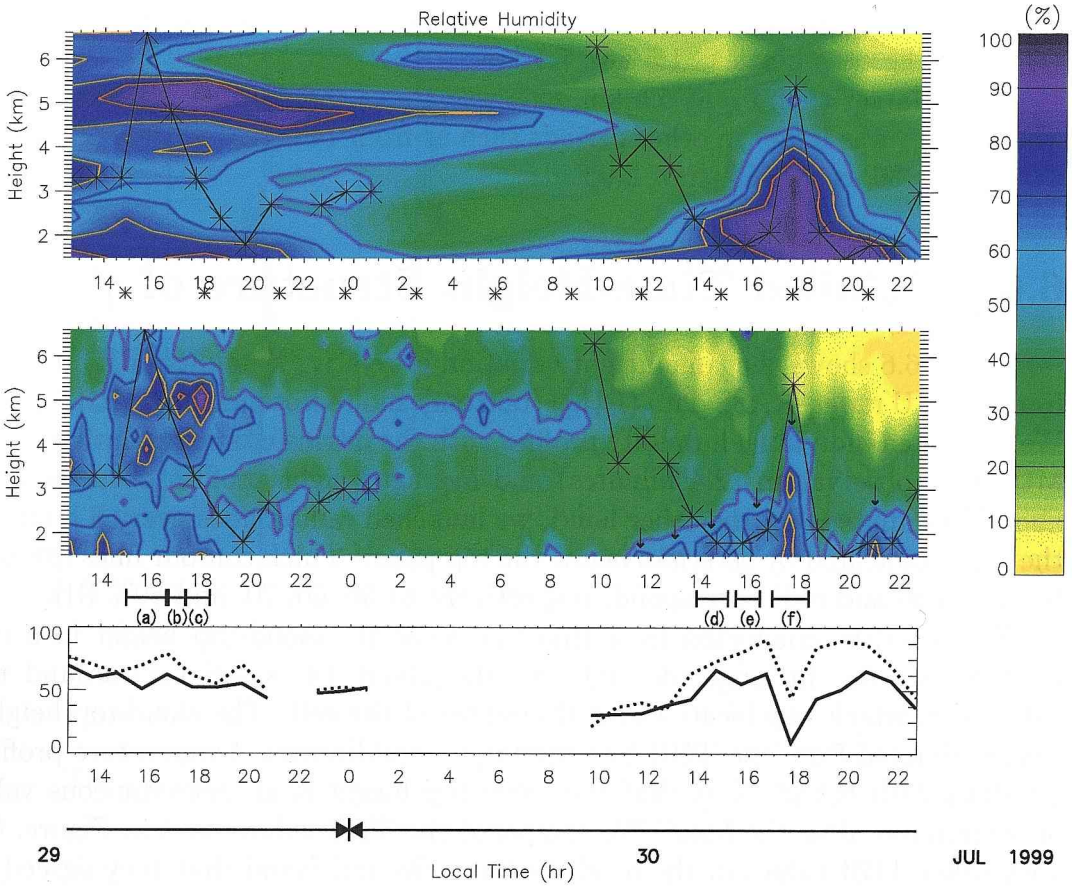

Figure 6.6: Time-height variation of RH observed by radiosondes launched every 3 hours (top) and those estimated with the MU radar–RASS after averaging for 30 minutes (middle) from 12:41 LT on July 29 to 23:29 LT on July 30, 1999. Asterisks connected by the line show the cloud top height derived from GMS data. (a), (b), (c), (d), (e) and (f) show the timing of rain clouds passing near or over the MU radar. The bottom panel shows the time variation of RH at the cloud-top height from both radar (solid) and radiosonde (dotted) data.

29 and 5.5 km at at 17:40 LT on July 30, respectively. From 9:40 to 14:40 LT on July 30, the cloud-top height steadily decreased from 6.3 km to 1.8 km except at 11:40 LT when a small peak appeared at 4.3 km. Radiosonde results show a region of RH_s >70% at 4.5–5.5 km, from 13:00 LT on July 29 to 6:00 LT on July 30, which did not agree with the cloud-top height. An enhancement was also detected in RH_R, which agreed better than the radiosonde results with the behavior of the GMS cloud top height.

RH_R in the afternoon on July 30 shows a single peak, which ascnded and descended during 12:40–17:40 LT and 17:40–22:40 LT, respectively. The increase in the cloud-top height at 17:40 LT on July 30 continued for only a few hours, which was shorter than the variation in the RH_s. RH_R showed several peaks from 12:00 to 22:00 LT on July 30, and the RH_R peak at about 17:40 LT agreed with the structure of GMS cloud-top height better than RH_s.

6.7 Behavior of Rain Clouds Passing over the MU Radar

During our observations, we monitored the real-time display of rain echoes measured by a meteorological radar located in Osaka about 60 km WNW of the MU radar. The Osaka radar observed rain echoes at the height of 2 km with a horizontal resolution of 2.5×2.5 km every 7 minutes. Rain clouds passed over or near the MU radar six times during the afternoons of July 29 and 30 and we describe the detailed characteristics of these rain clouds in the following which are useful to understand the behavior of RH in Figure 6.6.

6.7.1 Rain Clouds from 13:00 to 18:00 LT on July 29

In the afternoon of July 29, three rain clouds approached the radar site at (a) 16:07 LT, (b) 17:07 LT, and (c) 18:07 LT (as indicated in Figure 6.6). Rain clouds were blown toward NNE at about 10 ms^{-1} by the background winds. No rainfall was detected at the radar site during the cloud passages. The behavior of individual rain clouds is shown in Figure 6.7.

(a) A rain cloud appeared 15 km south of the MU radar at 15:15 LT. Moving toward NNE at 10 ms^{-1}, the rain cloud became most developed at 15:30 LT when it had a radius of about 8 km. The rain cloud in the decay stage migrated northward and came nearest to the MU radar at 16:00 LT when the center of the 6-km-radius cloud was 8 km SE from the MU radar. At 16:07 LT, a new rain band that was 6 km wide and 20 km long and spread

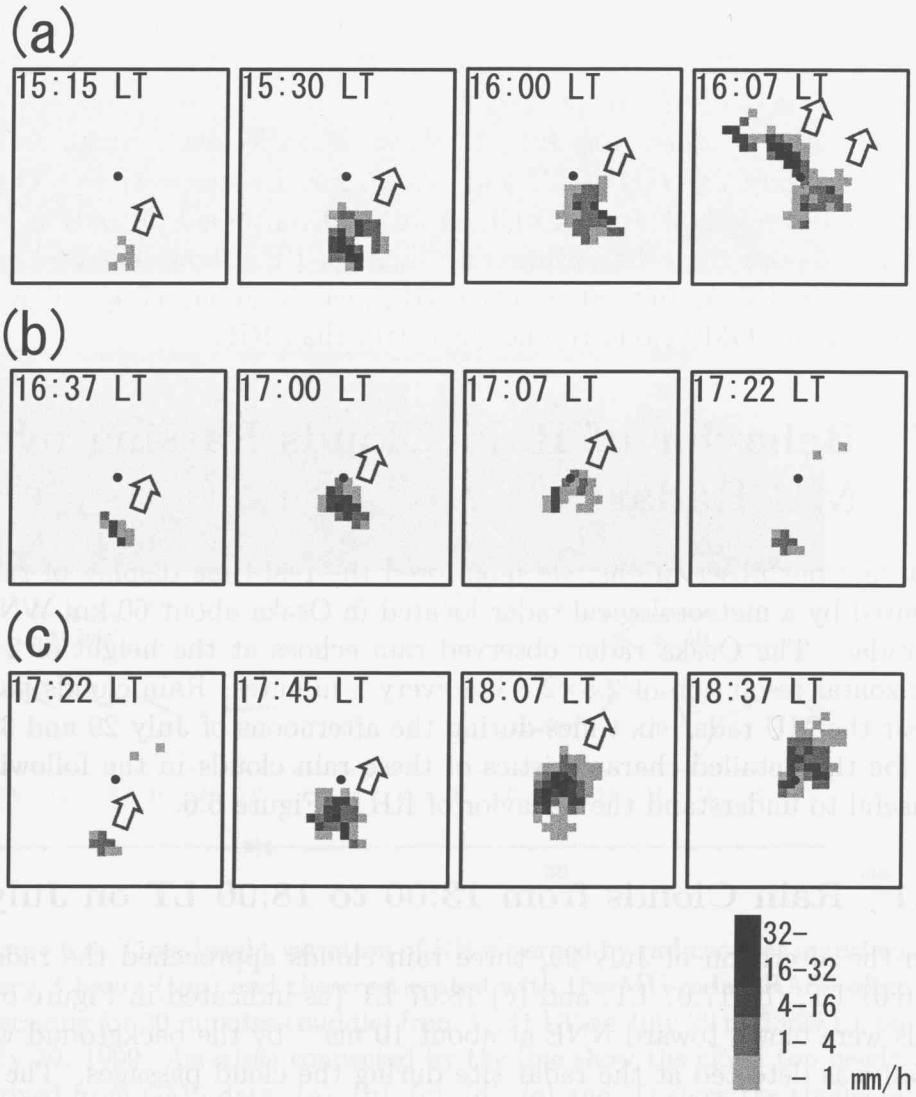

Figure 6.7: Horizontal distribution of rain intensity in an area of 25 × 25 km observed with the meteorological radar at Osaka during the passing of rain clouds (a), (b) and (c). The circle at the center shows the horizontal extent of the antenna beam positions at an altitude of 7.5 km.

along the SE-NW direction appeared SE of the MU radar. A rain echo as strong as 32 mm h^{-1} was observed 4 km SW of the MU radar, although the MU radar site was not covered by the rain cloud. After 16:07 LT both rain bands moved away to the NNE.

(b) A rain cloud appeared 10 km south of the MU radar at 16:37 LT, and moved toward NNE at 10 km h^{-1}. This cloud grazed by the MU radar at 17:07 LT when it was most developed with a radius of 6 km. After passing the MU radar, the decaying rain cloud continued moving to the NNE and disappeared at 17:22 LT.

(c) Another rain cloud appeared at almost the same location as in (b) at 17:22 LT, and approached the MU radar. The center of the rain cloud in the most developed stage passed over the MU radar at 18:07 LT and continued to the NNE.

The radiosonde data showed that the region of RH_s >70% at 4.5–5.5 km persisted from 13:00 LT on July 29 to 6:00 LT on July 30. Note that of the rise in the radar-derived RH_R (>70%) at 4.8–5.5 km is separated into three periods: 15:10–16:45 LT, 16:50–17:30 LT, and 17:30–18:30 LT. The three RH_R peaks agreed well with the passage of rain clouds (a), (b) and (c). Between 3.5 km and 4.1 km, RH_R >70% was observed from 15:20 to 16:10 LT which corresponded to the passage of rain cloud (a).

During the passage of rain cloud (c), RH_R was over 80% from 4.8 to 5.5 km during 17:40–18:15 LT, while for rain clouds (a) and (b), the region of RH>80% was restricted to a very narrow region from 3.8 to 4.9 km at 15:40–45 LT and from 5.0 to 5.2 km at 17:30–40 LT, respectively. The meteorological radar showed that rain cloud (c) passed over the MU radar, and RH_R rose above 80%. The peaks of RH_R were below 80% in the cases of rain clouds (b) and (c) which did not pass over the MU radar.

The cloud-top height measured by GMS showed a single 6.5-km peak at 15:40 LT, when rain cloud (a) approached the MU radar. The peak of RH_R near the cloud top height at 15:40 LT was about 60%. In the case of cloud (a), a rain echo as strong as 32 mm h^{-1} was observed 4 km NE from the MU radar. The rain intensity of (b) and (c) was less than 20 mm s^{-1}, and GMS observation did not show corresponding peaks.

As mentioned, the cloud-top height measured by GMS is an instantaneous value at 40 minutes after the hour. Rain clouds (a), (b), and (c) did not approach the MU radar at the GMS data sample time, so the peak of the cloud top at 15:40 LT probably corresponds to an anvil formation caused by the strong rain cloud

(a). Rain clouds (b) and (c), which were weaker than (a), could not be detected by GMS though, because they did not seem to form a sufficiently large anvil.

6.7.2 Behavior from 19:00 LT on July 29 to 12:00 LT on July 30

Next, we discuss the period from 19:00 LT July 29 to 12:00 LT on July 30. A region with RH_R of >50% was detected at 4.5–5.3 km from 13:00 LT on July 29 to 10:00 LT on July 30, showing general agreement with our radiosonde results, though the radar-derived humidity was smaller than that from the radiosonde data.

The GMS cloud-top height decreased from 17:40 to 19:40 LT on July 29, and reached a minimum height of 1.8 km at 19:40 LT on July 29. From 20:40 LT on July 29 to 0:40 LT on July 30, the cloud-top height stayed at 2.8–3.1 km where RH_R became about 50%.

No GMS-measured TBB was available from 1:40 to 4:40 LT on July 30. Between 5:40 and 7:40 LT and at 9:00 LT on July 30, TBB was about 240 K which corresponded to a cloud top of about 9.5 km. Since the meteorological radar data during this period showed that the MU radar site was not covered by a rain cloud, the cloud-top height of about 9.5 km was not caused by a rain cloud. Instead, it was probably due to a cirrus or anvil cloud in the upper troposphere.

After 10:00 LT on July 30, RH_R between 5 and 6.5 km fell rapidly to less than 10%. The radiosonde data also showed this RH_s decrease. The cloud top also fell from 9:40 LT, probably because the cirrus or anvil cloud in the upper troposphere had disappeared after 10:40 LT.

6.7.3 Rain Clouds from 12:00 to 22:00 LT on July 30

The radiosonde data showed that RH_s reached 70% at 1.5 km at 12:00 LT on July 30. The region where RH_s >70% increased from 12:00 to 17:50 LT, then decreased after the peak at 17:50 LT. The overall structure of RH_R was consistent with RH_s. However, the short-term fluctuation and peaks of RH_R and peaks are not inconsistent with RH_s, since the radiosondes do not have the same time resolution. RH_R showed separate peaks at 2 km at 11:30, 13:00, 14:45, 16:30, 17:30, and 21:00 LT as indicated by the arrows in Figure 6.6.

According to the meteorological radar data, three rain clouds approached the radar site during the afternoon of July 30 at (d) 14:45, (e) 15:45, and (f) 17:30 LT, corresponding to the RH_R peaks at 14:45, 16:30, and 17:30 LT, respectively. No rain clouds corresponding to the other RH_R peaks at 11:30, 13:00, and 21:00 LT

were detected by the meteorological radar. The radius and intensity of rain cloud (f) were larger than those for (d) and (e). The GMS cloud-top height showed a distinct peak at 5.3 km at 17:40 LT which corresponded to rain cloud (f), while the small rain clouds (d) and (e) were not shown by the GMS data.

The rain clouds moved toward NE at about 10 ms^{-1}. Detailed characteristics of these rain clouds, shown in Figure 6.8, were as follows:

(d) A small rain cloud appeared just above the MU radar at 14:45 LT. From 15:00 to 15:07 LT, the developing rain cloud covered the radar site while moving to the NE, and its radius reached 4 km at 15:07 LT. The rain cloud moved farther away from the MU radar, and the distance between the radar and the closest edge of this rain cloud was more than 5 km at 15:15 LT.

(e) A 4-km-wide, 10-km-long rain band that spread along the SE-NW direction appeared 5 km SW of the MU radar at 15:30 LT. This rain band migrated to the NE and reached its highest stage of development at 15:37 LT. At 15:45 LT, the decaying rain band reached the MU radar. The rain cloud above the MU radar disappeared at 16:00 LT. A new weak rain cloud appeared above the MU radar at 16:07 LT. The developing rain clouds, moving toward NE, passed over the MU radar from 16:15 to 16:22 LT, and were fully past by 16:37 LT.

(f) A rain cloud appeared 15 km south of the MU radar at 16:37 LT, and the developing rain cloud was stationary until 16:45 LT. The rain cloud then moved to the NNE toward the MU radar. It decayed at 17:07 LT, but developed again and reached a radius of 25 km at 17:22 LT. The rain cloud in its fully developed stage, with a radius of 10 km, approached and the north edge of the cloud reached the MU radar at 17:30. From 17:30 to 17:45 LT, the disappearing rain cloud passed over the MU radar and rapidly moved toward NE decaying at 18:00 LT.

6.8 Detailed Time-Height Structure of Meteorological Parameters

Next, we discuss in detail the variation in q_R by comparing it with the rain cloud characteristics detected by the meteorological radar, the wind velocity and θ, and the surface meteorological observations from 14:00 to 20:00 LT on July 30.

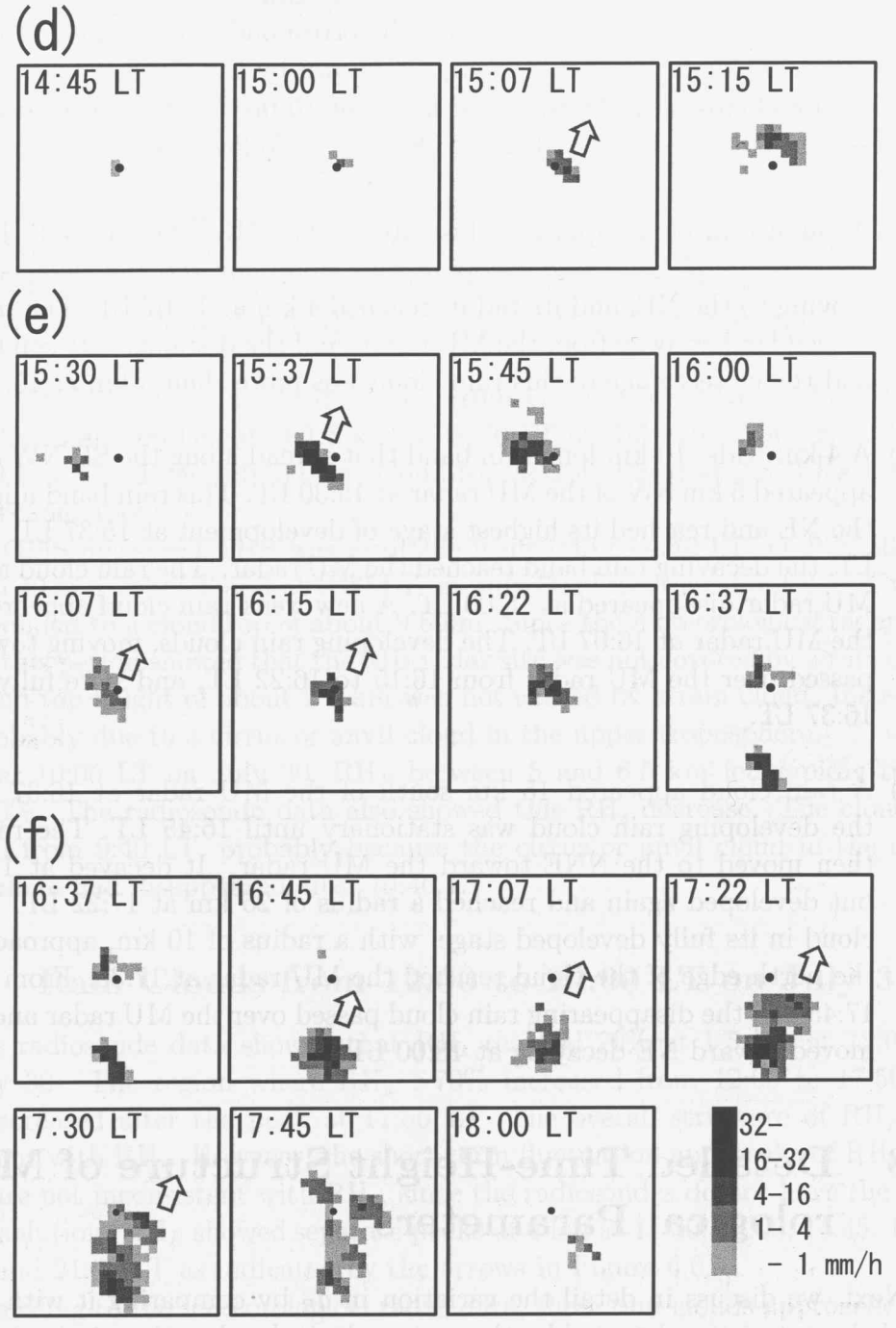

Figure 6.8: The same as Figure 6.7 for the passing of rain clouds (d), (e) and (f).

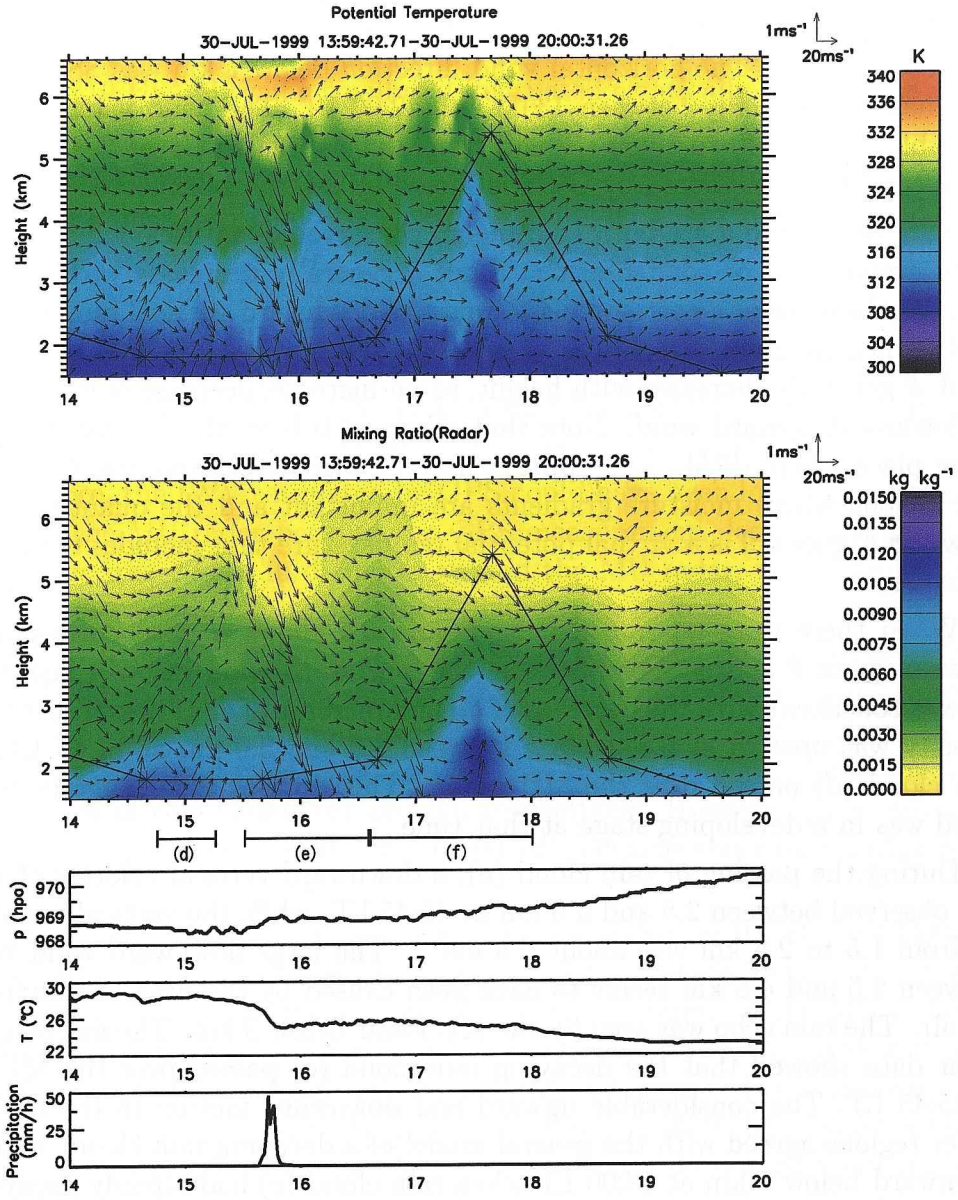

Figure 6.9: Time-height distribution of θ (top) and q_R (middle) observed by the MU radar–RASS from 14:00 to 20:00 LT on July 30, together with the horizontal and vertical wind velocities indicated by vectors. The cloud-top height obtained by GMS is indicated by asterisks connected by the line. The three panels at the bottom show the time variation of the surface pressure, temperature and precipitation observed at the MU radar. (d), (e) and (f) show the timing of rain clouds passing.

The top and second panels of Figure 6.9 show the time-height distributions of θ and q_R together with wind velocity vectors consisting of horizontal and vertical components. The horizontal wind direction below 7 km was SSW, and did not change drastically between 13:00 and 22:00 LT. The wind velocity was not available from 15:40 to 15:50 LT and from 16:05 to 16:15 LT at 2–4.5 km. The cloud-top height measured by GMS is shown by asterisks connected by lines.

Note that q and θ are both Lagrangian conserved quantities under conditions of no evaporation or condensation. Since q generally decreases with height, an increase/decrease of q corresponds to upward/downward vertical motion, respectively, when the influence of latent heat and advection is negligible. On the other hand, θ generally increases with height, so an increase/decrease of θ corresponds to downward/upward wind. Note that $\mathrm{d}\theta/\mathrm{d}z < 0$ is statically unstable. Thus, those place where $\mathrm{d}\theta/\mathrm{d}z < 0$ appears may be regions of sampling error of θ or else regions where moisture gradients are important and the quantity actually shown in Figure 6.9 is a virtual potential temperature that includes the effects of moisture.

When there were no rain clouds, Figure 6.9 shows a good correspondence between q_R or θ and w. For instance, the downward wind below 4 km at 18:40 LT was consistent with the decrease of q_R and increase of θ. However, the vertical velocity was upward at 0.8–1 ms^{-1} between 1.5 and 3.0 km at 14:45 LT, when rain cloud (d) passed over the MU radar. This upward flow suggests the rain cloud was in a developing stage at that time.

During the passing of rain cloud (e), a downward vertical velocity of 1 ms^{-1} was observed between 2.5 and 4.5 km at 15:45 LT, while the vertical wind velocity from 1.5 to 2.5 km was about 0.8 ms^{-1}. The large downward wind velocity between 2.5 and 4.5 km seems to have been caused by the drag of raindrops on the air. The rain echo was seen by the MU radar below 3 km. The meteorological radar data showed that the decaying rain cloud (e) passed over the MU radar at 15:45 LT. The considerable upward and downward motion in the lower and upper regions agreed with the general model of a decaying rain cloud. w became downward below 5 km at 16:00 LT when rain cloud (e) had already decayed. As the decaying process advanced, the vertical velocity became downward throughout the height range of the decaying rain cloud. In the region where there was a strong downward wind from 15:40 to 16:10 LT, θ decreased by about 4 K and q_R increased by about 0.001 $\mathrm{kg\,kg}^{-1}$. The downward motion seems to carry the air downward with high θ and low q.

The other three panels of Figure 6.9 show variation in the pressure, temperature, and precipitation observed on the ground at the MU radar site. At 15:43 LT, the surface pressure increased by 0.5 hPa, and temperature sharply decreased

by 2 K. A rapid rain meter detected a heavy rainfall of 40 mm h^{-1} between 15:45 and 15:55 LT, just after a gust front generated by the downward flow of air cooled by the evaporation of raindrops, passed over the MU radar at 15:40 LT. From 15:20 to 16:10 LT, θ became small and fluctuated erratically between 4.8 and 6.5 km, which seems to be related to the passing of rain cloud (e).

During the passing of rain cloud (f), RH_R >70% was detected only below 3.5 km, and the GMS cloud-top height was higher than that indicated by the radar results. From 17:25 to 17:35 LT, θ decreased by 5–7 K at 3.8–4.5 km and 2.8–3.4 km, and this decrease was accompanied by a downward flow as strong as 1 ms^{-1}. These observations suggest that the atmosphere was cooled due to raindrop evaporation . A large rain cloud (f) with a radius of 25 km was observed at 17:30 LT, and the north edge of the cloud reached the MU radar. However, there were no rain clouds in the other directions from the MU radar.

Therefore, the IWV estimated by GPS could have been lower than the actual IWV over the MU radar because the GPS measurement determined an average value for an area 22 km in diameter around the MU radar, while the MU radar observed a horizontal region 3.4 km in diameter as indicated in Figure 6.8.

Figure 6.10 shows the temporal variation of q_R, ε, the variance of w ($\overline{w^2}$), and T from 14:02 to 19:32 LT on July 30 at altitudes of 3 and 4.5 km. Note that $\overline{w^2}$ was calculated over 30 minutes. Figure 6.10 shows a rising q_R from 15:25 to 16:00 LT at 3 km and from 17:20 to 17:40 LT at 3 and 4.5 km, corresponding to the approach of rain clouds (e) and (f), respectively. However, q_R, ε, $\overline{w^2}$, and T at 3 and 4.5 km did not rise for rain cloud (d), because this rain cloud appeared below 3 km.

Peaks in both ε and $\overline{w^2}$ at 3 and 4.5 km (indicated by (i)) suggest there was a strong atmospheric disturbance. ε and $\overline{w^2}$ were already decreasing at about 15:45 LT, when the decaying rain cloud (e) came nearest to the MU radar. $\overline{w^2}$ also peaked at 16:10 LT at 3 km, which corresponded to the weak rain cloud at 16:07 LT. ε, however, did not show a distinct peak. The temperature fell by about 2 K at both 3 and 4.5 km from 16:00 to 16:10 LT. Under adiabatic and non-advective conditions, T should increase in a downward wind region, so this decrease of T was probably caused by atmosphere cooling due to raindrop evaporation .

When rain cloud (f) passed by, a peak in q_R was seen from 17:20 to 17:40 LT at 3.0–4.5 km, and corresponding rises in $\overline{w^2}$ and ε were also observed, except for $\overline{w^2}$ at 4.5 km (indicated by (iii)). The time variation of T shows a sharp trough at 17:30 LT at 4.5 km. Another trough was seen at 17:40 LT at 3 km where w was downward. The cooling effect of raindrop evaporation on the atmosphere was also apparent in this case. Note that at 16:50 LT ε rose at 3 and 4.5 km before

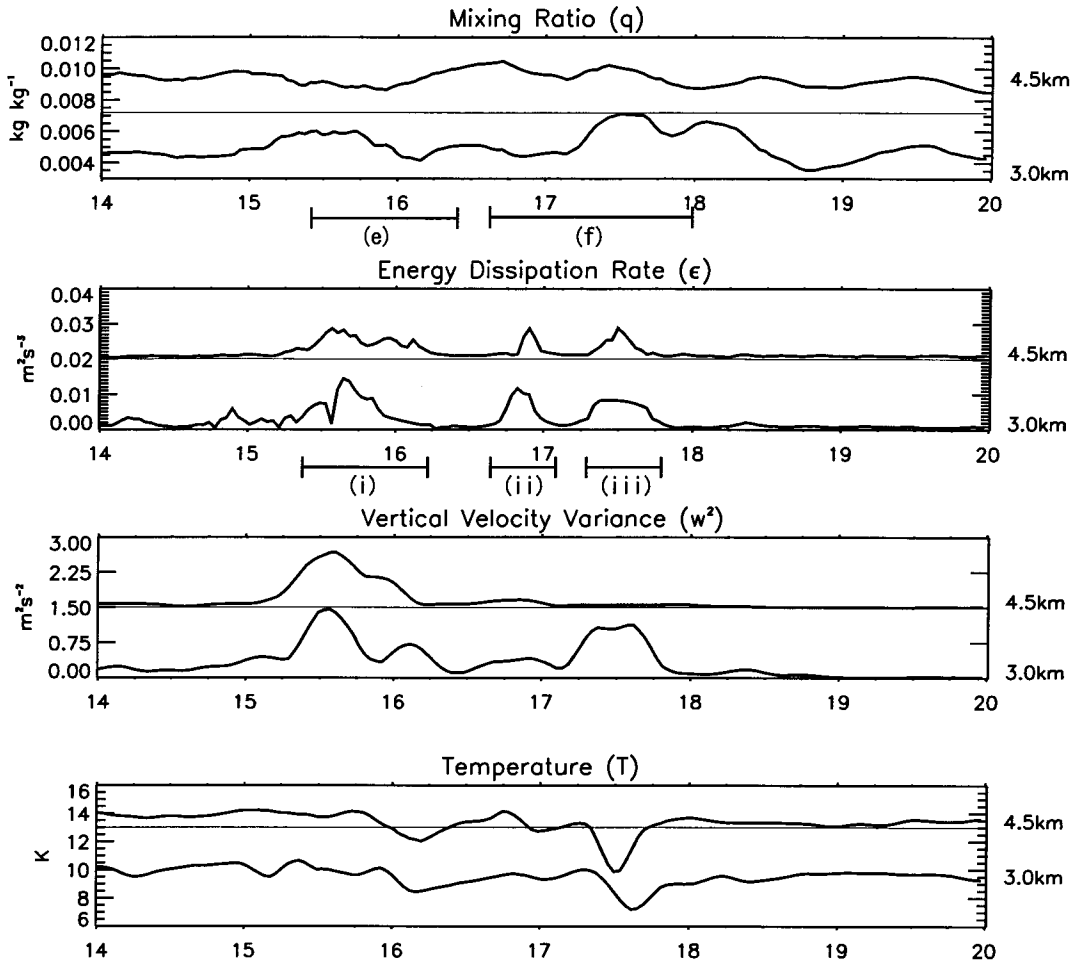

Figure 6.10: Time variation in q_R, ε, $\overline{w^2}$ and T from 14:58 to 18:10 LT on July 30. The variance of w was calculated for 30 minutes. Distinct peaks in ε are indicated as (i), (ii) and (iii) as explained in the text.

the passage of rain cloud (f) (indicated by (ii)), although q_R, $\overline{w^2}$, and T did not peak. This peak in ε corresponds to the development of rain cloud (f) 15 km SSE of the MU radar. Rain cloud (f) at 16:50 LT seems to have been so strong that ε over the MU radar rose sharply, but the other parameters did not significantly vary because the rain cloud was far (15 km south) from the MU radar.

We also observed complicated phenomena even when no rain clouds were present, such as the rise in q_R at 3 km at 18:10 LT where no other parameters showed a corresponding change. There are also regions of a high θ from 5.5 to 6.0 km at 17:00–17:15 LT and 17:20–17:35 LT.

6.9 Concluding Remarks

During our MU radar–RASS observations from July 29 to August 4, 1999, we collected both turbulence echoes and virtual temperatures with good time resolution. We estimated q profiles from the MU radar–RASS measurements by using the characteristics of turbulence echoes. We simultaneously measured PWV by GPS and launched radiosondes, which are used to constrain the retrieval of the q profiles. Our main findings were as follows:

1. The height structure of q can be estimated from the radar-derived M by inferring the sign for $|M|$. We have developed a new algorithm to guess the sign of M by referring to the radiosonde q profile and the PWV obtained by GPS measurement. As $\overline{\eta_{turb}}$ is also affected by F, which is difficult to determine from actual observations, we estimated F by using the NOAA Aeronomy Laboratory C_n^2 model by *Warnock and VanZandt* [1985] with high-resolution wind and temperature profiles obtained through the MU radar–RASS measurements. We studied the influence of F on the accuracy of the estimated q and found that F does not significantly affect q below 5.3 km. The estimation error of q therefore seems to be as small as 10% below 5.3 km, even when F is derived from radiosonde data rather than MU radar–RASS data. The influence of ε on q was found to be as small as 15% below 4.8 km under light winds. However, if winds are stronger, the accuracy of the estimated ε and hense q may fall.

2. The height structure of the q_R profile agreed well with q_s ,with the differences between q_R and q_s mostly within 1.5 $\times 10^{-3}$ kg kg^{-1} from 1.5 to 7.5 km. However, significant discrepancies were sometimes seen.

3. The radar- and radiosonde-derived humidity characteristics agreed well, although the radiosonde results tend to be higher than with q_R especially

under disturbed conditions. The PWV estimated by GPS represents the average value of a wide area around the MU radar, while the MU radar observed PWV in a narrow area within a zenith angle of less than 10° above the MU radar. In future observations, we will use instruments that measure PWV in a narrow horizontal area, such as a microwave radiometer, instead of GPS. The radar-derived humidity fluctuated with a typical time scale of 1–1.5 hours, which cannot be detected with radiosondes. The cloud-top height measured by GMS was generally in better agreement with RH_R values than RH_s.

4. We monitored the real-time meteorological radar results during the RASS observations, and found that a total of six rain clouds passed over or near the MU radar. The radar-derived humidity was well correlated to the rain cloud characteristics.

We have thus shown that the radar remote-sensing technique for determining q profiles used in this study is a useful means of continuously estimating the specific humidity profile at 1.5–7.5 km.

By applying the results of this study, a wind profiler with RASS can be used to simultaneously observe vertical and horizontal wind velocity, temperature, and humidity, which will contribute greatly to the study of meso-scale atmospheric thermodynamics.

Chapter 7

Summary and Conclusions

Simultaneous observations of wind velocity, temperature, humidity, and turbulence intensity are essential to study the detailed structure of atmospheric thermodynamics. A three-dimensional wind field can be observed by the wind profiler radar, while temperature profiles can be monitored by RASS with good time and height resolution. However, humidity profiles have not previously been continuously monitored with radar remote-sensing techniques. In addition, although the wind profiler radar has been applied to estimate the turbulence energy dissipation rate (ε), certain problems need to be solved to enable consistently accurate estimation, especially under strong wind or shear conditions. This thesis has examined the development of techniques to use radar to estimate humidity and ε, which is aimed at enabling the simultaneous observation of wind velocity, temperature, ε, and humidity.

Chapter 1 explained the purpose of this research, and looked at the previous work done concerning ε and humidity measurements.

Chapter 2 provided a theoretical background regarding turbulence echoes. The radar equation for turbulence echoes and a basic relationship to determine the turbulence echo power were described, as were methods of estimating ε. The RASS technique was explained, along with the radar equation for the RASS echo and the ray-tracing of acoustic wavefronts. The actual RASS system incorporated with the MU radar and typical temperature observations made with the MU radar–RASS were also described.

Chapter 3 presented an improved dual-beamwidth spectral width method to estimate ε. This method removes the broadening effects through simultaneous observations of nested sampling volumes with two different beamwidths. The principal advantage over the conventional method is less sensitivity to the error that occurs in the broadening model. The profiles from the two methods closely agreed under light wind conditions, but the agreement weakened as the

wind speed rose. The difference at higher wind speeds was probably caused by the rough approximation inherent in the model assumptions in the conventional method. Nonetheless, the conventional method was reasonably accurate under weak wind conditions.

Chapter 4 compared the ε values obtained using the echo power and spectral width methods under calm meteorological conditions. In both methods, the high-resolution Brunt Väisälä frequency squared (N^2) derived from temperature profiles obtained with the MU radar–RASS was used to estimate ε. The ε provided by the spectral width method is mainly determined by the spectral width and the influence of N^2 is small, while the ε provided by the echo power method showed fairly large time variations which cannot be detected with the spectral width method. These large variations seemed to be caused by the variation in the echo power intensity. The detailed comparison indicated that the echo power variation mainly depends on variation in the refractive index gradient (M), which in turn is mainly determined by the vertical humidity gradient.

Chapter 5 looked at a new radar remote-sensing technique used to measure a humidity profile based on the strong dependence of turbulence echo power on the vertical humidity gradient. The first-order differential equation for humidity was derived, whose solution requires an accurately determined profile of M. However, since a radar can only determine $|M|$ from the turbulence echo power, a method was needed to determine the sign of M. The method to estimate the sign from the correlation between M and $-N^2$ has been developed. The humidity profile thus derived from the MU radar–RASS measurement agreed well with simultaneous radiosonde results.

Chapter 6 looked at a way to improve the humidity estimation technique to allow more robust estimation even under disturbed meteorological conditions. This new algorithm estimates the sign of M by referring to the precipitable water vapor obtained by GPS measurement. Humidity profiles were estimated by using the improved method with the MU radar–RASS data obtained in July, 1999. The time-height structure of the radar-derived humidity agreed well with simultaneous radiosonde results obtained every three hours, although the radar-derived humidity revealed short-term fluctuations with a period of 1–1.5 hours which could not be observed by the intermittent radiosondes. The radar-derived humidity was also compared with data from a meteorological radar. During the observation campaign, a total of six rain clouds passed over or near the MU radar. The hourly fluctuation of radar-derived humidity was consistent with the movement and the development or decay of the rain clouds as monitored by the meteorological radar.

In summary, radar estimation using the MU radar enables simultaneous ob-

servation of the wind field, temperature, humidity, and ε, which will be a valuable means of investigating the thermodynamics of meso- and micro-scale disturbances. In the future, the members of this study will attempt to apply other forms of radar, such as the equatorial atmosphere radar (EAR) and the lower troposphere radar (LTR), in this field of observation. The use of the EAR will be useful for unveiling small-scale phenomena occurring in equatorial regions. In addition, LTR have developed by *Hashiguchi et al.* [2002], and a total of 25 LTR sites have recently been installed by the Japan Meteorological Agency (JMA). Applying the techniques described in this thesis through these sites should greatly improve the accuracy of short-term weather forecasting by allowing the radar-derived humidity to be incorporated into numerical forecasting models. Another important area for future work will be cooperative observation with the Mie lidar which can monitor the scattering from water or ice particles. These observations will be useful for clarifying the detailed structure of cloud dynamics.

Appendix A

Spatial Structure of the RASS Echo with Multiple Acoustic Sources

In this chapter, we investigate the echo pattern on the ground when multiple acoustic speakers are simultaneously used. Table A.1 shows the observation parameters of the MU radar–RASS experiment on December 18, 1996. The MU radar antenna array could be divided into 25 sub-arrays, which could be independently activated as transmitting and receiving antennas. We used seven sub-arrays for transmission and 20 sub-arrays for reception. Because only four receiver channels were available, we could not simultaneously determine the echo pattern. RASS measurements lasting 3 minutes were done five times while changing the combination of receiver sub-arrays. As a result, it took 15 minutes to obtain one distribution of the RASS echo pattern. The measured differences in sensitivity between the sub-arrays were less than 0.2 dB. Therefore, no correction of the sub-array sensitivity was needed.

The ray-tracing of the acoustic wavefronts was analyzed to determine the radar-beam directions and the positions of the acoustic sources. A temperature profile was measured using a simultaneous radiosonde, and wind velocity of above 1.5 km was observed with the MU radar. Wind profiles when the wind velocity was below 1.5 km were estimated by combining the MU radar results with the surface wind measurements. An accurate temperature profile was not required for the ray-tracing analysis because the effect of temperature variation on the acoustic wave is insignificant compared to that of wind-velocity variation.

From the results of the ray-tracing analysis, we selected two radar-beam directions at (azimuth and zenith angle) = (285°, 28°) and (285°, 32°), and two sound sources at (distance, azimuth angle, and elevation) = (55 m, 264°, −0.29

Table A.1: Observation parameters on December 18, 1996.

MU Radar	
height range (km)	1.20–5.85 km
inter-pulse period(μs)	416
sub-pulse length (μs)	1
pulse compression bit	2
number of beams	2
number of receiver channels	4
coherent integration	32
number of FFT points	256
incoherent integration	4
observation duration (s)	27.3
beam direction	
(azimuth angle, zenith angle)	(285°, 28°), (285°, 32°)
offset Doppler velocity (ms^{-1})	302.7
parameter estimation method	0th and 1st order moments
Acoustic Source	
transmitter type	hyperbolic horn speaker
wave form	CW
repetition period (s)	0.5
chirped frequency range (Hz)	85.0–107.0
location of transmitter from radar center	(1) (55 m, 264°, −0.29 m)
(r, azimuth angle, z)	(2) (55 m, 293°, −0.30 m)
	(3) (55 m, 323°, −0.30 m)
transmission speaker	(2)
	(1) and (3)
	(1),(2) and (3)

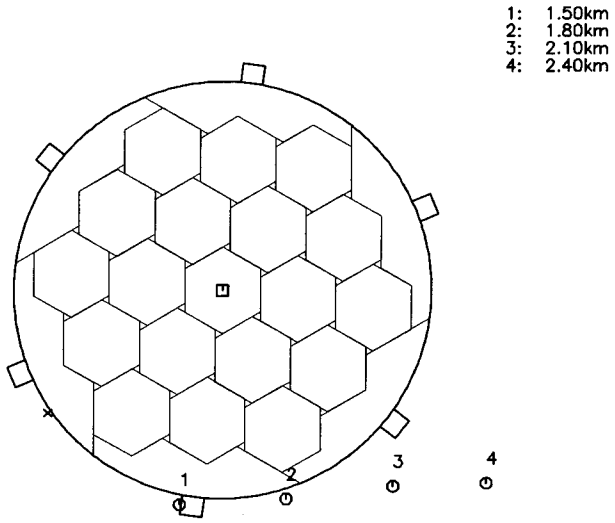

Figure A.1: The center of the RASS echo spot simulated through ray-tracing of acoustic wavefronts. The radar-beam direction was (azimuth angle, zenith angle) = (285°, 28°). Acoustic sources were located at (distance, azimuth angle, height) = (55 m, 264°, −0.29 m) as indicated by ×. The □ shows the location of the center of the radar antenna, and each ○ shows the center of the RASS echo spot at a particular height.

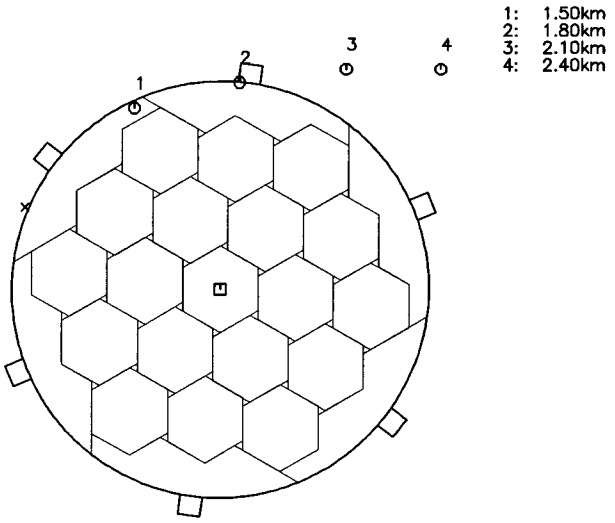

Figure A.2: The same as in Figure A.1, except that an acoustic source was located at (distance, azimuth angle, height) = (55 m , 323°, −0.30 m).

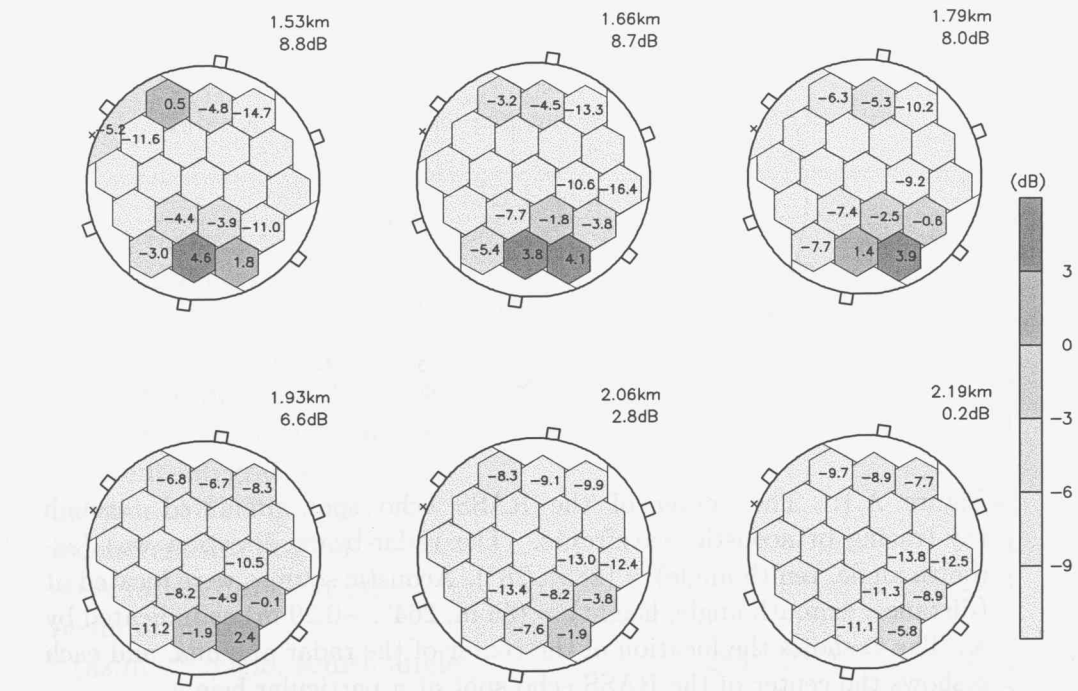

Figure A.3: Distribution of RASS echo intensity (S/N) observed by each sub-array at 23:07 LT on December 18, 1995. The radar beam direction was (azimuth angle, zenith angle) = (270°, 28°). The altitude and total S/N are shown at the upper right of the MU radar antenna. S/N was corrected by being multiplied by a factor of r^{-2}. The × shows the location of the acoustic sources.

m), and (55 m, 323°, −0.30 m).

We calculated the center of the RASS echo pattern by using geometrical optics and the acoustic wavefronts simulated through ray-tracing. Figures A.1 and A.2 show the results when we independently used a single acoustic source at (285°, 28°) and (285°, 32°). The center of the RASS echoes was expected to be near the north and south edges of the MU radar antenna array.

Figure A.3 shows the observed horizontal distribution of the RASS echo pattern. Note that the attenuation of the RASS echo intensity was corrected by multiplying a factor proportional to the inverse square of range (r^{-2}). The sub-array with S/N greater than 6 dB was distributed around both the north and south borders of the MU radar antenna. Our findings suggest that acoustic waves

transmitted from multiple acoustic sources independently scatter radio waves, so the resultant RASS echo can be considered a superposition of these independent scatterings. Because the azimuth angle of the two acoustic sources differed by 30°, the shape of the acoustic wavefronts also differed, which caused the RASS echoes to be scattered from different height ranges. It is thus important to arrange sound sources around the best location and to change them according to variation in the background wind velocity and temperature to detect RASS echoes from a wide range of heights.

References

Adachi, T., T. Tsuda, Y. Masuda, T. Takami, S. Kato, and S. Fukao, Effects of the acoustic and radar pulse length ratio on the accuracy of radio acoustic sounding system (RASS) temperature measurements with monochromatic acoustic pulses, *Radio Sci.*, **28**, 571–583, 1993.

Adachi, T., Detailed temperature structure of meteorological disturbances observed with RASS (radio acoustic sounding system), PhD. thesis, Kyoto University, 1996.

Atlas, D., Advances in radar meteorology in Adv. Geophys., edited by H. Landsberg and J. van Mieghem, pp. 317–478, Academic Press, New York, 1964.

Balsley, B. B. and K. S. Gage, The MST radar technique: Potential for middle atmosphere studies, *Pure Appl. Geophys.*, **118**, 452–493, 1980.

Bertin, F., J. Barat, and R. Wilson, Energy dissipation rates, eddy diffusivity, and the Prandtl number: An *in-situ* experimental approach and its consequences on radar estimate of turbulent parameters, *Radio Sci.*, **32**, 791–804, 1997.

Bohne, R., radar detection of turbulence in thunderstorms, reports # AFGL-TR-81-0102 (ADA 108679), Air Force Geophys. Lab., Hanscom Air Force Base, MS, U.S.A., 1981.

Chen, Y., Energy dissipation rates of free atmospheric turbulence, *J. Atmos. Sci.*, **31**, 2222–2225, 1974.

Cohn, S., Radar measurements of turbulence eddy dissipation rate in the troposphere: A comparison of techniques, *J. Atmos. Ocean. Technol.*, **12**, 85–95, 1995.

Crane, K., Statospheric turbulence analysis, report # AFGL-TR-77-0207 (ADO 47740), Air Force Geophys. Lab., Hanscom Air Force

Base, MS, U.S.A., 1980.

Crooks, M. and Co-authors, Project HICAT: An investigation of high altitude clear air turbulence, Air Force Flight Dynamics Laboratory Technical Report, AFFDL-TR-67-123, 255pp, 1967.

Delage, D., R. Roca, F. Bertin, J. Delcourt, A. Crémieu, M. Massebeuf and R. Ney, A consistency check of three radar methods for monitoring eddy diffusion and energy dissipation rates through the tropopause, *Radio Sci.*, **32**, 757–767, 1997.

Fukao, S., T. Sato T. Tsuda, S. Kato, K. Wakasugi, and T. Makihira, The MU radar with an active phased array system 1. Antenna and power amplifiers, *Radio Sci.*, **20**, 1155–1168, 1985.

Fukao, S., T. Sato, T. Tsuda, M. Yamamoto, M. D. Yamanaka, and S. Kato, MU radar: New capabilities and system calibrations, *Radio Sci.*, **25**, 477–485, 1990.

Fukao, S., M. D. Yamanaka, N. Ao, W. K. Hocking, T. Sato, M. Yamamoto, T. Nakamura, T. Tsuda, and S. Kato, Seasonal variability of vertical eddy diffusivity in the middle atmosphere, Part I: Three-year observations by the MU radar, *J. Geophys. Res.*, **99**, 18,973–18,987, 1994.

Furumoto, J. and T. Tsuda, Characteristics of energy dissipation rate and effect of humidity on turbulence echo power revealed by MU radar-RASS measurements, *J. Atmos. Solar-Terr. Phys.*, **63**, 285–294, 2001.

Furumoto, J., K. Kurimoto, and T. Tsuda, Continuous monitoring of humidity profiles with the MU radar–RASS, *J. Atmos. Ocean. Technol.*, submitted, 2002.

Gage, K. S. and J. Green, Evidence for specular reflection from monostatic VHF radar observations of the stratosphere, *Radio Sci.*, **13**, 991–1001, 1978.

Gage, K. S., J. Green, and T. E. VanZandt, Use of Doppler radar for the measurement of atmospheric turbulence parameters from the intensity of clear air echoes, *Radio Sci.*, **15**, 407–416, 1980.

Gage, K. S., C. Williams, W. Ecklund, and P. Johnston, Use of two profilers during MCTEX for unambiguous identification of Bragg scattering and Rayleigh scattering, *J. Atmos. Sci.*, **56**, 3679–3691, 1999.

Goldsmith, J. E., M., S. E. Bisson, R. A. Ferrare, K. D. Evans, D. N. Whiteman, S. H. Melfi,, Raman lidar profiling of atmospheric water vapor: simultaneous measurements with two collocated systems, *Bull. Amer. Meteor. Soc.*, **7**, 975–982, 1994.

Gossard, E. E., R. B. Chadwick, W. D. Neff, and K. P. Moran, The use of ground-based Doppler radars to measure gradients, fluxes and structure parameters in elevated layers, *Appl. Metorol.*, **21**, 211–226, 1982.

Gossard, E. E. and N. Sengupta, Measuring gradients of meteorological properties in elevated layers with a surface-based Doppler radar, *Radio Sci.*, **23**, 625–639, 1988.

Gossard, E. E., Radar research on the atmospheric boundary layer, Radar in Meteorology: Battan Memorial and 40th Anniversary Radar Meteorology Conference, 477–527, 1990.

Gossard, E. E., D. E. Wolfe, K. P. Moran, R. A. Paulus, K. D. Anderson, and L. T. Rogers, Measurements of clear-air gradients and turbulence properties with radar wind profilers, *J. Atmos. Ocean. Technol.*, **15**, 321–342, 1998.

Gossard, E. E., S. Gutman, B. B. Stankov, and D. E. Wolfe, Profile of radio refractive index and humidity derived from radar wind profilers and the Global Positioning System, *Radio Sci.*, **34**, 371–383, 1999.

Hashiguchi, H., S. Fukao, Y. Moritani, T. Wakayama, and S. Watanabe, A lower troposphere radar: 1.3-GHz active phased-array type wind profiler with RASS, *J. Meteor. Soc. Japan*, submitted, 2002.

Heisenberg, W., Zur statistischen theorie der turbulenz, *Zeit. f. Phys.*, **124**, 628–657, 1948.

Hirahara, K., Local GPS tropospheric tomography, *Earth, Planets and Space*, **52**, 935–939, 2000.

Hocking, D. C., S. Fukao, M. Yamamoto, T. Tsuda, and S. Kato, Viscosity waves and thermal-conduction waves as a cause of 'specular' reflections in radar studies of the atmosphere, *Radio Sci.*, **26**, 1403–1422, 1991.

Hocking, W. K., On the extraction of atmospheric turbulence parameters from radar backscatter Doppler spectra, *J. Atmos. Terr. Phys.*, **45**, 89–102, 1983.

Hocking, W. K., Measurement of turbulent energy dissipation rates in the middle atmosphere by radar techniques: a review, *Radio Sci.*, **20**, 1403–1422, 1985.

Hocking, W. K., An assessment of the capabilities and limitations of radars in measurements of upper atmosphere turbulence, *Adv. Space Res.*, **17**, (11)37-(11)47, 1996.

Hocking, W. K. and P. K. L. Mu, Upper and middle tropospheric kinetic energy dissipation rates from measurements of $\overline{C_n^2}$ – review of theories, *in-situ* investigations, and experimental studies using the Buckland Park atmospheric radar in Australia, *J. Atmos. Terr. Phys.*, **59**, 1779–1803, 1997.

Hocking, W. K., The dynamical parameters of turbulence theory as they apply to middle atmosphere studies, *Earth, Planets and Space*, **51**, 525–541, 1999.

Kley, D., H. G. J. Smith, H. Vömel, H. Grassl, V. Ramanathan, P. J. Crutzen, S. Williams, J. Meywerk, and S. J. Oltmans, Tropospheric water-vapor and ozone cross-sections in a zonal plane over the central equatorial Pacific ocean, *Q. J. R. Meteorol. Soc.*, **123**, 2009–2040, 1997.

Kolmogorov, N., The local structure of turbulence in incompressible viscos fluid for very large Reynolds number, *Dokl. Akad. Nauk SSSR*, **30**, 299–303, 1941.

Kung, C., Large scale balance of kinetic energy in the atmosphere, *Mon. Weather Rev.*, **94**, 627–640, 1966.

Kurosaki, S., M. D. Yamanaka, H. Hashiguchi, T. Sato and S. Fukao, Vertical eddy diffusivity in the lower and middle atmosphere: a climatology based on the MU radar observations during 1986-1992, *J. Atmos. Terr. Phys.*, **58**, 727–734, 1996.

Lee, Y., R. Paradis, and D. Klingle-Watson, Preliminary results of the 1983 Coordinated Aircraft-Doppler Weather Radar Turbulence Experiment, Vol. 1. Report # DOT/FAA/PM-86/11 (A197894), Lincoln, Lab., MIT Lexington, MS, U.S.A., 1988.

Lilly, K., E. Waco, and I. Adelfang, Stratospheric mixing from high-altitude turbulence measurements, *J. Appl. Meteor.*, **13**, 488–493, 1974.

Maeda, K., S. Maeda, An observation of galactic background radiation

with MU radar, Proceedings of the MU radar symposium , 2–3, 1991.

Mapes, B. E. and P. Zuidema, Radiative-dynamical consequences of dry tongues in the tropical troposphere, *J. Atmos. Sci.*, **53**, 620–638, 1996.

Marshall, J. M., A. M. Peterson, and A. A. Barnes, Jr., Combined radar-acoustic sounding system, *Appl. Optics*, **11**, 108–112, 1972.

Masuda, Y., Influence of wind and temperature on the height limit of a radio acoustic sounding system, *Radio Sci.*, **23**, 647–654, 1988.

Matsuura, N., Y. Masuda, H. Inuki, S. Kato, S. Fukao, T. Sato and T. Tsuda, Radio acoustic measurement of temperature profile in the troposphere and statrosphere, *Nature*, **323**, 426–428, 1986.

May, P. T., K. P. Moran, and R. G. Strauch, The accuracy of RASS temperature measurements, *J. Appl. Meteor.*, **28**, 1329–1335, 1989.

May, P. T., T. Adachi, T. Tsuda, and R. Lataitis, The spatial structure of RASS echoes, *J. Atmos. Ocean. Tech.*, **13** 1275–1284, 1996.

Miloshevich, L., H. Vömel, A. Paukkunen, and A. Heymsfield and S. Oltmans, Characterization and correction of relative humidity measurements from vaisala RS80-A radiosondes at cold temperatures, *J. Atmos. Ocean. Technol.*, **18**, 135–156, 2001.

Miyazaki, S. and Y. Hatanaka, Continuous GPS observation system of Geopraphical Survey Instutute, *Meteor. Res. Note*, **192**, 93–105, 1998.

Narayana Rao, D., P. Kishore, T. Narayana Rao, S. Vijaya Bhaskara Rao, K. Krishna Reddy, M. Yarraiah, and M. Hareesh, Studies on refractivity structure constant, eddy dissipation rate, and momentum flux at a tropical latitude, *Radio Sci.*, **22**, 1375–1389, 1997.

Nastrom, G. D., Doppler radar spectral width broadening due to beamwidth and wind shear, *Annales Geophysicae*, **15**, 786–796, 1997.

Nastrom, G. D. and F. D. Eaton, Turbulence eddy dissipation rates from radar observations at 5-20 km at White Sands Missile Range, New Mexico, *J. Geophys. Res.*, **102**, 19,495–19,505, 1997.

Ottersten, H., Mean vertical gradient of potential refractive index in turbulent mixing and radar detection of CAT, *Radio Sci.*, **4**, 1247–1249, 1969.

Probert-Jones, J. R., The radar equation in meteorology. *Q. J. R. Meteorol. Soc.*, **88**, 485–495, 1962.

Seko, H., S. Shimada, H. Nakamura, and T. Kato, Three-dimensional distribution of water vapor estimated from tropospheric delay of GPS data in a mesoscale precipitation system of Baiu front, *Earth, Planets and Space*, **52**, 927–933, 2000.

Silver, S., Microwave antenna theory and design, McGraw-Hill, New York, 1951.

Stankov, B. B., B. E. Martner, and M. K. Politovich, Moisture profiling of the cloudy winter atmosphere using combined remote sensors, *J. Atmos. Ocean. Technol.*, **12**, 488–510, 1995.

Stankov, B. B., E. R. Westwater, and E. E. Gossard, Use of wind profiler estimates of significant moisture gradients to improve humidity profile retrieval, *J. Atmos. Ocean. Technol.*, **13**, 1285–1290, 1996.

Tatarski, V. I., Wave propagation in a turbulent medium, McGraw-Hill, New York, 1961.

Tsuda, T., T. Sato, T. Fukao, and S. Kato, MU radar observation of the aspect sensitivity of backscattered VHF echo power in the troposphere and lower stratosphere, *Radio Sci.*, **21**, 971–980, 1986.

Tsuda, T., P. T. May, T. Sato, S. Kato, and S. Fukao, Simultaneous observations of reflection echoes and refractive index gradient in the troposphere and lower stratosphere, *Radio Sci.*, **23**, 655–665, 1988.

Tsuda, T., Y. Masuda, H. Inuki, K. Takahashi, T. Takami, T. Sato, S. Fukao, and S. Kato, High time resolution monitoring of tropospheric temperature with a radio acoustic sounding system (RASS), *Pure and Appl. Geophys.*, **130**, 497–507, 1989.

Tsuda, T., T. Adachi, Y. Masuda, S. Fukao, and S. Kato, Observations of tropospheric temperature fluctuations with the MU radar-RASS, *J. Atmos. Ocean. Technol.*, **11**, 50–62, 1994.

Tsuda, T., T. E. VanZandt, and H. Saito, Zenith-angle dependence of VHF specular reflection echoes in the lower atmosphere, *J. Atmos.*

Terr. Phys., **59**, 761–775, 1997.

Tsuda, T., M. Miyamoto, and J. Furumoto, Estimation of a humidity profile using turbulence echo characteristics, *J. Atmos. Ocean. Technol.*, **18**, 1214–1222, 2001.

VanZandt, T. E., Vertical profiles of reflectivity turbulence structure constant : Comparison of observations by the Sunset radar with a new theoretical model, *Radio Sci.*, **13**, 819–829, 1978.

VanZandt, T. E. and R. A. Vincent, VHF fresnel reflectivity due to low-frequency buoyancy waves?, *MAP Handbook*, **9**, 78–80, 1983.

VanZandt, T. E., C. Williams, W. L. Clark, W. L. Ecklund, and K. S. Gage, Dual-radar techniques for measuring the turbulence energy dissipation rate ε, paper presented at 29th Intern. Conf. on Radar Meteor., July 12–19, 1999.

VanZandt, T. E., W. L. Clark, K. S. Gage C. R. Williams, and W. L. Ecklund, A dual-wavelength radar technique for measuring the turbulent energy dissipation rate ε, *Geophys. Res. Lett.*, **27**, 2537–2540, 2000.

VanZandt, T. E., G. Nastrom, J. Furumoto, T. Tsuda, and W. L. Clark , A Dual-Beamwidth Radar Method for Measuring Atmospheric Turbulent Kinetic Energy Density, *Geophys. Res. Lett.*, submitted, 2002.

Vinnichenko, K. and A. Dutton, Emprical studies of atmospheric structure and spectra in the free atmosphere, *Radio Sci.*, **4**, 1115–112, 1969.

Ware, R., F. Solheim, R. Carpenter, J. Gueldner, J. Liljegren, T. Nohrkorn, and F. Vandenberghe, Radiometric profiling of tropspheric temperature, humidity and cloud liquid, *Radio Sci.*, submitted, 2002.

Warnock, J. and T. E. VanZandt, A statistical model to estimate the refractivity turbulence structure constant C_n^2 in the free atmosphere, NOAA Tech. Rep., ERL-AL-10, 180pp, 1985.

Woodman, R. F. and Y. H. Chu, Aspect sensitivity masurements of VHF backscatter made with the Chung-Li radar: plausible mechanisms, *Radio Sci.*, **24**, 113–125, 1989.

Wulfmeyer, V. and J. Boesenberg, Ground-based differential absorption lidar for water-vapor profiling: Assessment of accuracy, reso-

lution, and meteorological applications, *Applied Optics*, **37**, 3825–3844, 1998.

Yamamoto, M., T. Sato, P. T. May, T. Tsuda, S. Fukao, and S. Kato, Estimation error of spectral parameters of mesosphere-stratosphere-troposphere radars obtained by least squares fitting method and its lower bound, *Radio Sci.*, **22**, 1013–1021, 1988.

Yoshihara, T., Y. Noguchi, T. Tsuda, and K. Hirahara, A study on a tomography analysis with a moving cell for estimating local-scale distribution of water vapour, *J. IEICE Japan,* **J84-B**, 12, 2236–2243, 2001.

Publication List

Refereed Journals

1. Furumoto, J. and T. Tsuda, Characteristics of energy dissipation rate and effect of humidity on turbulence echo power revealed by MU radar–RASS measurements, *J. Atmos. Solar-Terr. Phys.*, **63**, 285–294, 2001.

2. Tsuda, T., M. Miyamoto, and J. Furumoto, Estimation of a humidity profile using turbulence echo characteristics, *J. Atmos. Ocean. Technol.*, **18**, 1214–1222, 2001.

3. VanZandt, T. E. , G. D. Nastrom, J. Furumoto, and T. Tsuda and W. L. Clark , A dual-beamwidth radar method for measuring atmospheric turbulent kinetic energy density, *Geophys. Res. Lett.*, submitted, 2002.

4. Furumoto, J., K. Kurimoto, and T. Tsuda, Continuous monitoring of humidity profiles with the MU radar–RASS, *J. Atmos. Ocean. Technol.*, submitted, 2002.

Unrefereed Articles

1. Arikawa, Y., T. Tsuda, and J. Furumoto, Fine structure of the tropopause observed with the MU Radar/RASS, Proceedings of Fourth International Symposium on Tropospheric Profiling: Needs and Technologies, 16–18, 1998.

2. Furumoto, J. and T. Tsuda, Turbulence characteristics revealed by the MU radar–RASS, Proceedings of third MU radar symposium, 154–160, 2000 (in Japanese).

3. Furumoto, J. and T. Tsuda, Turbulence characteristics revealed by MU radar–RASS, Proceedings of the ninth international workshop on technical

and scientific aspects of MST radar combinined with COST76 final profiler workshop, 233–236, 2000.

4. Miyamoto, M., T. Tsuda, and J. Furumoto, Estimation of a humidity profile from MU Radar–RASS measurements, Proceedings of the ninth international workshop on technical and scientific aspects of MST radar combinined with COST76 final profiler workshop, 393–396, 2000.